Investigation and Model-Based Design of Rotating Detonation Rocket Engine System

a project presented to
The Faculty of the Department of Aerospace Engineering
San José State University

in partial fulfillment of the requirements for the degree
Master of Science in Aerospace Engineering

by

Anton P. Kulinich

May 2024

approved by

Dr. Periklis Papadopoulos
Faculty Advisor

Abstract

This report provides a detailed review of current state of the art simulation, computational modeling, engineering analysis, and experimental research of rotating detonation rocket engines (RDREs). RDREs leverage supersonic combustion of fuel and oxidizer, a process fundamentally more efficient than the traditional subsonic deflagration employed in contemporary rocket engines. Driven by continuously revolving detonations (wave fronts) RDREs extract more energy relative to deflagration through extremely rapid compression and near constant volume combustion. The fundamental theory is provided along with governing equations and assumptions. The physics of detonation wave combustion is discussed along with comparison to simulation and experiment. A review of simulation and experimental hot fire testing of RDRE systems is included to provide insight into crucial design considerations. Current experimental engines are analyzed and results are studied to understand detonation wave physics, wave stability, combustion chamber conditions, engine performance, manufacturing and design. A detailed description of the numerical modeling approach along with governing equations and assumptions implemented by the leading RDRE research team from NASA is presented. The engineering level analysis code is used to provide suggestions on sizing and performance with quantitative and qualitative system trade studies analyzed. A baseline RDRE design providing equal thrust to a deflagration based engine is made using the RDRE performance and sizing code developed by NASA. Results indicate significant improvement in engine efficiency and performance, form factor reduction, and reduced turbopump system requirements. A large scale design of experiments is executed providing 463,050 unique RDRE configurations. This dataset is leveraged to understand RDRE performance trends in multi-dimensional design space. Sample requirements are set and a final engine design is provided. Suggestions are made on scaling and performance and subsystem and component integration techniques.

Acknowledgments

I want to acknowledge Dr. Periklis Papadopoulos for his advice and guidance on this project. Dr. Papadopoulos has provided me a wealth of technical knowledge and guidance through out my time as a graduate Aerospace Engineering student. It has been a sincere honor to learn, and work along side Dr. Papadopoulos, and to share with him his deep appreciation for all aerospace engineering disciplines.

I would also like to acknowledge the extensive sacrifices my parents have made to provide me with the opportunity to peruse my education. I want to acknowledge fellow SJSU Aerospace Engineering Master's students, classmates, and colleagues, Christopher Crews-Holloway and Travis George. I want to thank them for the many discussions shared, extensive collaboration and development of our skills and knowledge, and guidance from their respective strengths and disciplines of engineering. I would also like to acknowledge Dr. Daniel Paxson and his colleagues at NASA Glenn research center for their guidance and for developing the RDRE performance and sizing analysis code utilized extensively within this report.

Table of Contents

List of Tables

List of Figures

Nomenclature

ϕ	Equivalence Ratio
γ	Specific Heat Ratio
η_c	Combustion Efficiency
η_p	Pump Efficiency
η_t	Turbine Efficiency
ρ	Density
$\rho_{fuel,in}$	Fuel Inlet Density
$\rho_{oxid,in}$	Oxidizer Inlet Density
μ	Viscosity
A_e/A_t	Exit Area Ratio
A_t/A	Throat Area Ratio
a^*	Fill Speed Of Sound
c	Speed of Sound
D_{mean}	Mean Diameter
D_{tube}	Tube Hydraulic Diameter
f	Frequency
F	Thrust
ht	Hub-to-tip Ratio
L_{act}	Engine Length
L_{eff}	Effective Length
$M_{i,avg}$	Fill Mach Number (Average)
$M_{i,max}$	Fill Mach Number (Max)
Nu	Nusselt Number
P	Pressure
P_{det}	Peak Pressure
P_{fill}	Fill Pressure
$P_{fuel,in}$	Cooling Jacket Inlet Pressure
P_{tank}	Tank Pressure
Pr	Prandtl Number
PR_t	Turbine Pressure Ratio
Q_{cool}	Total Heat Load
Q_{tube}	Tube Heat Load
Re	Reynolds Number
R_g	Specific Gas Constant
T_{adb}	Adiabatic Exhaust Total Temperature
$T_{fuel,in}$	Fuel Inlet Temperature
$T_{fuel,out}$	Fuel Outlet Temperature
T_{gg}	Gas Generator Temperature
T_{max}	Mass-Average Exhaust Total Temperature
T_w	Wall Temperature

u	Velocity
U_{tube}	Tube Flow Velocity
V_{loss}	Injector Loss
w_1	Total Mass Flow 1
w_2	Total Mass Flow 2
w_{cool}	Coolant (Fuel) Mass Flow
w_{tube}	Tube Mass Flow
AFRL	Air Force Research Laboratory
CFD	Computational Fluid Dynamics
C-J	Chapman-Jouguet
FEA	Finite Element Analysis
Isp	Specific Impulse
LES	Large Eddy Simulation
LHDR	Length to Hydraulic Diameter Ratio
PDE	Pulse Detonation Engine
RDE	Rotating Detonation Engine
RDRE	Rotating Detonation Rocket Engine

Chapter 1: Introduction to Detonative Propulsion

1.1 Motivation

A Rocket propulsion system is a critical system for many aerospace applications such as orbital launch vehicles, satellites, reentry systems, hypersonic vehicles, missiles and more. The high thrust to weight ratio of these systems offers necessary performance capabilities to achieve high velocities and thrust in the vacuum of space. Liquid rocket engines serve of particular utility for high thrust applications including launch vehicles and newly emerging hypersonic aircraft. Liquid rocket engine systems require both fuel and oxidizer to be stored on board and as such any significant increase in fuel efficiency and propulsive performance would enable mass weight savings and improved capabilities. The ability to allocate additional weight saved from lower fuel consumption enables more payload to be carried by orbital launch systems. Increased fuel efficiency can increase operational range of hypersonic surveillance or transportation systems.

Current industry standard liquid bi-propellant rocket engines today are based off of the Brayton cycle. Research began in the 1940's to investigate using pressure gain detonative combustion to achieve higher thermodynamic efficiency in systems. Zel'dovich proposed the idea in 1940 to use detonation as the means for combustion instead of deflagration based combustion in ramjet and rocket propulsion [1][2]. Frolov et. al experimentally validated the proposed increase in energy efficiency in their experiment on two different-size liquid rocket engine prototypes in 2015 [3]. Increased attention has been ongoing on the research, development, and testing of detonation based engines [4]. Private companies have recently begun their own investment and research and development on these systems. On December 14th, 2023, GE Aerospace announced the successful demonstration of their hypersonic dual-mode ramjet with rotating detonation combustion engine [5]. Over the last decade, significant strides have been made in the modeling, simulation, and hot fire testing of detonation based combustion propulsion systems. The objective of this project is to investigate vehicle system impacts in integrating a detonation propulsion system over a standard propulsion system of equal performance.

Detonation based engines can be described using the thermodynamic Humphrey cycle, rather than the Brayton cycle which is used as the foundation for jet and rocket engines operated today. Detonations enable an extremely efficient method of harnessing the chemical energy stored within a fuel and oxidizer mixtures [6][7]. Detonation occurs on a microsecond time scale compared to milliseconds required for traditional deflagration combustion systems. There is not enough time for pressure to reach equilibrium, therefore, thermodynamically, this combustion phenomena approaches a near constant volume process [6]. The Humphrey cycle adds heat at constant volume allowing for the

combustion process to occur without the gas expanding within the combustion chamber. This subtle change theoretically allows for more useful work to be extracted from the gas for the same amount of heat addition when compared to the Brayton cycle. During an ideal constant volume process, the heat added goes directly into increasing the temperature and pressure of the gas rather than expanding it. With the gas now at increased temperature and pressure the additional efficiencies in energy conversion in this process result in more kinetic energy and thus more work output (increased ISP, a key performance metric for propulsive systems). This provides increased thermodynamic efficiency compared to constant pressure processes where the heat energy does work against the surrounding pressure to expand the volume of gas.

Pressure gain propulsion presents a more thermodynamically efficient engine [8]. Detonation engines have been investigated for implementing pressure gain propulsion utilizing detonation waves to achieve higher performance and efficiency. A study done by Jones at NASA Glenn Research Center showed potential in reducing aircraft fuel consumption by 4-9% when using pressure gain instead of the pressure drop propulsion systems found in aircraft today [9]. According to Bureau of Transportation Statistics, the US Airline industry consumed 15.371 billion gallons of fuel at a cost of $43.602 billion United States Dollar (USD) [10] from the beginning of 2023 to the end of October 2023. Taking the upper limit of the potential fuel efficiency found by Jones in utilizing pressure gain combustion to commercial propulsion systems, this could result in a net 1.38 billion gallons of fuel saved and a total potential savings of $3.92 billion USD in in this time period alone. Although this report will focus on rocket propulsion, this highlights the importance of investing into researching and development of detonation based forms of propulsion beyond continuing to optimize deflagration based systems and achieving only marginal improvements relative to current state of the art.

Table 1.1: Airline fuel cost and consumption (U.S Carriers - Scheduled - 2023)[10].

Year	**Month**	**Consumption** (million gallons)	**Cost** (million dollars)
2023	January	971.1	3,233.5
2023	February	907.1	2,950.5
2023	March	1,065.1	3,120.6
2023	April	997.2	2,654.2
2023	May	1,041.8	2,549.1
2023	June	1,058.3	2,581.1
2023	July	1,108.4	2,768.1
2023	August	1,106.9	3,145.2
2023	September	1,004.4	3,171.1
2023	October	1,070.9	3,341.1
2023 YTD		**10,331.7**	**$29,514.5**

With the ever evolving need for more efficient systems, the rotating detonation engine has been extensively researched over the last several decades as a new propulsion system for many aerospace applications. The theoretical gains in propulsive efficiency and structural provide potential for reduced weight, reduced propellant feed system requirements, and increased fuel efficiency for rocket propulsion systems.

High efficiency rocket engines are of major interest for aerospace applications ranging from launch vehicles to CubeSats. For example, forms of efficiency may include

structural and mechanical efficiency, manufacturing efficiency or fuel efficiency. Fuel efficiency has major implications on vehicle system and mission design. The ability to integrate propulsion systems of equal thrust and higher fuel efficiency can result in more payload, longer range, increased flight operational time, more compact design, reduced costs and other performance gains. Hypersonic aircraft, missiles, and launch vehicles require high thrust systems. The standard propulsion system for these vehicles has been liquid bi-propellant rocket engines that require considerable amounts of on board propellant. Reducing fuel consumption without penalizing system or mission performance is the goal for any aerospace system. Detonation based engines have in large part been a theoretical solution to achieve increasing ISP compared to traditional rocket engines. These engine systems have been researched over the last few decades, particularly for defense applications. The front runners that have emerged in pressure gain propulsion are pulse detonation engines (PDE), rotating detonation engines (RDE) for air breathing applications, and rotating detonation rocket engines (RDRE).

Beyond fuel efficiency, it is important for aerospace subsystems to be as light weight as possible. Improving form factor efficiency without penalizing system performance reduces mass and volume requirements. A study by Ishihara et al. showed that when comparing the thrust performance of a RDRE with a steady rocket engine, the detonation engine combustion chamber length was shorter in length than the deflagration based rocket engine [11]. The dimensional specifications are outlined in the engine schematics in Fig.1.1.

Table 1.2: Comparison of thrust performance for different engine types [11].

Engine Type	Combustor Length (mm)	Thrust (N)
Detonation	$L_c = 0, L_{cc} = 15$	100 ± 6
Steady	$L_c = 15, L_{cc} = 200$	106 ± 6

High performance computing and new solvers capable of accurately modeling detonation physics are of key interest and are helping drive design understanding and flow field behavior. These advancements in simulation capability and accuracy enable research to be done more rapidly. Research can be accelerated on optimized injection schemes, wall chamber regenerative cooling channels, combustion stability response to transients, and overall engine performance of rotating detonation engines. In parallel, additive manufacturing has unlocked rapid design iteration due to the relatively rapid time scales in manufacturing over current approaches. Although this technology is early in its development, it has demonstrated to be a viable process for manufacturing RDREs [12] and ability to test new designs faster than traditional manufacturing methods. Furthermore, additive manufacturing enables engineers to rapidly design for many of the structural challenges that detonation based engines present, including extreme pressures, temperatures and vibrational loads.

As technology matures, RDREs present a feasible pathway to higher performance propulsion systems that are more fuel efficient, enable more compact mechanical designs lowering weight and size requirements, and enable longer range and extended flight operation over traditional rocket based engines in use today. These benefits can have major implications on aerospace and defense applications.

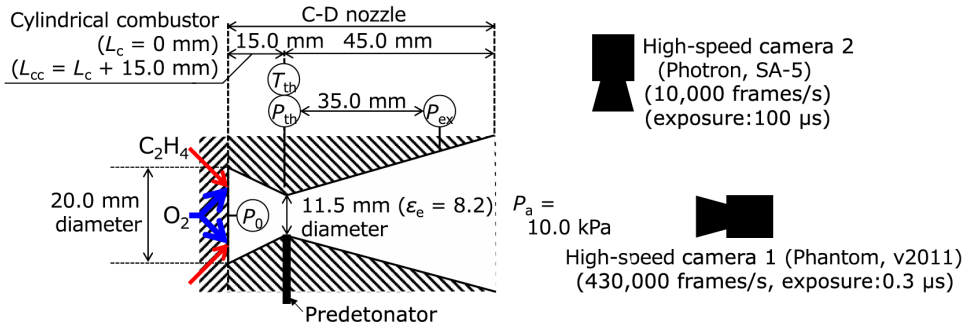

(a) Converging rotating detonation rocket engine.

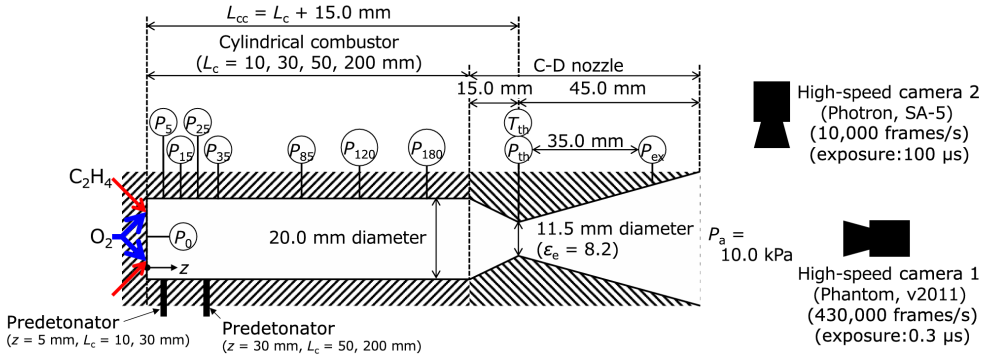

(b) Conventional rocket engine schematic.

Figure 1.1: Engine schematics [11].

1.2 Overview of Rotating Detonation Rocket Engines

RDREs use continuously revolving detonation waves to produce thrust. RDRE chambers harness chemical energy release more efficiently through controlling continuously revolving supersonic shock waves within a (usually) circular chamber. As these high energy waves travel around an annulus, they rapidly compress fresh mixture and provide even higher heat release compared to standard deflagration based engines. As the fuel and oxidizer mixture are detonated, resulting products expand at supersonic speeds. These systems present beneficial trades in terms of reduced subsystem components such as requiring turbo-pump machinery to produce the high pressures required by rocket engines operating on Brayton cycles through deflagration.

1.2.1 TRL Analysis

Although detonation based engines have been a theoretical solution over traditional Brayton cycles engines, they face challenges on their path to technology readiness level (TRL) 9. Current challenges include detonation wave stability, high temperature and pressure ratios inside the combustion chamber, acoustic loads and reliable injection of fuel and oxidizer. These challenges are being researched and investigated through high performance computing and experimental testing. TRL is a measurement system used in assessing a level of a particular technology [13]. Given the extensive research and

computational simulation capabilities over the last decade, the TRL of the RDRE system has made strides toward flight readiness. The end of the 2023 marked a major milestone in TRL advancement. NASA demonstrated major progress in a 233 second hot fire test of their 3-D printed RDRE [14]. The engine was able to generate 5,800 lbf of thrust for over 4 minutes. The article mentions the engine was fired to replicate a lunar lander burn or a deep space propulsion burn. According to NASA [13], this would put the current state of RDRE engines at TRL 5. TRL 5 is identified as a breadboard technology and must undergo more rigorous testing than technology that is only at TRL 4. Simulations should be run in environments that are as close to realistic as possible. TRL 6 is classified as a fully functional prototype. Definitions of other levels defined by NASA are found in Tab. **??**.

The extended hot fire demonstration of this effort out of NASA has marked a major milestone and has further validated the proposed capabilities and potential of the RDRE system. The most recent paper found outlining the current state of NASA continuous detonation cycle engine development [15] discusses milestones to date in 2022.

Table 1.3: Technology Readiness Levels (TRLs) defined by NASA. [13]

TRL	**NASA Definition**
1	Basic principles observed and reported.
2	Technology concept and/or application formulated.
3	Analytical and experimental critical function and/or characteristic proof-of-concept.
4	Component and/or breadboard validation in laboratory environment.
5	Component and/or breadboard validation in relevant environment.
6	System/subsystem model or prototype demonstration in a relevant environment (ground or space).
7	System prototype demonstration in a space environment.
8	Actual system completed and **flight qualified** through test and demonstration (ground or space).
9	Actual system **flight proven** through successful mission operations.

To further the TRL of RDRE systems and address uncertainty in the handling extreme heat loads NASA and IN Space LLC announced a collaborative partnership to explore additive manufacturing processes of high conductance copper alloys [15]. Teasley also provides an outline of the future work that was proposed for the FY23-24, the current time frame as of the writing of this project. One of the next steps was to demonstrate self-sustained cooling utilizing only propellants. Further efforts are underway to investigate nozzle design and annular geometry optimization to maximize performance and minimize loss. The ongoing success of this project demonstrates significant interest in the investment of more efficient propulsion systems.

NASA's fiscal year 2022 report on the RDRE project helped quantify the technology product capability. The annual review presentation by Perkins and Paxson [16] [17] provides technology product capability with an increased specific impulse of on the order 10% relative to conventional rockets. This can mean more fuel efficient systems coming in at lower weight or increasing mission duration. Options for higher performance are also being investigated as of 2022. RDREs operate at equal performance at reduced combustion feed pressure. Reduced fuel and oxidizer pump requirements can reduce part size, weight and complexity. Another favorable capability is the physical reduction in combustor length on the order 50% [18] relative to state of the art constant pressure engines. A diagram visualizing this comparison is provided in Fig. 1.2.

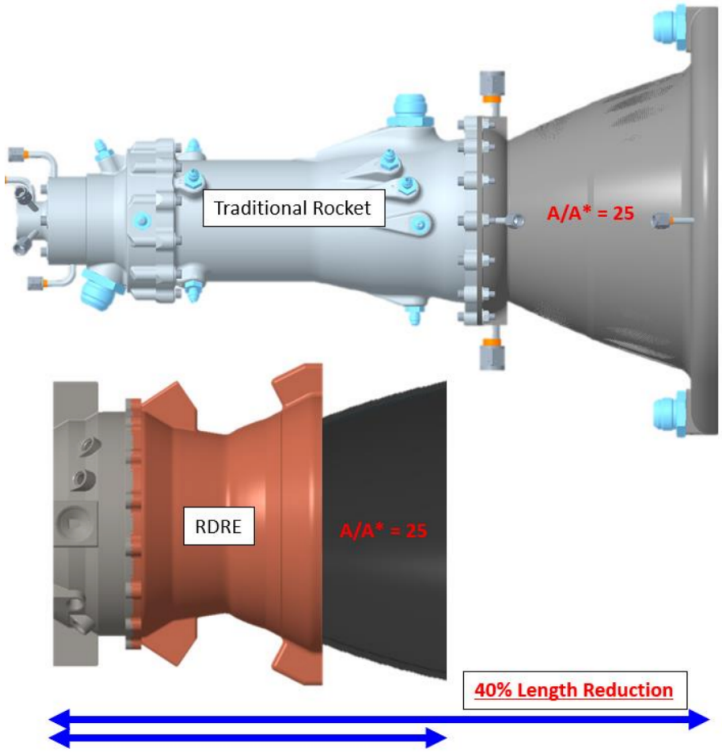

Figure 1.2: CAD visuals of two comparable engines showing reduced system length for the RDRE relative to a comparable constant pressure NASA WHALE engine. [18].

1.3 Purpose and Goal

This report details current literature to understand simplified theory behind supersonic detonative combustion, discuss the current progress in modeling, numerical simulation methods, experimental hot fire testing of RDREs. After a detailed literature review, an introduction into a simplified RDRE performance and sizing model is introduced. An introduction to the engineering analysis tool calibrated with free parameters anchored to experimentally validated qusi-2D CFD simulations developed by the leading NASA RDRE research team will be provided. This tool is implemented in MATLAB where it is used to compare predicted engine sizing and performance to a well studied RP-1/LOX deflagration engine design concept. The results of this study show significant RDRE gains when designing for equivalent thrust output. The code is also used to benchmark

prediction capability with available experimental engine testing data in literature. The program is then used to compute a large engine sizing and performance dataset by initializing a large multi-dimensional design parameter sweep. The results is performed using this computationally efficient numerical program to enable preliminary level propulsion system trade study analysis. Lastly, both qualitative and quantitative impacts of utilizing an equivalent thrust RDREs on a vehicle system architecture and mission design are presented. The goal of this project is understand underlying design philosophies and provide a preliminary design of an RDRE optimized for specified requirements.

The goal of this report is to provide insight into RDRE design considerations and highlight the potential impact these systems hold for the future of liquid rocket engine design. Results of an optimized engine for a specified thrust class will highlight the relatively small form factor and high performance density of these engines. Lastly, the work done in this report aims to enable further RDRE design optimization to be investigated, including improving and applying additional modeling capabilities to best assess the true potential innate to the driving physics of these engine systems.

Chapter 2: RDRE Theory and Core Concepts

2.1 Deflagration, Detonation Combustion Processes

Rocket propulsion systems harness tremendous amounts of chemical energy stored within propellants that are released during combustion. These systems harness the stored chemical energy and expel gases at high rates, typically out of a fluidic device, which enables rapid expansion and acceleration of flow. This exchange of momentum with the system provides thrust in the other direction. The fuel efficiency of a rocket propulsion system highly depends on how well the stored chemical energy is converted into kinetic energy of the combusted gas. For a set mass of fuel and oxidizer, the more efficiently this energy conversion takes place through combustion, pressurization and flow expansion, the better efficiency performance the engine will provide. This efficiency metric is also known as the specific impulse of the system. The specific impulse is defined as the integrated thrust over time for a unit weight of propellant as measured on Earth.

$$I_{sp} = \frac{F_{thrust}}{g_0 \dot{m}} \tag{2.1}$$

Maximizing this performance is critical for propulsion systems. Well known rocket engines such as the Rocketdyne F-1, Space Shuttle Main Engine (SSME) or SpaceX Merlin-1D combust fuel and oxidizer at extremely high pressures and temperatures and require a nozzle to then efficiently expand the flow after the combusted gas reaches sonic conditions at the throat. The combustion phenomena in these engines occurs with a propagating flame front that is subsonic. These subsonic combustion waves are also called a deflagration [19]. Deflagration waves necessitate heat conduction and radical diffusion as their main process through which mass, momentum, and energy are moved through the mixture [20]. Radicals are defined by Wilson and Fristrom as an atom or group of atoms, which, in chemical terms, has a free valency and may react to form a more stable molecule [21]. Radicals are considered to be highly reactive. For example, one can introduce radicals in the form of H or OH to an undisturbed mixture of H_2 and O_2 and a chain reaction can occur.

For example, deflagration waves travel on the order of 20 to 200 cm/s [19]. A heat or ignition source is used to achieve these processes through locally increasing the temperature to a point where combustion can occur. Combustion requires the mixture to be within flammability limits. Factors that affect flammability limits are the pressure, temperature, and chemical composition of the gas. Explosive or flammable mixtures are ones that can rapidly undergo oxidation (exothermic reactions). Fuel and oxidizer

mixtures undergo explosive reactions in conditions that are strongly dependent on the pressure and temperature of the system. When a premixed fuel and oxidizer system is exposed to an ignition source that increases the local temperature substantially, a reaction takes place. Apart from controlling temperature and pressure inside the combustion chamber of a deflagration based rocket engine, the maximum efficiency is dictated by the upper limit of how well a deflagration process utilizes the maximum potential chemical energy of the propellant mixture. This physical process is further discussed and is less efficient than the detonative form of combustion.

Combustion can also occur at supersonic velocities. When certain conditions are met, a deflagration wave can become a detonation wave. In a detonation wave, the main transport process is no longer reliant on the diffusion of combustion radicals and the conduction of heat energy. These transport processes take a relatively long compared to the process within a detonative wave. The heat release occurs almost instantaneously behind the shock front and the propellants are driven to higher pressures and temperatures more efficiently as entropy generating processes have less time to progress. Detonation differs from subsonic deflagration due to the supersonic prorogation of the flame front and significantly higher reaction kinetics. Qualitative descriptions of two types of combustion waves are provided in Tab. 2.1.

Table 2.1: Magnitude of flow parameter ratios in deflagration and detonation waves in gases[22].

Ratio	**Detonation**	**Deflagration**
u_u/c_u^a	5–10	0.0001–0.03
u_b/u_u	0.4–0.7	4–16
P_b/P_u	13–55	0.98–0.976
T_b/T_u	8–21	4–16
ρ_b/ρ_u	1.4–2.6	0.06–0.25
Note: c_u^a is the acoustic velocity in the unburned gases. c_u^a is the Mach number of the wave.		

The Mach number of a detonative wave propagating through an unburned gas mixture can reach values of 10. This has significant implications for propulsion as flow following a deflagration process requires a converging diverging nozzle to achieve supersonic expansion of exhaust gas. Furthermore, the burnt gas can achieve pressures upwards of 55 times the pressure of the unburned gas in a detonative wave. This large pressure gain can reduce pressurization requirements on an engine. The higher temperature ratios that occur through detonation also explain the further increases in efficiency of the detonative combustion process.

2.2 Detonation Wave Theory

Detonation waves are a difficult phenomena to exactly model, resulting in the usage of simplified models to analyze thermodynamic properties of a wave. A detonation wave is a discontinuity where the combustion front and shock wave are coupled. Several models have been theorized and tested to simplify analysis. Two most commonly used models are the Chapman-Jouguet and the Zel'dovich, von Neumann, and Döring (ZND) theory.

2.2.1 Initiating Detonation

Several conditions are required to provide a gaseous system to initiate and then sustain a propagating detonation wave. For example, if a tube is filled with an explosive gas mixture, a combustion wave can propagate when the tube is ignited at the open end. The open end ignition will cause a wave to propagate with some steady velocity [22]. If the ignition occurs at the closed end, and with a long enough tube, this deflagration wave can accelerate to a detonation. The following process describes the thermal initiation of a detonation wave [22].

1. Ignition at Closed End: Combustible mixture is ignited with a thermal source initiating the propagation of a deflagration wave.

2. Expansion and Compression Waves: Burned gas products have a specific volume on the order 5-15 times more than the unburned gas ahead of the flame front [22]. Given the burned occupies more volume per unit mass, the expansion from heat release generates compression waves that move forward into the unburned gas mixture.

3. Heating and Acceleration: Each preceding compression wave that arises from the expansion slightly heats the unburned mixture. The sound velocity then increases and the newly generated waves can now begin to catch up to the initial wave.

4. Development of Turbulence: As the preheating increases the speed of the traveling flame, the unburned gas is accelerated further and turbulence occurs. This turbulence can further enhance mixing and energy transfer amplifying the increasing velocity and acceleration of the unburned gas mixture.

5. Shock Wave Formation: This process eventually leads to the formation of a shock that is strong enough to ignite the mixture behind it. Given the mixture in the detonation front is highly compressed and also pre-heated, the rate of reaction is significantly higher than the deflagration front. When this rapid energy release from the combustion occurs, the wave is prevented from decaying, a self sustaining detonation wave is obtained.

This process is also called the slow mode initiation of a detonation wave, otherwise referred to as deflagration to detonation transition, or DDT. Direct initiation, or the fast mode [22] occurs only when an strong shock wave is generated by an external source. This strong shock wave must retain a minimum strength for a minimum amount of time. As stated in point 5 above, the immediate application of energy from the shock front can provide conditions necessary to detonate an explosive mixture. The critical parameter for this type of initiation is to have sufficiently high reaction rates.

2.2.2 Hugoniot Relations and the Hydrodynamic Theory of Detonations

The following section of combustion theory is outlined in detail in [19] and [22] provides a preliminary overview of the simplified model of a detonation wave. Propagation of a combustion front requires rapid reaction kinetics. The rapid heat release can maintain the the shock wave that drives the detonation wave front. The Rankine-Hugoniot

conditions are derived by modeling the discontinuity in the form of a flame is propagating through a gaseous medium in a tube. The wave is modeled as a 1-D, planar, and steady with unburned gases moving into the wave at a velocity u_1, equal to that of the propagating velocity of the wave in the laboratory frame. A schematic of this model can be seen in Fig. 2.1. The wave is thus considered to be fixed with respect to the tube. In other words, in the reference frame of the wave, it is at rest, and unburned mixture is moving towards and across the wave.

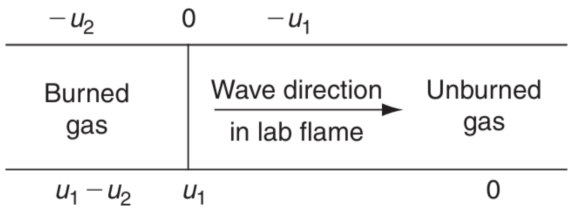

Figure 2.1: Detonation wave 1-D analysis configuration [22].

Table 2.2: Velocity components of 1-D planar wave system in laboratory and wave reference frames.

	Burned Gas	**Wave Front**	**Unburned Gas**
Wave Frame	$-u_2$	0	$-u_1$
Laboratory Frame	$u_1 - u_2$	u_1	0

$$\rho_1 u_1 = \rho_2 u_2 \qquad \text{(continuity)} \tag{2.2}$$

$$P_1 + \rho_1 u_1^2 = P_2 + \rho_2 u_2^2 \qquad \text{(momentum)} \tag{2.3}$$

$$c_p T_1 + \frac{1}{2}u_1^2 + q = c_p T_2 + \frac{1}{2}u_2^2 \qquad \text{(energy)} \tag{2.4}$$

$$P_1 = \rho_1 R T_1 \qquad \text{(state)} \tag{2.5}$$

$$P_2 = \rho_2 R T_2 \qquad \text{(state)} \tag{2.6}$$

There are 4 independent equations and 5 unknowns. The first three equations define the conservation of mass, momentum and energy of the system with the assumptions previously mentioned. The later two equations define the state of the gas. The unknowns in the frame of the wave front are: u_1, u_2, ρ_2, T_2, and P_2. An eigenvalue cannot be obtained and thus either the rate of reaction or a condition for the detonation velocity must be determined. Manipulating the equations as outlined in [19] provides the following two equations:

$$\frac{\gamma}{\gamma - 1}\left(\frac{P_2}{\rho_2} - \frac{P_1}{\rho_1}\right) - \frac{1}{2}(P_2 - P_1)\left(\frac{1}{\rho_1} + \frac{1}{\rho_2}\right) = q \tag{2.7}$$

$$\gamma M_1^2 = \left(\frac{P_2}{P_1} - 1\right)\left[\frac{1}{1 - \left(\frac{1}{\rho_2}\right)\left(\frac{1}{\rho_1}\right)}\right] \tag{2.8}$$

The Hugnoit Relation, Eqn. 2.7, shows that for some value of energy release q, and the known state of the unburned gas, there are a family of solutions that can be found the describe the state of the burned gas in terms of its density and pressure. A different curve on this plot is obtained for every value of $q \geq 0$. This curve is provided in Fig. 2.2. The plot can be broken down into three regions demarked by points representing different

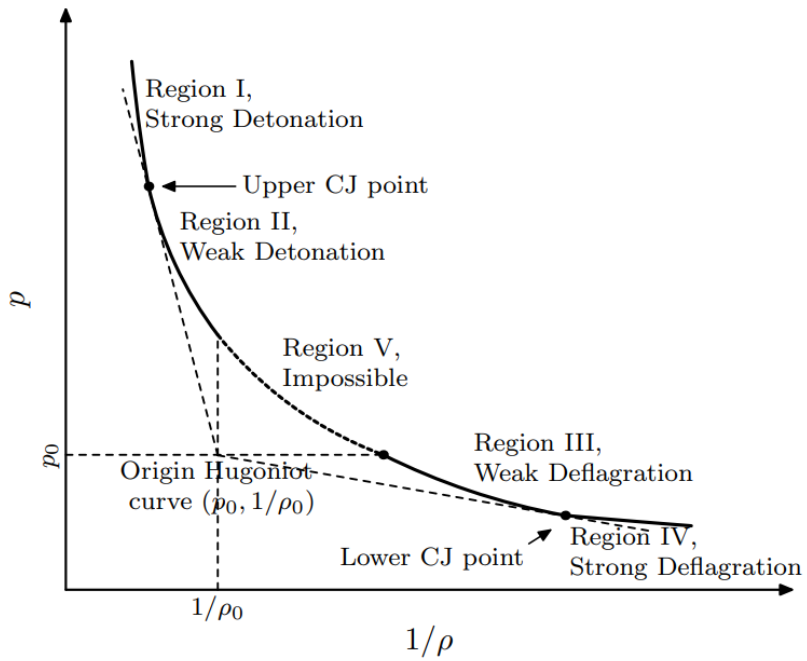

Figure 2.2: The Rankine-Hugoniot diagram [19].

potential end states of a gas behind a shock wave with specified initial conditions. The regions are broken down by two tangent lines that intersect at the origin of the Hugoniot curve. The origin is the state of the unburned gas defined by the pressure and density. There is also a horizontal and vertical line denoting constant pressure and specific volume respectively. Equation 2.8 dictates Mach number behavior depending on the solution on the curve. These regions outline the possible velocities that result from solutions that can exist on this curve. Regions I and II denote end states that are supersonic, i.e $M_1 > 1$. Recall, if the Mach number of the unburned gas is supersonic in the reference frame of the wave, the wave front is supersonic in the lab reference frame. Regions III and IV represent subsonic solutions, and region V is impossible since the value for M is imaginary according to equations 2.7 and 2.8.

In order to solve for all unknowns, another condition must be developed for the detonation velocity. Rearranging the continuity and momentum conservation equations, the velocity of the detonation is found using the following:

$$u_1^2 = \frac{1}{\rho_1^2}\left((P_2 - P_1)\left[\frac{1}{\rho_1} - \frac{1}{\rho_2}\right]\right) \tag{2.9}$$

Substituting this back into Eqn.2.2 provides the burned gas velocity:

$$u_2^2 = \frac{1}{\rho_2^2}\left((P_2 - P_1)\left[\frac{1}{\rho_1} - \frac{1}{\rho_2}\right]\right) \tag{2.10}$$

The particle velocity (Δu) is defined as:

$$\Delta u = u_1 - u_2 = \left[\frac{1}{\rho_1} - \frac{1}{\rho_2}\right](P_2 - P_1)^{1/2} \tag{2.11}$$

This value represents the velocity of the burned gas relative to the tube. Further dividing the particle velocity by the square root of the detonation velocity to obtain the following expression:

$$\frac{\Delta u}{u_1} = \frac{\left(\frac{1}{\rho_1}\right) - \left(\frac{1}{\rho_2}\right)}{\left(\frac{1}{\rho_1}\right)} = 1 - \frac{\left(\frac{1}{\rho_2}\right)}{\left(\frac{1}{\rho_1}\right)} \tag{2.12}$$

Depending on the downstream condition of the gas, this expression will dictate the value for the velocity of the burned gas particle with respect to the tube. For detonation regions on the Rankine-Hugoniot plot (see Fig. 2.2), where $(1/\rho_2) < (1/\rho_1)$, the right hand side of Eqn. 2.12 will result in a positive value. This result simply describes a compression wave where the downstream density is higher than the density of the gas upstream of the shock. The positive value of the right hand side of this equation also means the particle velocity (Δu) must have a positive value. As such, the burned gas follows the wave. On the other hand, if the resulting downstream density is reduced relative to the unburned mixture, the right hand side will now be negative. This means, the value of Δu must be negative, implying the particle is moving away from the wave. Given the burned gas particle velocity is positive moving with the wave, the model explains why detonation waves and combustion fronts are, in approximation, coupled. The energy release of the burned gas generates a compression wave, which continues to push the wave through the unburned mixture. This results in a self propagating phenomena. This is the physical phenomena taken advantage of to produce power in the form of thrust.

2.2.3 Chapman-Jouguet (C-J) Condition

Chapman postulated [22] the slope of the adiabatic process is a line that intersects at the Upper CJ point and another one that exists in the lower CJ point as seen in 2.2. This slope at point the upper CJ point can be found to be the following:

$$-\left[\frac{\partial P_2}{\partial(\frac{1}{\rho_2})}\right]_{s_J} = \left[\frac{(P_2 - P_1)}{(\frac{1}{\rho_1}) - (\frac{1}{\rho_2})}\right]_J \tag{2.13}$$

This relation can be used to also define the velocity of sound in the burned gas as:

$$c_2^2 = \left(\frac{\partial P_2}{\partial \rho_2}\right)_s = -\frac{1}{\rho_2^2}\left[\frac{\partial P_2}{\partial(1/\rho_2)}\right]_s \tag{2.14}$$

From Eqn.2.10 and Eqn.2.14, the velocity of the burned gases equals the speed of sound in the burned gas at the upper CJ point [22]. In the idealized approximation, pressure perturbations downstream of the shock can not propagate to the wave front itself, thereby

not being able accelerate nor decelerate the wave.

$$\left[c_2^2\right]_J = \frac{1}{\rho_2^2}\left[\frac{(P_2 - P_1)}{\left(\frac{1}{\rho_1}\right) - \left(\frac{1}{\rho_2}\right)}\right]_J = \left[u_2^2\right]_J \tag{2.15}$$

This makes the C-J detonation a steady state process as the sonic condition dictates that the detonation wave is self-sustained and conditions occurring downstream do not impact the wavefront. Above the upper C-J point, when the speed of sound in the unburned gas is higher than the speed of the detonation wave relative to the unburned gases, any rarefaction waves can propagate and catch up to the detonation front, reducing it's pressure and weakening the shock back to a stable C-J condition [22]. These overdriven states are transient. Thus, detonation waves are discontinuity propagation's that are supersonic and are sustained by the energy release from the chemical reactions directly behind the shock front. Given this solution for the detonation wave at the upper C-J point is the only steady state solution it is the condition used for experimental studies.

2.2.4 Experimental Observations on C-J Condition

The C-J model was implemented accounting for factors such as dissociation in the product composition and provided numerical estimations for detonation velocities comparable to experimentally measured results. Values for the detonation velocity are obtained by the Gordon and McBride Complex Chemical Equilibrium program [23]. The computed results are only slightly higher than experimental. These results indicate the theory predicted results aligns well with experimentally measured data.

Glassman discusses other experimental results showing density being the most sensitive upstream parameter when it comes to affecting wave speed. The density can be changed by varying the fuel and oxidizer mixture ratio thereby changing the wave speed. Looking at Tab. 2.3, the decreasing fuel to oxidizer ratio of $H_2$and O_2 indicates reduced wave speed. Several factors including chemical kinetics and reaction rates, physical and chemical parameters, and wave structure can explain these discrepancies.

Table 2.3: Comparison of calculated and measured detonation velocities [22][24].

Mixture	**Measured**	**Calculated**		
	Velocity (m/s)	Velocity (m/s)	P_2 (atm)	T_2 (K)
$4H_2 + O_2$	3390	3408	17.77	3439
$2H_2 + O_2$	2825	2841	18.56	3679
$H_2 + 3O_2$	1663	1737	14.02	2667
$CH_4 + O_2$	2528	2639	31.19	3332
$CH_4 + 1.5O_2$	2470	2535	31.19	3725
$0.7C_2N_2 + O_2$	2570	2525	45.60	5210
$P_0 = 1$ atm, $T_0 = 298$ K.				

2.2.5 Z-N-D Theory

The previous model, otherwise known as the Champman-Jouguet theory made the assumption that the planar detonation front was infinitesimally thin. Zel'dovich, Neuman and Döring proposed another model (ZND) during WWII [25]. The ZND model assumes

the wave as having a non-infinitesimal reaction zone that consists of the induction zone and reaction zone (also called the fire zone) as seen in Fig.2.3. The schematic in Fig. 2.3 shows the induction zone and the reaction zone following the shock front. The diffusion

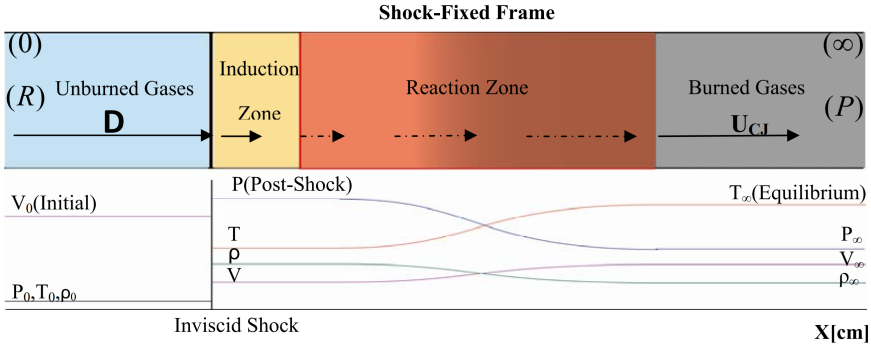

Figure 2.3: Schematic diagram including pressure, velocity, temperature and density in ZND detonation wave. [26].

effects of the flame are considered to be negligible due to the high velocity of these waves. The previous model did not factor in chemical reaction rates or structure [22]. This assumption was valid given the conservation equations in the C-J model did not place a restriction on the distance between the shock and the location of the generating force. In the ZND wave structure, one must now take into consideration the kinetics of the chemical reaction giving both a spacial and time separation of the front and the C-J plane of discontinuity.

The ZND models considers a detonation front traveling at a detonation velocity leaving heated and compressed gas behind it. As the unburned gas crosses the leading shock discontinuity, its pressure, temperature and density rise sharply. Following the induction period where the temperature rises and as the flow expands and initiates a reaction, the temperature increases further due to heat release from the reaction. The reaction is then assumed to be complete and in equilibrium as it reaches the C-J state where the reaction zone velocity has reached a local sonic condition [19]. Energy is generated behind the C-J state through thermal reaction. The change of states can be seen in the plot 2.4 as a function of distance following the shock front. The fraction of material reacted changes little at first and the state of the gas remains relatively flat

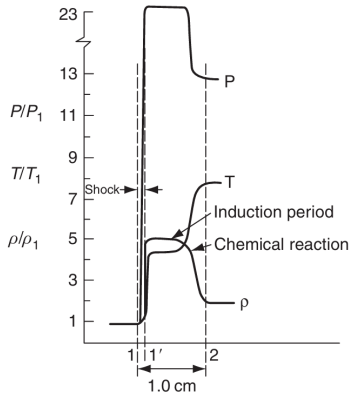

Figure 2.4: Physical Parameters through a detonation wave [22].

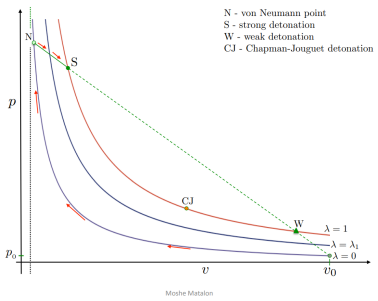

Figure 2.5: Hugnoiut plot parameterized by λ [27].

from just after the shock front through the induction zone. The reaction then begins to accelerate exponentially until it is completed at a high rate. For reference, a detonation wave propagating through a mixture of H_2 and Air with an equivalence ratio of $\phi = 1.2$ results in a calculated detonation velocity of 2033 m/s with a tube relative Mach number of 4.86. Inside the induction zone, the pressure ratio is calculated to reach 28 relative to the upstream conditions. The temperature inside the induction zone is computed by the ZND model to reach 1548 K and increase further to 2976 K after the reaction completes [22].

Matalon's lecture provides a simple breakdown for the possible solutions of the gas along the Hugnoit parameterized by λ [27]. Inspecting Fig.2.5, as the gas particle jumps to point N, it is on a shock-Hugoniot line corresponding to a $\lambda = 0$, the unreacted state. The reaction rate of an assumed one-step irreversible reaction is described by λ. For example, λ can be the mass fraction of the products species. At $\lambda = 0$, the gas is in its unreacted state, with a value of 1 defining a complete reaction. As reaction proceeds to $\lambda = 1$, the final state is the C-J state. The ZND model furthermore does not restrict over driven waves, or those where the velocity of the burnt gas exceeds the C-J velocity. This model works well at determining static parameters and is one dimensional in nature and provides a good point of departure for simplifying the analysis of a detonation wave. In reality, detonations exhibit a 3-D cell structure. [22].

2.2.6 Cellular Detonation Wave Front

Early experimental laser-Schlieren chromatography provided the ability to visualize three-dimensional cellular structures that make up all self-sustaining detonation waves [22]. THese cellular structures are a result of dynamic interactions between shock waves and chemical reactions. These repeating patterns of high pressure and temperature regions separated by reaction zones and shock fronts. These cells form strutures visualized through soot foils or high speed imaging techniques [22]. Each cell consists of tripple points seen denoted in Fig. 2.7b at regions A and B. Shock waves meet and lead to localized reactions and creation of this cellular structure. Detonation cells are inherent to a self propagating wave and as such are influenced by critical parameters discussed next.

2.2.7 Parameters that Control Detonation

One critical detonation parameter is the ignition energy supplied to the explosive mixture. Without a sufficiently high energy source, a reaction may not occur at a sufficient

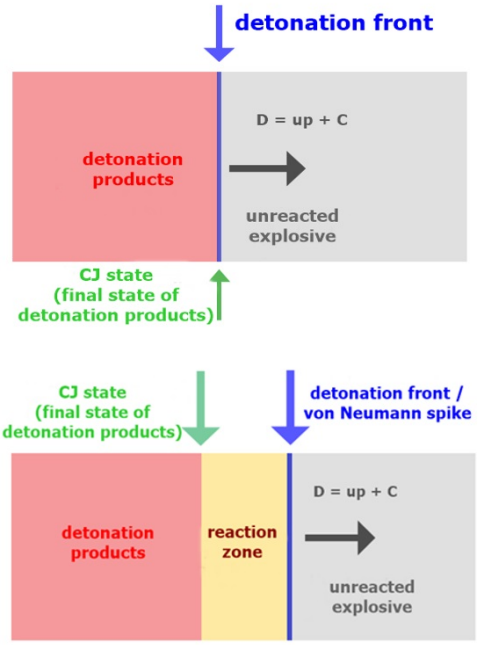

Figure 2.6: C-J Wave and Z-N-D wave diagram comparison [28].

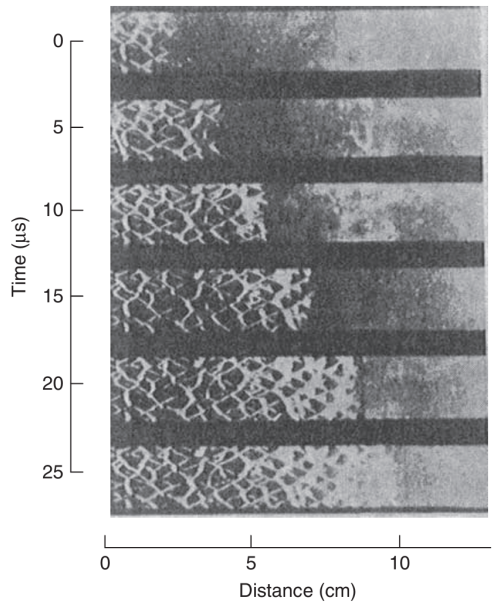

(a) Laser-Schlieren experiment capturing propagating detonation wave at several time intervals highlighting 3-D cellular structure.

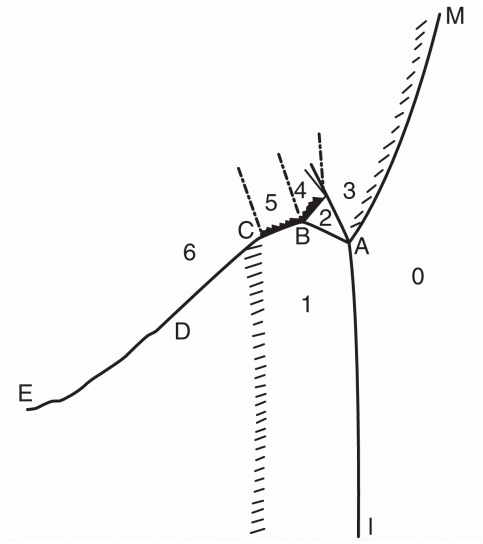

(b) Schematic of a cellular detonation front [22].

Figure 2.7: Cellular detonation wave front visuals [22].

enough rate to sustain energy release to enable the wave to self propagate. The wave can decay back to a deflagration and for example cause entropy gain in the system thereby decreasing efficiency of a engine system. From a physics standpoint, the decay of detonation to deflagration happens when the reaction zone decouples from the shock wave.

Mixture composition (equivalence ratio ϕ) affects reaction rates and detonation characteristics. For example, hydrogen has higher detonation velocities and smaller cell sizes compared to hydrocarbons. Another critical parameter to ensure detonation is the minimum diameter of the tube in which the wave is propagating. There does not seem to be an upper limit on the width or diameter of such a control volume, but detonation waves will collapse if the minimum tube diameter falls below a critical value, less than the size of a detonation cell, the wave can be quenched. This approximate value according to experimental data is reported to be about 13 times the length of the detonation cell size ($d_{critical} = 13\lambda$ where λ is the cell length).

2.2.8 Real World Phenomena in Detonation Wave Dynamics

Perturbations in flow parameters coupled with highly non-linear phenomena dynamically affect the wave system. As such, it is important to understand the origin of perturbations in real systems such as the combustion chamber of an RDRE. For example, small perturbations can arise from the upstream density changing due to imperfect mixing of fuel and oxidizer which can cause non-uniformity in the flow species and local variations in the density of the mixture [22]. Certain shock wave driven instabilities are seen to arise in real flow [29] [30] [31]. These are known as Richtmyer-Meshkov instabilities. When a shock wave passes through the interface of two gases, the sudden acceleration imparted on the interface distorts it. The disturbance of the interface causes instabilities which in turn can amplify perturbations in the flow. This leads to complex three-dimensional structures in the detonation. These structures can greatly impact factors such as the propagation speed and uniformity. Viscous effects from the injector and the highly dynamic state of the flow within the chamber can also lead to entropy generating events not accounted for in these simplified models. However, this and other non-linear phenomena can be investigated to a reasonable degree with high fidelity simulation and access to large compute resources. This will be discussed in the simulation and numerical modeling section to come.

2.3 Thermodynamic Cycles

Thermodynamic cycle analysis can be used to model idealized systems that have inherent thermodynamic processes involving transfer of heat and work into and out of the system. The state variables of the system (temperature, pressure, volume, entropy, enthalpy, internal energy, mass and density) are path independent meaning the change in the value of the state variable will be equal for any path taken in the state space. In other words, the value of the state does not care about the time history of the system to obtain the state. However, this is not true of the work and heat content into and out of the system. The amount of work done and heat transferred does depend on how the process was performed making it path dependent. For example, compressing a gas slowly via an isothermal process will result in different work and heat transfer compared to compressing the gas extremely rapidly at constant volume. A pressure-volume, or PV diagram, can be used to evaluate these processes by plotting the changes in the state of the system in thermodynamic equilibrium. This form of analysis typically assumes a closed cycle where:

$$\Delta U = E_{in} - E_{out} = 0 \tag{2.16}$$

By plotting the variation of properties for the closed cycle, a closed loop is formed with pressure on the y-axis and volume on the x-axis. The area enclosed in this loop is the work done by the process.

$$W = \oint PdV \tag{2.17}$$

By modeling a real process with these idealized assumptions, a first order approximation of the work done by a thermodynamic cycle in a closed system can be analyzed. In reality, actual systems have various entropy generating events that will reduce the overall efficiency of a cycle.

2.3.1 P-V Diagram Analysis

Standard engines in use are based on the Brayton cycle, where combustion takes place at constant pressure. As noted previously in this report, the conventional rocket engine utilizes a constant pressure heat addition process. Figure 2.8 provides a plot of the ideal Brayton and Humphrey cycle analysis. The resulting total entropy production in a Humphrey cycle is less than a Brayton cycle. Less entropy translates to higher efficiency. Kimura provides a break down of well known thermodynamic cycles [32].

The first thermodynamic discussed is the Brayton cycle. The initial state is point 1, the working fluid is pressurized through an isentropic compression leading to the state at 2b. From there, constant pressure combustion takes the fluid to state 3b where is undergoes isentropic expansion where it ends at the initial pressure. The cyclic nature of this process is brought to closure by assuming the refill of fresh mixture can be assumed to bring the system back to the original state.

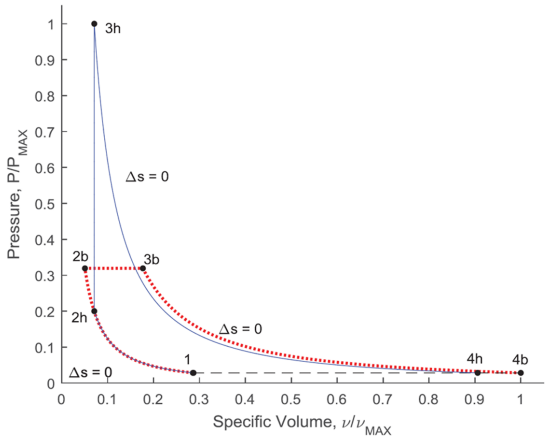

Figure 2.8: Thermodynamic cycles: Brayton (red - dotted) and Humphry (blue - solid) [32].

The Humphrey cycle is nearly identical to the Brayton cycle with the exception that 3b is replaced with 3h. The constant volume heat addition to obtain this state provides a higher working pressure allowing more theoretical work being extracted from the energy released into the system via combustion. As determined in the previous section on detonation theory, the detonation shock front represents a nearly isochoric compression of gas, resulting in higher pressures and hence pressure gain combustion.

Further analysis of an RDRE can be done by implementing the Fickett-Jacobs cycle [2][33]. Given the extremely rapid compression and combustion within a detonation

wave, the Fickett-Jacob's cycle can be seen to have a even higher point 3 and a slightly lower specific volume than in the Humphrey cycle. Wolanski provides the [2] theoretical efficiency calculations for each cycle in Table2.4.

Table 2.4: Efficiency comparison for different fuels in various cycles. Initial compression ratio of 5 [2].

Fuel	Brayton (%)	Humphrey (%)	Fickett-Jacobs (%)
Hydrogen–H2	36.9	54.3	50.5
Methane–CH4	31.4	54.1	59.3
Acetylene–C2H2	36.9	53.2	61.4

Cuciumita presents methodology and results a detonation propulsion system modeled with different cycles and considering real efficiency losses in by modeling entropy generating processes. The paper outlines the algorithms utilized to compute results such as theoretical efficiency, useful work and cycle specific heat for this detonation engine. Cuciumita also models the ZND process thermodynamically utilizing. The results of the real thermodynamic cycle analysis for an engine fueled by a stoichiometric mixture of air and acetylene are presented in Table 2.5. Analysis is done on the following models: H is the Humphrey cycle, FJ the Fickett-Jacobs cycle, and the ZND model. Assumptions were made on the efficiency loses and are outlined in the paper [33]. The ZND process model of this engine provided the largest net specific work.

Table 2.5: Net work, net heat and cycle efficiency. Initial compression ratio = 6 [33].

Model	Net specific work [MJ/kg]		Net specific heat [MJ/kg]		Cycle efficiency [%]	
	Ideal	Real	Ideal	Real	Ideal	Real
H	1.88	1.69	2.32	2.09	81.04	80.91
FJ	1.95	1.76	2.63	2.39	74.02	73.80
ZND	3.54	3.17	4.57	4.09	77.54	77.48

2.4 Detonation Engines

2.4.1 Pulse Detonation Engine (PDE)

Pulse detonation engines were the more extensively studied propulsion system utilizing pressure gain detonations to achieve propulsion [25]. Wolanski provides the following definition of a pulse detonation engine: PDEs consist of a sufficiently long tube, which is filled with fresh fuel–oxidizer mixture and ignited by a sufficiently strong energy source. The flame initiated by ignition must, in a relatively short time, accelerate to the detonation velocity, such that the transition from deflagration to detonation happens in a relatively small distance. Detonative combustion produces high pressure, which is converted to thrust [2]. The long tubes require the the combustion products to be evacuated and refilled before the next cycle is ensued. This results in detonations operating on a frequency of about 10-100Hz. Wolanski further outlines other PDE designs and their applications for turbomachinery, rockets, and other power generation systems. Due to this low cycle frequency and the requirement that products must be expelled and injection

and ignition have to happen again before the next detonation is a main reason a continuous rotating detonation wave harnessed within an annular chamber has been chosen as a design for propulsion systems.

However, given the majority of early research went into PDEs, the system has been experimentally flight tested. In 2008, a PDE was activated for 10 seconds to power an aircraft seen in Fig.2.9.[2]. The long pipe is seen extruding from the aft of the aircraft.

Figure 2.9: Long EZ Aircraft with PDE [34].

2.4.2 RDE versus PDE

A rotating detonation engine (RDE) takes advantage of the desired thermodynamic efficiencies of a propagating detonation wave by allowing the wave to propagate continuously along a cylindrical annular chamber. This design allows for detonations to revolve continuously rather than ending at the end of a pipe as done with a PDE.

Thrust in an RDE/RDRE is generated in a near continuous manner, compared to the pulsed nature of the PDE. PDEs operate on having to achieve cyclic deflagration to detonation transitions every pulse, thus their frequency of thrust generating detonations is about 10-100 Hz [2]. The frequency of RDEs can be on the order of hundreds to thousands of Hz. Given the detonation waves initiate once, they can propagate continuously as long as the fuel-oxidizer mixture is maintained in the cylindrical combustion chamber. RDEs are a more mechanically simple design as they do not require complex mechanical valve operation and timing. Furthermore, RDREs can be easily integrated into existing architectures.

A diagram visualizing the thermal gradient of gas within an cylindrical RDE in 3-D is shown in 2.10. As the detonation wave propagates around the annular thrust chamber, it comes into contact with fresh, unreacted gas. As the gas undergoes detonation, it continues propagating and expelling products at supersonic velocities along the axial direction of the cylinder.

2.5 Simulation and Computational Modeling

This section will provide an investigation of computational modeling techniques used to evaluate combustion physics, detonation wave stability and instability, injector modeling, engine performance and other critical flow field analyses. Simulation works hand in hand with testing. Numerical modeling can enable engineers to rapidly explore

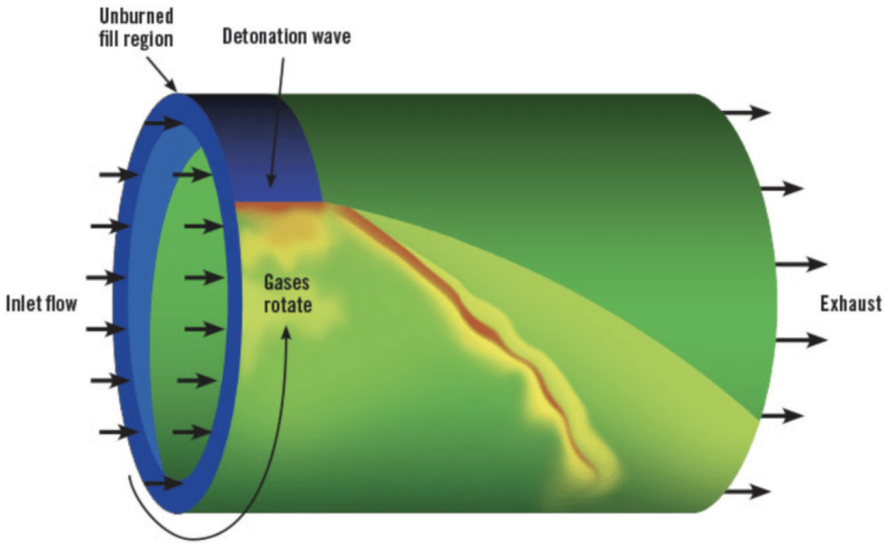

Figure 2.10: Diagram of a RDE [25].

factors that affect the flow field within an RDRE. However, numerical modeling is a fine balance of computational cost and model complexity, as well as solver algorithms and more. Numerical studies have been of growing interest for design space exploration due to the rapid ability to study the variation of design space parameters. Well known established design parameters for an RDE/RDRE are summarized [35] [36] as the following: fuel and oxidizer compositions, global equivalence ratio, mass flow rates, stagnation and back pressures, injector geometry and detonation channel geometry. Numerical simulations can enable engineers to understand performance variations due to these parameters in a relatively faster manner than building and testing. However, numerical models need to be verified and validated against experimental data to ensure confidence in simulation results. Simplified models such as [37] are an example of utilizing series of assumptions that reasonably simplify computations and decrease compute time and resource requirements while providing engineering level analysis capability.

Numerical simulations for RDREs in literature range in complexity and computational cost. 2-D are commonly performed as it simplifies the simulation volume. Given the RDRE is axially symmetric, the geometry can be unrolled from the cylindrical volume to a 2-D plane.

CFD enables researchers and engineers to simulate and easily visualize the flow field within the combustion chamber. This provides valuable insights and data that is otherwise more difficult to capture in experiment. A paper by Schwer et al. [38] utilized CFD to investigate the complex detonative flow field and effects of parameters on engine performance. These parameters were stagnation conditions and back pressure. Back pressure is defined in the paper as pressure at the outlet/exit plane. The stagnation pressure is the pressure at the inlet micro-nozzles at the bottom of the thermal gradient flow field plot provided in Fig. 2.12.

The analysis of this 2-D model showed detonation wave height and mass flow rate are primarily determined by stagnation pressure. Another paper by Paxson et. al demonstrated the use of simplified 2-D numerical simulation to investigate detonation wave speeds [39]. The study aimed to investigate low detonation speeds consistently observed in air breathing RDE experiments. Paxson at NASA Glenn Research Center, built a

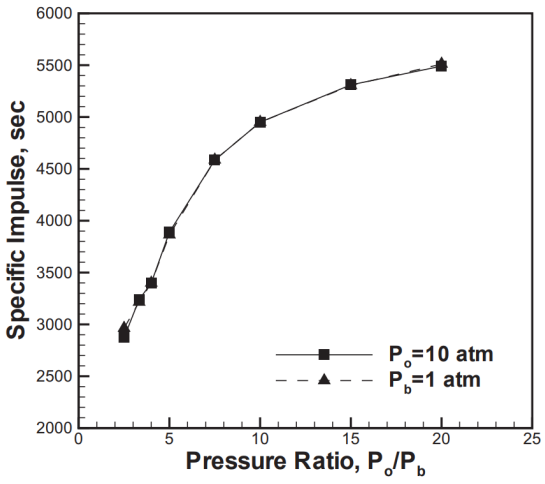

Figure 2.11: ISP vs. pressure ratio of an air-breathing RDE [38].

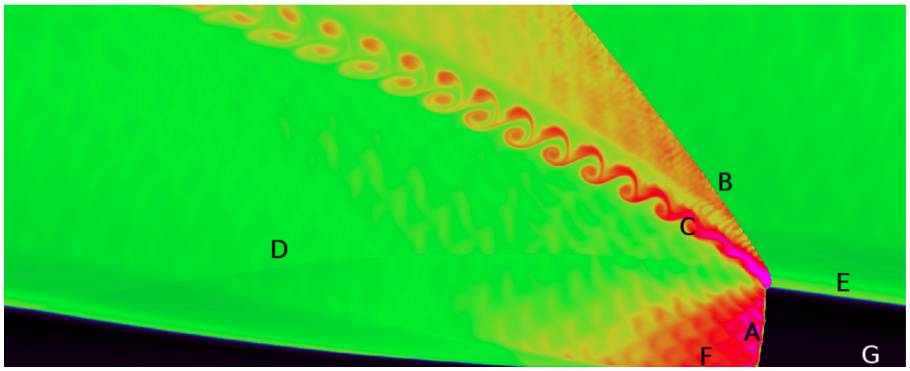

Figure 2.12: Unrolled RDE flow field from numerical simulation [25][38].

simplified 2-D CFD simulation with a reactive Euler solver to study these reduced propagation velocities. Paxson proposes [39] that lower effective reaction rates potentially caused by intense small scale turbulence is the primary mechanism for these reduced wave velocities. The most profound effect of turbulence is the enlargement of the reaction zone, or effectively a reduction in the chemical reaction rate. The detonation speed was found to be lower in a unique flow field analysis. Although the solver was not designed to model turbulence, it was able to provide useful information when used to examine the flow field's response to reaction zone enlargement and its effects on detonation wave speed, temperature, and ISP. The data from the numerical tool did show reduced reaction rates leading to reduced detonation velocities. It is stated that other methods for potential detonation velocity losses relative to predicted C-J conditions could also come from heat loss and variations to the fuel air mixture. In comparison with experimental results, numerical results also showed that a reduction in Wave-speed, however, does not alter the predicted performance of idealized RDE's as measured by their gross specific impulse. [39].

Other models requiring numerical solving have been built to specifically understand rocket engine sizing and performance estimates. Paxson and Perkins [37] built a simple an engine model characterized as essentially infinite number of sequentially firing pulse detonation engine (PDE) tubes arranged in a circumferential manner. The paper describes how each infinitesimal PDE is a lumped parameter chamber that execute a time dynamic

Atkinson cycle. The Atkinson cycle is a modified Humphrey cycle with an intake and exhaust stroke. The model implements various tuning parameters that can be set based on CFD results that have been experimentally validated. The flow down of this type of validation is important to understand and leverage appropriately. CFD codes implement various assumptions or may have grid quality issues due to restriction on the finite computational resources available. As such, certain simplifications or tolerance to some variability is allowed. High fidelity simulations must undergo verification and validation with either direct experimentally measured conditions or other prior validated test cases. This process provides a confidence level in computational modeling.

The result of their work showed that they have built a rapid design tool that can compute a converged cycle in under 1 second on a modern computer laptop[37]. This is significant as this model has been tuned using free parameters to closely match high fidelity CFD simulations and some experimental data provided by Brophy and Codoni from the Naval Postgraduate School in Monterey [40]. Given the model is based on PDE chambers, adding the requirement that the cycle time for each of the chambers must match the period of rotation for a detonation wave effectively determines the RDRE diameter [37].This can provide engineers with a rapid design tool to perform system trade studies on varying parameters. This tool can also model system sub-components such as turbopumps and cooling channels further demonstrating its simplicity.

An example was provided utilizing the RDRE blowdown model highlighting two comparable RP-1 and GOX engines. The outputs of the model computations can be seen in Tab. 2.6. The model was used to predict performance and sizing of a 190,000 lbf sea level thrust RDRE with an inlet manifold pressure of 1,250 psia. According to [37], there is not yet an established optimal value for length to channel hydraulic diameter ratio (LHDR) in the community. The engine was simulated for a ratio value of 5 and 2.5. This parameter essentially tells that for a set diameter engine, a lower value will result in a shorter engine as measured along its cylindrical axis. This parameter is also defined in the code as the aspect ratio of the RDRE (AR_{RDRE}). This will be the common notation for this geometrical parameter in the paper moving forward. Results in Tab. 2.6 provide

Table 2.6: Comparison of design parameters for different length to hydraulic diameter ratios [37].

	Engine A	**Engine B**
Length to Hydraulic Diameter Ratio	5	2.5
Mean Diameter (inches)	11.80	9.35
Specific Impulse Loss due to Heat Transfer (%)	3.0	1.2
Inner to Outer Diameter Ratio	0.8	0.7

interesting insights for design as this trend suggests improved thermal efficiency for reduced LHDR or AR_{RDRE}. With the reduced ratio between the inner and outer diameter, the resulting mean diameter of the engine was found to be lower as well. The results of this model suggest interesting design optimization for RDRE based on different applications. Further analysis was done on optimally sizing a nozzle for both configurations. It was found that although the reduced length engine had improved thermal efficiency, it required a longer nozzle than the engine of LHDR = 5. The two designs are seen in Fig. 2.13. This leads to further analysis necessary to understand potential losses in having to cool the larger length nozzle. It is possible that engine A from could indeed come out to be the more thermally efficient engine. Lastly, they describe how they were able optimize

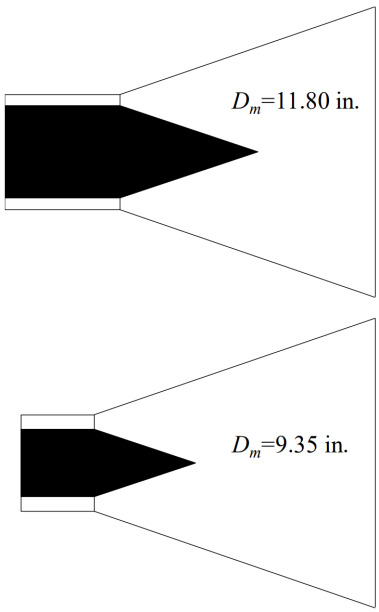

Figure 2.13: Notional RDREs of equal ISP but differing design dimensions[37].

cooling passages around a user defined limit on the maximum pressure drop allowed by the cooling passage system seen in Fig.2.14. Using iteration on the passage width and

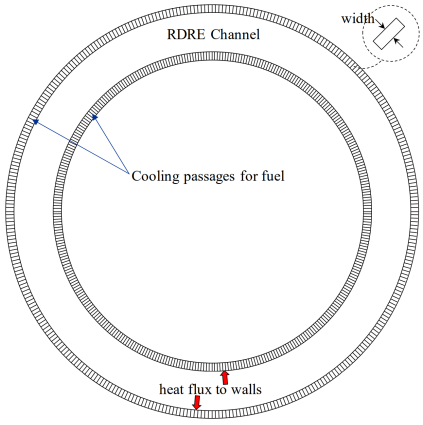

Figure 2.14: RDRE cooling passage schematic [37].

aspect ratio, flow properties within the passage are computed. These properties enable the pressure drop to be found for the cooling passage configuration that meets the specified target heat load. This optimizes cooling passage efficiency while meeting thermal management requirements. Setting the pressure drop of the cooling system equal to 20% of the inlet manifold pressure as the acceptable limit resulted in the following cooling passage outlet temperatures. Practical RDREs will require robust and reliable cooling systems that do not significantly degrade performance. The data provided by Paxson et. al gives insight regarding coolant passage design considerations. Initial results show that the shorter engine may suffer in increased nozzle design, but provide improvements in thermal efficiency and enable regenerative cooling while ensuring fuel is within coking limits. Robak [41] states that regenerative cooling with hydrocarbon fuels is feasible to a limit. This point is the upper wall temperature limit that prevents the fuel from reaching

Table 2.7: Outlet temperatures of fuel in coolant passages for different RDRE configurations [37].

Configuration	Outlet Temperature (R)
Engine A	1635
Engine B	1146

coking temperature. Fuel deposits can build up if these temperatures are reached, and the build up can result in engine failure due to decreased thermal conductivity of the coking layer that causes gradual increase in wall temperature past a failure point [41]. The temperature of the fuel in the cooling passages is crucial to consider during design as excessive build up of the coking layer can significantly impact flow rate and cooling performance. In fact, 3-D numerical simulations of hydrocarbon fuel cooled tubes showed non-uniform coking layer build up diameter [42].

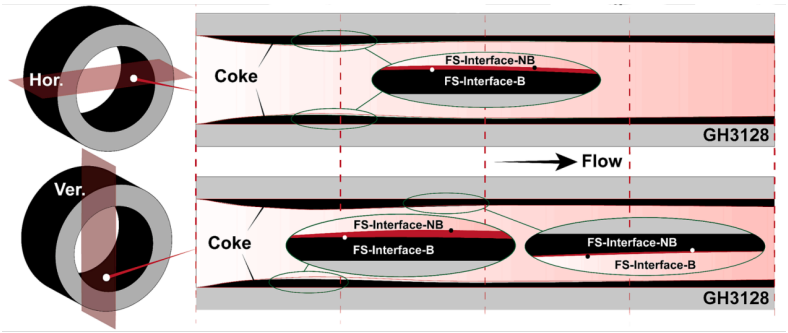

Figure 2.15: Visual schematic of coking layer within cooling tube from 3-D CFD showing two cross sectional planes [42].

Another technology goal to note from the latest available NASA project overview [17] was to modify existing 3-D CFD codes and develop validated modeling techniques for RDREs to allow simulations to be performed in one week or less on a workstation cluster. This recent technology goal highlights the current need to develop and validate a full scale, 3-D, high fidelity simulations that are not too computationally expensive.

Work was done around this same time, 2021, to address this current technology gap. Pal et. al [35] provide a CFD methodology to simulate full scale, non-premixed RDEs. One objective addressed was to develop a well validated CFD model for combustion in non-ideal RDEs that meets two requirements:

1. Sufficiently predictive in capturing the essential combustion dynamics and parametric trends in realistic 3D configurations

2. Computationally affordable to explore large design space.

To get an idea of what is computationally expensive, the Air Force Research Laboratory (AFRL) performed a 5-million CPU hour Large Eddy simulation of their Gen-1 RDRE. They found that simulations accurately predict the performance and behaviour of the physical experiments[43]. An image of the large eddy simulation from AFRL is shown in Fig.2.16.

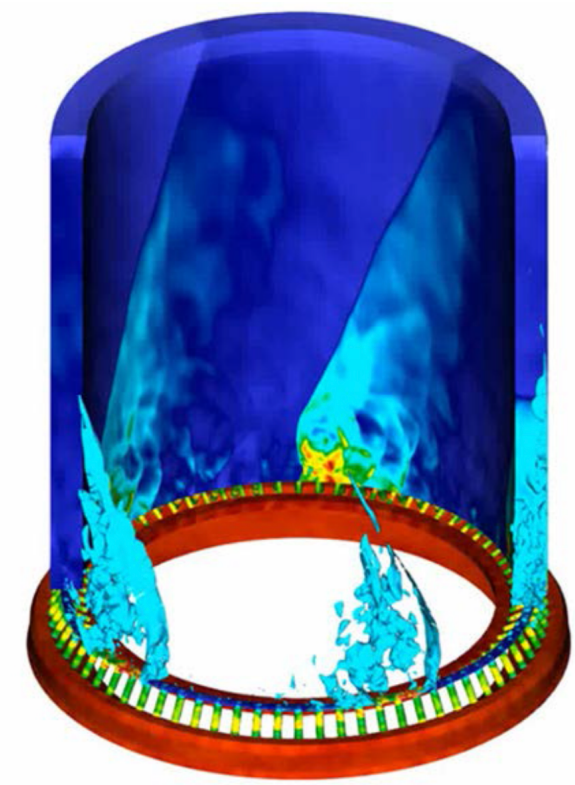

Figure 2.16: AFRL RDRE 5 million CPU hour large eddy simulation [43].

2.6 Experimental Testing

Various experiments have shown the validity of utilizing rotating propagation of detonation waves inside an annular chamber for efficient rocket propulsion. A paper from GHKN Engineering and Aerojet Rocketdyne [44] outlines an experiment where the primary goals were to design, build and test a continuous detonation rocket engine (CDRE) otherwise known as an RDRE used as the main acronym throughout this paper. The experiment aimed to provide measurements on engine performance, namely Isp and thrust for several potential fuels and gaseous oxygen (GOX). Several injector modules were also tested on machined brass and additively manufactured stainless steel. The nozzle configurations were also studied, including a straight and open annulus and several converging/diverging annular nozzles. They studied the effects of feed pressures, equivalence ratios and mass flow rates on engine performance for their different engine configurations. They present an assessment of the potential to use CDRE/RDREs for in-space propulsion. Over 200 hot fires were done in their experiment. Stable detonation was achieved for all fuel-oxidizer mixtures. They measured their engines to be about 80-90% that of the theoretical ideal value. Data in the experiment showed that the engine could remain stable even in the presence of acoustic or detonative interference [44]. This provided good insight into the stability of these engines as stability is critical for a TRL9 system.

The experimental setup is briefly discussed here.

Towards the end of the test campaign, Smith performed a pulse mode operation test. The laboratory thruster was fired with a roughly 19% duty cylce: 100 msec on, and 430 ms off. The tests done on the engine in pulse-mode operation showed the potential for utilizing these for reaction control systems. Reaction control systems require the ability

for the thruster to activate and deactivate rapidly, with a short time decay of operation to provide precision movements [44] [45]. In other words, the leading edge of an impulse signal from the engine control system from no-thrust to a consistent thrust state should take about 2ms to go from low to high state. As seen in Fig. 2.17 on the third row from the top, the commands sent to the valves upstream (before) the detonation chamber are square waves. The fuel and oxygen then begin to flow into the chamber, although with not as smooth of a waveform as the valve open commands. The detonation spark commands are then quickly pulsed at the tailing edge of the valve open command. The spark commands have a slight time delay from when the propellant flow rates have reached their operating condition. Given this engine was not designed for these pulse mode firings, the data still presents interesting insight into their start and restart behaviors, especially crucial for reaction control systems. The transient performance, or how well the engine performs under fluctuating conditions, was not a design consideration. Ultimately what this test aimed to demonstrate was the capability for repeatable, successive pulses that result in controlled detonation.

Of course, for a flight qualified engine, the manifold volumes and feed line lengths could be optimized to allow much tighter coupling between control valves and the injector. With tighter coupling between these components, the engine would instead provide much shorter pulse widths, shorter rise and decay times of the wave form, and much wider duty cycle range [44]. This is a beneficial design consideration for control systems that require rapid maneuvering, extremely responsive inputs, and reliable signal pulse width to not undershoot or overshoot a target signal value.

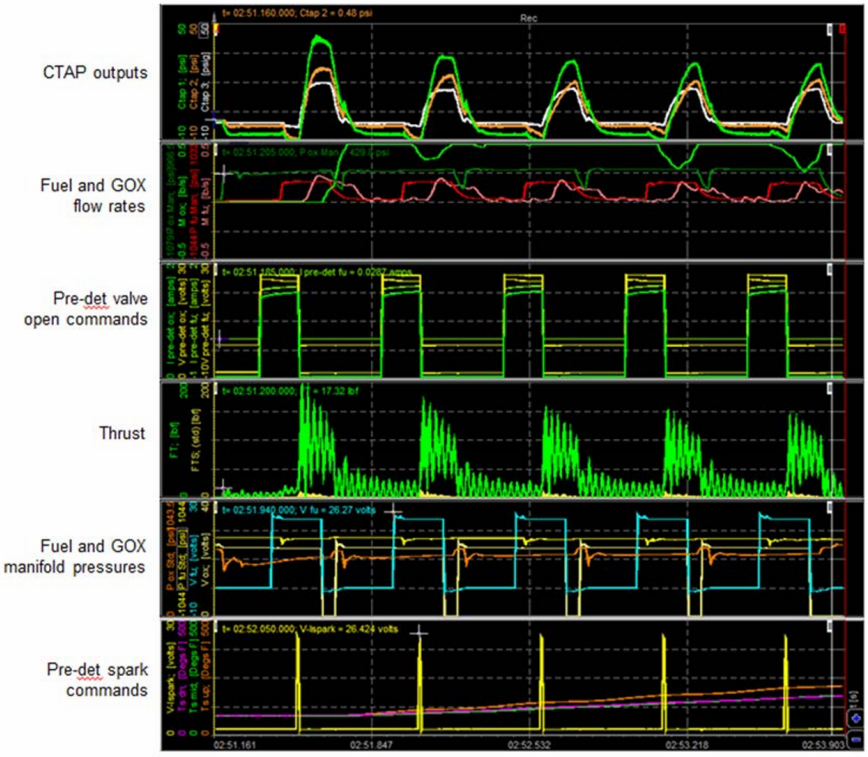

Figure 2.17: Signal response from Dewetron data acquisition system used in RDRE experimental testing highlighting pulse mode operation [44].

One key potential of CDRE as mentioned in this paper is that CDRE designs may be more easily scalable. Deflagration engines are difficult to scale to different thrust levels

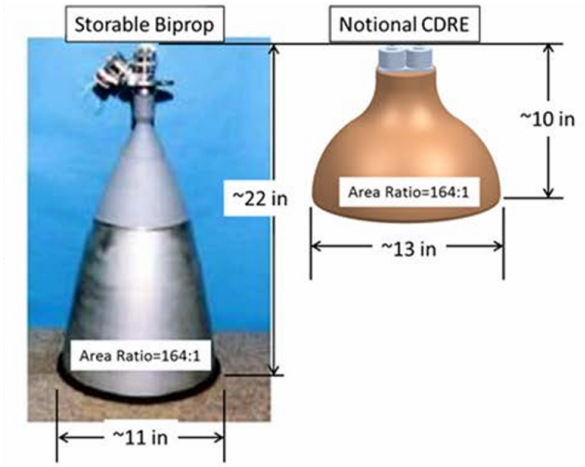

Figure 2.18: GHKN and Aerojet Rocketdyne developed a notional CDRE design for 110lbf engine for similar service of the R-4D-11 [44].

because of the sensitivity of deflagration burning to acoustic and detonation interference regimes that are specific to particular combustion chamber configurations [44]. The stability tests performed demonstrated insensitivity to imposed detonation shocks in the CDRE. Hence, as design parameters such as annular diameter and width are scaled, the fundamental mixing and combustion processes remain essentially unchanged[44].

They used experimental measurements and extrapolated data to design a notional CDRE to match the similar services of their 110 lbf thruster the R-4D-11. The notional design showed the total length of the CDRE thruster to be 10 inches compared to 22 for the conventional engine. The chamber length of the CDRE was 1.5 inches, compared to 5 inches for the conventional engine. From a system standpoint, this engine would have a favorable form factor, weigh less, and have less material to cool. The potential ISP of the CDRE was 30 seconds higher, 370s compared to 340s [44].

Thrust vectoring is another potential of RDREs. A paper from Daniau et al. presented the design of a continuously rotating detonation wave engine. They found that changing the local mass flow rate at the injection site should produce a thrust vector. Several months later this was verified with experiment [46]. This experiment was performed at the Lavrentyev Institute of Hydrodynamics in Novosibirsk where detonation wave rocket engines were already been studied for decades when the experiment was performed in 2006. Experimental data confirmed the engine having a 30% increase in the thrust-wall over pressure when doubling the mass flow rate. These results were reported to be lower than expected but this was due to the small diameter of the test engine. The small diameter of the engine limited the heterogeneity of the flow inside the combustion chamber. The paper states that for larger diameter configurations, 100% increase of thrust on one side compared to the other should be possible[47].

As discussed earlier in the theory section of this report, the density, or species composition of the upstream flow most significantly impacts detonation velocity. The number of detonation waves inside the chamber is thus also a function of the combustible mixture. Other factors including the geometry and mass flow rate also play a major role. Given the fact that changing the mass flow rate and injection pressure, or changing the mixture ratio of the incoming propellant, the velocity of the detonation can be controlled. The ability to control the number of waves is mostly dictated by the height of the fresh

mixture between two detonation waves. At higher injection pressures, the fresh mixture can make its way further away from the injector plate and actually support a new detonation [46]. On the other hand, reducing this height can collapse a wave and therefore reduce the wave count present in the RDRE system. By controlling the injection scheme the resulting thrust can be modulated within the chamber.

To investigate the thrust vectoring capability through experiment, different approaches were taken. The thrust had 100 mm (3.94 inches) internal diameter combustion chamber with 190 injection holes at the injector plate. The first approach was changing the equivalence ratio on one side of the engine, and the other approach utilized increasing injector diameters on one side to double the mass flow rate. A simple diagram (Fig. 2.19) displaying where the mass flow rate is doubled when viewing an cross section of the annular geometry perpendicular to its axis.

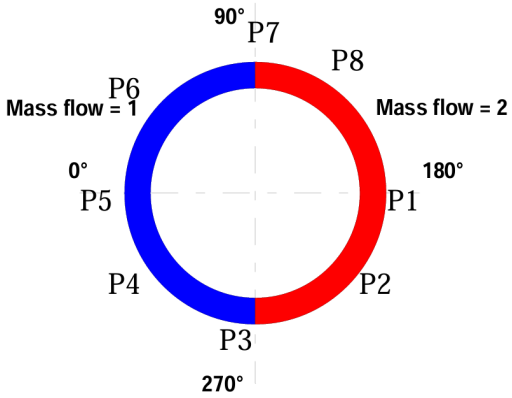

Figure 2.19: Diagram showing double the mass flow rate on the right hand (red) side of the annular chamber 2-D cross section [46].

This enables an interesting discussion regarding system design. The thrust direction and response time is therefore only limited by the response time of the injectors [47]. This opens different design possibilities. When looking at a conventional rocket propulsion system Fig.2.20 [48], the engine requires an extensive gambling system to provide thrust vectoring capabilities. There needs to be actuators, hydraulics, structural supports and other components just to provide a thrust vector. However, the potential of thrust vectoring through modulating injection around an annulus chamber can provide very unique and highly responsive handling capabilities. Something of interest to investigate is a thrust vector control system capabilities study. It can be interesting to investigate if increased vectoring rates at slightly reduced thrusts be more beneficial over a traditional gimbals system for an engine that is fully reliant on mechanically actuated thrust vectoring. Even further vectoring capability can theoretically be combined by mechanical and injection modulation working in unison.

It is important to note how stability tests were done to investigate how an RDRE responds to transients and phenomena that could ruin the operational stability. These experimental tests can also provide ranges of operational conditions that ensure stable operation. This can define boundaries on operational conditions and further improve design reliability and performance. Detonation waves were generated in the pre-detonation tube used to start the engine. These detonation waves were then fired into the chamber during its stable operation. The experimental data showed forms of instability such as wave reversal and wave slapping (discussed later this section). These observations were

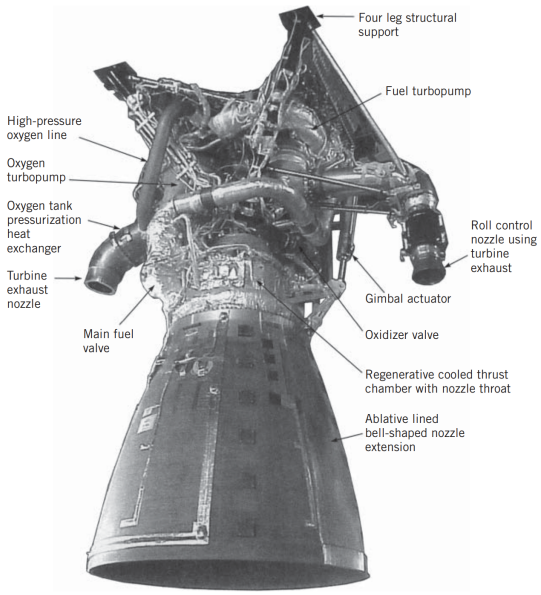

Figure 2.20: Gas generator cycle rocket engine RS-68 decomposition [48].

made using high speed cameras. What is interesting to note is the same amount of time and number of revolutions made by the wave were necessary to bring the engine back into a near stable state. This coincides with the measured behavior when testing the pulse mode operation of the engine. The overall takeaway was that RDREs seem to exhibit better stability to transients than standard liquid rocket engine combustion chambers [44].

Daniau, Falempin, and Bykovskii also experimentally measured the heat flux of this experimental RDRE with both Hydrogen and kerosene as the two operational fuels tested. Mean heat fluxes were reported in the range of 12 - 15 MW/m^2 [46], or about 1.2 to 1.5 kW/cm^2. To conceptualize the heat flux experienced by RDREs an simple order of magnitude analysis is performed. Assuming it takes approximately 3000 - 4000 watts to power a home at peak consumption, the energy flowing through just two to three square centimeters per second inside the chamber is enough to power an average American home at peak demand. Instantaneous heat flux is also of major concern at local points in the geometry where the detonation wave is passing. For a standard liquid rocket engine, the maximum heat flux occurs at the throat of the chamber where flow is maintained at sonic condition [45]. In a RDRE, the spacial location is changing dynamically with time. Although heating presents major challenges in design, the dynamic heat flux behavior enhances oxygen vaporization and increases mixing of fuel and oxidizer proving beneficial for efficiency, performance and detonation stability [49]. It was also reported in [44] that the stainless steel injectors experienced visual thermal degradation over the course of several hot fire tests. Experimentally measured heat flux, time averaged pressure, and visual instrumentation in the form of high speed cameras [50] greatly informs design and manufacturing decisions. Furthermore, this data can help validate computational models, increasing their prediction capabilities and reliability across different ranges of test conditions. Some beneficial takeaways of obtaining this data is solidifying cooling system requirements and driving correct material selection for specific mission needs.

2.6.1 Collective Experimental Efforts in RDRE Research and Development

This same engine design was later used as a foundation for a series of test campaigns out AFRL and several university research labs. A paper by Bennewitz et al. [50] presents a collective summary of experimental research efforts on rotating detonation rocket engines as of the year 2023. They were able to benchmark performance and standardize operability of rotating detonation rocket engines as they advance the system to flight demonstration. This impressive collective research effort includes the AFRL, University of Central Florida (UCF), Purdue University and University of Washington. It was found that ongoing experimental RDRE research campaigns across multiple facilities have confirmed consistent operation and has set a standardized framework in validating RDRE architecture performance. This experimental progress is showcases the value of the results across these experimental engines. Key findings about RDRE design, performance, detonation wave physics and other considerations are presented as follows.

Experimental findings from this test campaign across different institutions compares well with experimental data published by NASA. Specific impulse performance gains of about 10% compared to a traditional constant pressure engine. There was further validation through this work on improvements in system form factor improvements and potentially measurable weight savings compared to their constant pressure counter parts. These gains will become increasingly more clear as more research into RDRE operation and cooling become better understood. Although there are numerous experimental data and research already being or has been done on operability and performance, injection response, detonation structure, measurement techniques and other studies, they mention there was no real coordinated effort to unify results [50, 51, 52, 53]. The following unique scientific challenges due to detonation combustion are discussed in detail.

- Stability and strength of waves.
- Flame-acoustic coupling means highly non-linear physics such as chemical reaction kinetics, local inflow boundary conditions and reactant mixture ratio.
- Wave dynamics have large-scale sensitivities (for example inflow conditions) that impact performance.

Understanding these challenges and how to mitigate is crucial to maximize RDRE potential. This unification was undertaken by gathering results through close replications of operating conditions for RDRE verification and validation. Four separate propulsion facilities performed experiments on the same 1350 N-thrust (303.5 lbf) class RDRE. The engine schematic and a hot fire test can be seen in Fig.2.21.

Three operating conditions and a transition regime were tested to encompass varying performance levels and detonation stability and detonability within the engine. The conditions are summarized in the the table below 2.8. The variation of flow rates at constant equivalence ratio further demonstrated stable detonation across different operating conditions. The data also showed consistency across different test engines.

Conditions within the RDRE are controlled by altering the equivalence ratio ϕ and propellant mass flow rate $\dot{m}_{\text{tot}}$. The equivalence ratio is defined as the ratio of the actual fuel/air ratio to the stoichiometric fuel/air ratio. Stoichiometric combustion occurs when all the oxygen is consumed in the reaction, and there is no molecular oxygen (O2) in the products. If $\phi = 1$, the combustion is stoichiometric [54]. Optimal performance of

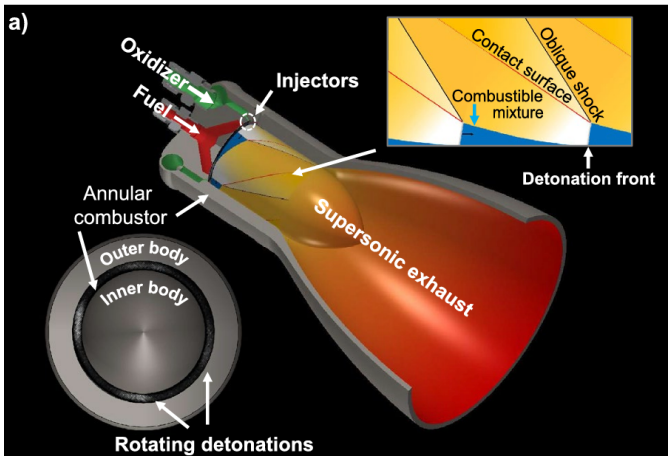

(a) Experimental RDRE hardware schematic.

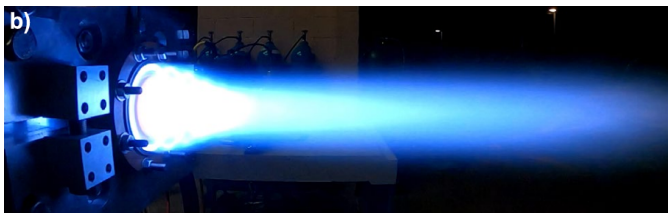

(b) Experimental RDRE hot fire test.

Figure 2.21: RDRE hardware schematic and example hot fire test picture [50].

the experimental RDRE was found for equivalence ratios between 1.1 and 1.7, fuel rich mixtures of gaseous methane and oxygen. These trends may be different for different propellant combinations. This is something to investigate further. The transition condition as mentioned earlier, was achieved by increasing the mass flow rate and thereby inducing a mode transition from two to three stable waves. The experimental data suggests that higher equivalence ratios result in higher mode excitation levels with more waves in the chamber. A plot provided by Bennewitz shows the number of waves photographed through a high speed camera facing the combustion chamber as seen in Fig. 2.22. It can be seen that excitation begins to occur after a mass flow rate of about 0.300 (kg/s). This plot is for an equivalence ratio of 1.1. The corresponding wave speed as a function of total mass flow rate is also provided. The wave speed decreases slightly as total mass flow rate is increased.

2.6.2 Mode Transitions Measured in RDREs

Mode transitions serve as an interesting innate operational capability of an RDRE. Understanding modal transitions and wave count present in the combustion chamber and how this affects performance, stability, and efficiency are important to measure, understand, and optimize for. Furthermore, outlining ranges of operable conditions on ϕ, $\dot{m}$ and injector pressure P_{inj} or manifold pressure P_{man} can inform design requirements on engine control subsystems. More thrust can be achieved with higher wave counts present at a given time. As such, the thermal and structural loads on the engine will increase. This in turn, will drive cooling system and pump feed system design. Other factors such as stable operation need to be considered and measured accurately. When

Table 2.8: Engine dimensions and test conditions [50].

Design Dimensions		
Parameter	**Specification**	
Outer Diameter	76.2 mm	3 inches
Length	76.2 mm	3 inches
Annulus Width	5 mm	0.2 inches
Injector Elements	72 pairs	Unlike flat impinging injector element pairs, inclined 30 degrees from axial centerline
Test Conditions		
Condition	**Equivalence Ratio** (ϕ)	**Total Mass Flow Rate** ($\dot{m}_{\text{tot}}$ in kg/s)
Condition 1	1.1	0.272
Condition 2	1.7	0.272
Condition 3	1.1	0.270 - 0.375
Measured Performance Results		
Parameter	**Value**	
Thrust Range	350 - 625 N	
Specific Impulse	125 - 175 s	
Experimental Uncertainties		
Parameter	**Uncertainty Range**	
Equivalence Ratio	0.5 - 6 %	
Total Mass Flow Rate	0.3 - 2.5 %	

Table 2.9: Equivalence ratio and combustion condition [54].

Conditions	**Combustion Condition**
$\phi < 1$	Lean with excess air/oxidizer
$\phi > 1$	Rich with incomplete combustion

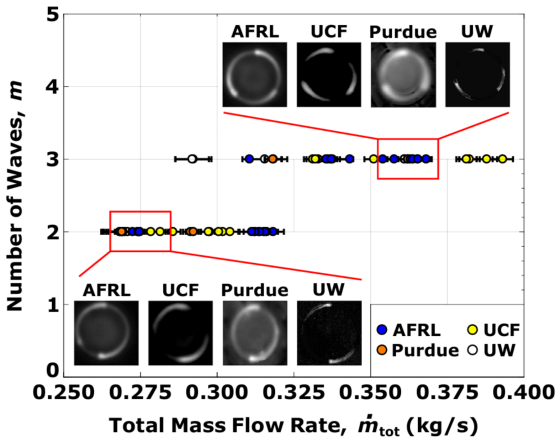

Figure 2.22: Detonation mode characteristics from AFRL, UCF, Purude and UW RDRE experimental testing standardization effort [50].

varying mass flow rates, equivalence ratios could temporarily change and a too lean or rich mixture can in turn destabilize the wave. Optimizing for smooth and efficient transitions between these operating modes will ensure more stable and reliable operation. This will also drive injector design requirements to ensure flight ready engines with high throttle ranges can operate stability at different flow rate and pressure inputs. Geometry also influences the wave propagation and interaction with the chamber walls and other waves and dynamic flow field regions. Ensuring parasitic reflections and wavelets are minimized for given geometries can also be studied through test campaigns. Lastly, the modal transitions themselves introduce sudden changes to the system, which typically can lead to instability. Hot fire test data for modal transitions will inform monitoring, sensory and control system design considerations. As such, this phenomena is to be investigated through discussion on experimental work in this field.

Bennewitz et al. provide an in depth study on modal transitions in the same engine outlined in Tab. 2.8 with increased flow rates up to 0.454 kg/s. Modal transitions occur when the number of waves in the combustion chamber changes or their direction changes. As discussed, these changes can occur due to changes in inflow conditions, geometry, and other factors. Detonation waves can also interact with each other, wave consumption, wave merging and wave separation can take place [49]. Given modal transitions are unsteady events they can negatively impact engine performance. Three transitions are explored in this paper. Certain flow conditions can lead to reversal in the direction of rotation, increased wave count and decreased wave count.

The first is a rotational direction reversal. This happens when the wave number is maintained but changes rotational direction. It was observed in the hot fire tests that the rotational detonation reversal has intermittent counter propagating behavior. As this transition takes place over some finite period of time, two opposing sets of waves become active and the original set of waves eventually dominates. Further analysis is found that wave consumption takes place when a parameter $\delta\theta'$ and corresponding cyclic acceleration increase. This causes one wave to accelerate into another wave and consume it. Given there is not enough local reactant to sustain both waves, they merge into one. This experiment provided a focus on the instantaneous behavior of modal transition waves.

Understanding these modal conditions helps better understand the results of the paper previously being covered [50]. This experiment across all facilities was done on two or three wave excited modes. With inlet conditions consistent across all experiments, measurement and flow metering techniques were standardized. Overall uncertainty across measurements in this experiment were cited to be 0.5% to 1.5%. This showed good agreement in performance results across the different facilities. Consistent local inflow boundary conditions are stated to be critical for uniform detonation amongst all tested engines. The engine performance summary showing thrust and specific impulse for three different engine experiments as a function of mass flow rate at constant equivalence ratio including their uncertainties are presented in Fig.2.23. The trend shows thrust and specific impulse measurements are all tightly grouped providing proof that robust engine operation is achievable despite the complex nature of detonation physics and early technology readiness of RDREs. The paper also discusses high speed imaging and post processing standardization.

It is desired to have higher detonation wave speed as increased wave speed results in more efficient combustion of reactants. A paper by Chacon et al in 2019 studies the parasitic combustion with an optically accessible continuous wave rotating detonation engine. Experimental results indicated that the reduction in wave speed and pressure

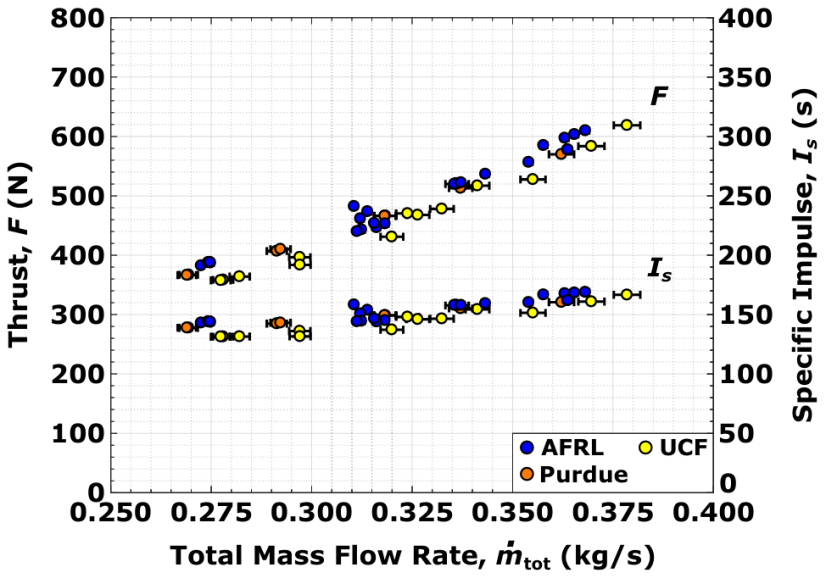

Figure 2.23: RDRE performance summary from experimental hot firings across multiple facilities indicating close alignment and standardized testing capability [50].

ratio is consistent with existence of this non-ideal combustion [55]. The heat released by the parasitic deflagration is not utilized by the detonation wave reducing the overall pressure rise.

Bigler et. al [56] did a study focusing on the global performance effects of these modal transitions on rotating detonation rocket engines. Given the study [49] and what is known about detonation combustion, [55], it would imply that increased wave mode transition should result in reduced performance. In their experiment, they found that although wave speed was in fact reduced, the measured thrust and specific impulse of the engine increased with increasing wave count. The paper discusses that measurements and thermodynamic analysis were done to further understand mode transitions.

Along with the experimental testing, Bigler et al. built a thermodynamic model. They marked three portions of where heat release takes place. This is before, during and after the detonation wave. A sensitivity study was done by varying these three parameters to examine the effects on detonation wave speed and ISP of the engine. A reduction in heat release before or after the detonation results in decreased wave speed. Wave speed is tightly coupled to the heat release during detonation. The parameter that most affected ISP was the pre-detonation heat release, meaning parasitic deflagration is more of an impact to engine performance than wave speed. Their thermodynamic models show that it is still possible to achieve higher performance with higher wave speed and reduced wave count. Bigler states that there is some optimization between detonation wave speed and number of waves, possibly due to a decrease in the spacing between the waves corresponding with a decrease in the amount of parasitic deflagration in the annulus.[56]. Therefore, there seems to be an optimal wave count for different chamber sizes. Minimizing the space between the waves reduced potential for parasitic deflagration, however. As wave count goes up, wave speed goes down and there is less space for deflagration. There is a trade to be done between these parameters as maximizing wave speed is still desired. The authors state that once an optimal wave count is determined for a geometry, an increase in wave speed is expected to be directly correlated to engine

performance [56].

The experiment was done across a wide range of input conditions. ϕ is varied from 0.5 to 2.0 with constant mass flow rate of 0.6 lbm/s. Mass flow rate is also varied from 0.25 lbm/s to 1.0 lbm/s while holding a constant $\phi = 1.1$. The following results are summarized in Tab.2.10 from [56]. At these operating conditions, an increase in wave count and decrease in wave speed results in an increase in thrust and specific impulse.

Table 2.10: Summary of RDRE performance from experimental testing on mode transition [56].

Test	Thrust (lbf / N)	ISP (s)	Wave Speed Change
A (Two Wave)	82.6 / 363	141.6	-
H (Three Wave)	126.3 / 556	165.1	-
Mode Transition Average	5.3% increase	5.3% increase	12% decrease

Although across all mode transitions from two to three waves resulted in improved performance, performance can not be solely attributed to the operational mode. Thrust and specific impulse also increase with increased mass flow rate. The conclusion is that optimal configurations need to be determined for specific cases.

2.6.3 Experimental Data Processing Techniques using High Speed Imaging

To better characterize complex detonation propogation and unsteady modal behavior, high speed visible imaging into the annulus was used. A separate paper by Bennewitz et al. provides a detailed overview of these imaging techniques and equations used to process image data [57]. Bennewitz et al. reported three major challenges present in extracting finely resolved quantitative details about detonation modes in an RDRE. One of these challenges was the manual processing of large datasets that needed to be automated. They also cited challenges in camera stability and with delineating wavefront from the background. The automated method developed will be introduced with the goal of providing insight into effective methods of experimental testing and analysis crucial to perform efficiently during research and development.

The pixel intensity data is processed and then populated into 200 azimuthal bins around the annulus. Each bin covers an angular location and the intensity of the visible light signal is integrated and then digitally processed to track wave location. Each bin provides an intensity value for 1.8° coverage of the annulus. The camera is mounted 6.1 meters downstream of the RDRE exit. The camera is enclosed by a quartz window and is focused into the annulus on the injector plane. The paper cites using a Phantom v2511 high speed camera (HSC) equipped with a Nikon Reflex Nikkor HN-27 lens. The images are recorded at 200,000 frames per second with a resolution of 256 x 256 pixels. This information is summarized and provided in Tab. 2.11. These techniques are useful in the successful testing and development of future systems. Furthermore, these methods are non-invasive into the chamber or critical structural components of the engine.

RDRE High Speed Imaging Configurations	
High-Speed Camera (HSC)	Phantom v2511
Camera Location	6.1 m downstream of the RDRE
Enclosure	Quartz window
Lens	Nikon Reflex-Nikkor HN-27
Frame Rate	200,000 frames per second (kfps)
Resolution	256×256 pixels
Exposure Time	1 to 3 µs
Field of View	Entire RDRE annulus

Table 2.11: High speed imaging configuration and specification for experimental RDRE testing and image processing [57] [49].

Chapter 3: Computational Approach to RDRE Performance Analysis

This following chapter serves as an overview of the simplified RDRE model code developed by Paxson et al. out of NASA Glenn Research Center [37]. This code will serve as the centerpiece of the analysis, design and discussion in the rest of this report. This code was obtained from the NASA software catalog [58] and was briefly introduced in the previous chapter. The discussion that follows will investigate the driving assumption and physics, governing equations, and other critical components of the RDRE blowdown model. The discussion on the methodology behind development of this computational engineering level analysis tool will be provided as well.

3.1 Engineering Level Analysis

3.1.1 Introduction

Simplified engineering level analysis codes are well suited for use in early design phases of a project due to their efficiency and modularity. Simplified computational models can now be solved rapidly on most engineering computers today. This enables engineers to more rapidly design near optimal optimal system level designs for specified mission requirements. CFD was not selected as an analysis and simulation tool for this project due to the relatively longer computational time requirements and less flexible means of evaluating overall system performance for specified sizing. Performing a large design of experiments in CFD would have been too computationally expensive. Although the model introduced in this chapter utilizes approximations and assumptions that do not reflect the complex nature of these propulsion devices, methodologies have been taken place to provide reasonable accuracy in predicting performance without sacrificing computational cost.

As briefly introduced in the prior chapter, experimentally validated quasi-2D (Q2D) CFD simulation results provide points of anchoring physical parameters for the model. The work done by Paxson et al. directly represents an effort to meet the need for a simplified model that can compute performance, flow rates, physical dimensions and other important factors of a RDRE. The implications of fulfilling this need are multifaceted:

1. **Initial design phases:** Provides engineers the ability to make preliminary design estimates and decisions without requiring complex and expensive simulations.

2. **Integration with other systems:** Enables the integration of propulsion system design into the broader system architecture analysis. Understanding sizing, fuel consumption, thrust and other key performance metrics will drive the system architecture design.

3. **Integration with other solvers:** The ASCII format of the data and the scripting potential of this code can enable integration with trajectory optimization tools such as Genesis [59]. The evaluation of the propulsion system weight and sizing will inform structural requirements. This will then drive aerodynamic performance which can then affect propulsion requirements again. This iterative process can be accelerated through cross system analysis codes coupled together. There are individualized codes that can be merged to provide necessary inputs and outputs required by the solvers to assess various system level optimization studies.

4. **Mission evaluation:** The rapid ability to converge on potentially optimal design configurations enables engineers to rapidly assess suitability for various missions. As an example. the predicted mass flow rate can be used to estimate necessary fuel requirements which can provide an estimate on cost.

Several simplified models have been referenced by Paxson et al. as not being complete enough to fulfill the need to size and predict an engine's performance. These models on their own do not provide the ability to serve as a design tool. Two such papers cited are discuss the thermodynamic cycle analysis of pulse detonation engines [60] and results obtained through idealized thermodynamic calculations for RDREs using CEA [61]. Both of the analysis tools developed did not provide estimates on sizing or heat transfer. Furthermore, they use assumptions that do not take into account fundamental RDRE cycle losses. Given this fact, the predictions are over idealized.

Paxson then provides insight into an improved model by Kaemming et al. A reduced order approach on modeling RDREs implements time dependent sub-models with parameters tuned to match CFD results [62]. Although this model provides performance and sizing estimates, it was tuned using CFD results for air-breathing engine configurations. As such, the detonation physics will be different due to different chemical compositions in fuel mixing with air instead of pure oxidizer. The overview and theory that follows provides a more general model tuned for rocket based applications. The model is programmed in both Excel and MATLAB providing efficient means of leveraging automation and integration into other system level analysis codes.

The goal in creating this model was to enable the integration of a propulsion system model into other aspects of system and mission design. This is critical for early design phases as it is not feasible to undergo high fidelity simulation and experimental data driven performance optimization. These later design phases will use parametric variation and multi-dimensional, multi-phase, CFD simulations of entire RDREs rather than simplified models. The continuation of this project leverages the model's ability to provide reasonable estimates about RDRE design and performance with multi-dimensional variation to the input parameter space.

Various tuning parameters are built into the model and their values determined through using experimentally validated CFD simulations. For example, a variable in the governing equations or some scaling factor for a physical quantity can be chosen and tuned until the predicted value can come close to a measured result. The selection of these paraemters and the methodology of selecting the values will be discussed next.

3.1.2 Background - Anchoring the Q2D CFD Model

A paper by Paxson discusses the development and validation and comparison of Q2D CFD high fidelity numerical simulation and experimentally measured performance RDREs [63]. This 2D CFD code was developed in 2015 with the goal to validate a CFD model with experiment, investigate flow dynamics and optimize RDE design. Through model validation, the code could be a useful utility as a tool for performance optimization and diagnostics. Enabling researchers the ability to explore effects of mixing delays, heat transfer and deflagration on RDE performance is vital to save time and cost in early development. Furthermore, some of these measurements are not always obtainable in an experimental configuration. In summary, the 2D simulation code demonstrated high accuracy in performance prediction of thrust, flow rates, and pressure distributions.

The steady state solutions of this code capture the essential flow field structure in the reference frame of the detonation wave front. The detonation front is stationary and fresh mixture is flowing through the front at the detonation wave velocity. The model assumes the annular radius as much greater than the height and the working fluid to be a calorically perfect gas (CPG). Source terms are added to account for viscous effects and heat transfer between the walls and the working fluid. A simple one species reaction equation further reduces the computational complexity of this model. This finite rate reaction model states that the reaction rate is equal to the product of the amount of reactant and the rate constant K_0 [63].

Another important assumption made is the working fluid entering the combustion chamber is perfectly premixed. In reality, these fluids (in the rocket case, an oxidizer) or gases are injected separately, with potentially different pressures and result in imperfect mixing. Paxson mentions other important mechanisms to consider including flow reversal in the injectors taking place as the detonation wave passes over the injector face. When the pressure at the injector face decreases as the detonation front moves away, flow into the chamber resumes. However, due to the design of injection system, this resumption may not be simultaneous. In a finite gap between the annular walls, there can be viscous boundary layer affects that can cause transients and also lead to turbulence. For some instant in time, the pressure distribution over a set azimuthal location of the injector face is not constant. There can be purging periods where air is entering but fuel is not.

Paxson et al. provide a creative approach to setting a prescribed inlet reactant fraction to zero over various portions of the circumference of the engine in the simulation domain. Another physical phenomena captured by this model is the finite time it takes for the fuel and air to mix before reaction. The code was modified to set a user defined number of computational grid rows near the inlet to never react.

The inflow face is modeled with partially open boundary conditions, allowing to model the injection scheme into the computational fluid domain. An orifice separates the manifold providing the premixed fluid at a fixed total temperature and total pressure. The ratio of the flow area of this orifice over the annulus area of the RDE is defined as ϵ. Thus, if the pressure in the combustion chamber region is less than the manifold pressure upstream of the orifice, the propellant mixture can flow into the chamber. With ϵ and mass flow rate the properties of the flow are known at the inflow boundary. The model also handles backflow when pressure in the chamber exceeds the manifold pressure by tuning this orifice area to match experimental backflow data. Capturing these injector losses that can exist in real systems further improves the accuracey of these results.

Due to the coarseness of the simulation grid and the simplicity of the reaction

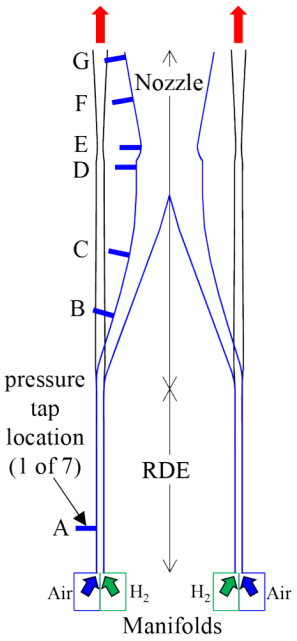

Figure 3.1: Experimental schematic showing a converging-diverging nozzle downstream of an RDE. [64].

mechanism, the authors reported high numerical diffusion which led to unrealistically high weave speeds in the deflagration zone. The K_0 parameter was tuned in these regions to adjust the rate of reaction. In the simulations performed, 8% of the incoming air and fuel mixture were set to undergo deflagration. They investigated other deflagration fractions. They cited for conditions from an experimental test case, adjusting the deflagration fraction from 8% to 17% predicted the thrust to fall by about 4% [63]. The model was tuned to best match experimental results under two conditions. The thrust, mass flow rate and pressure distributions were compared at various axial pressure tap locations along the axis of the RDE. A figure of the experimental rig is seen in Fig. 3.1.

The simplified and rapid converging CFD with tuned parameters and various lumped sub models showed favorable agreement with two experimental test cases [63]. The following plots from the work shows good alignment with pressure distributions along the axis of the RDE. The first plot highlights the purge scenario modeling realistic injection processes providing good agreement to experiment. The next plot in Fig. 3.2 shows the distribution of pressures from the experiment along location on the axis of the engine and the computed time averaged pressures with implementing the reaction delay model.

3.2 Model physics and derivations for computation

To simulate the performance and operation of the RDRE, the recently developed NASA RDRE blowdown code [37] [65] treats the engine as essentially infinite number of circumferentially arranged PDE tubes that fire sequentially one after the other. Each PDE is modeled using a time dependent Atkinson cycle. This cycle is an extension of the Humphrey cycle discussed in chapter 2 with inlet and outlet strokes, similar to those found in automobile internal combustion engines. Each PDE is treated as a lumped-parameter chamber with an ideal valve at the inlet and a throat at the exit. The inflow

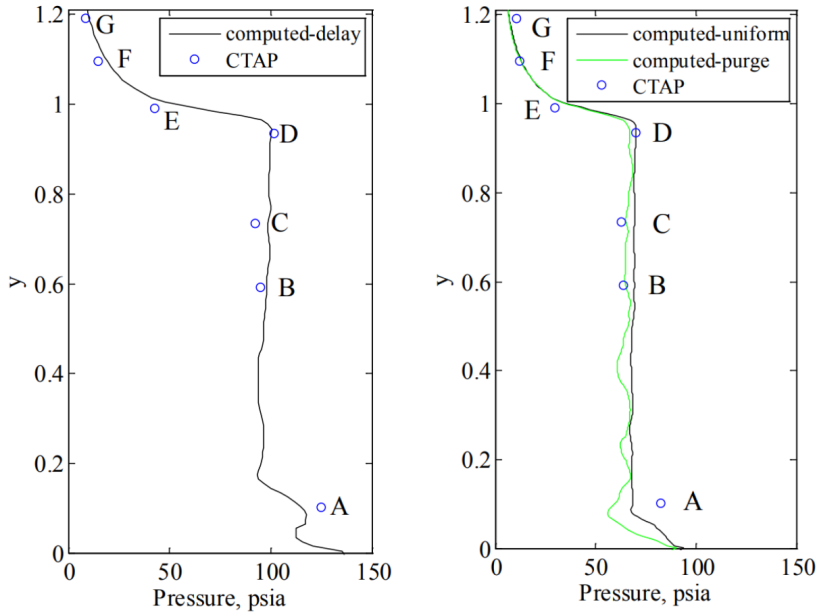

Figure 3.2: Computed time averaged and measured pressures implementing various sub-models. [63].

of fresh propellant has a finite Mach number that can be controlled through variance in the constriction area ratio at the throat before chamber exit. This is one such parameter that has been tuned to best replicate experimentally validated CFD results [37]. The RDRE analogous device is assumed to operate using calorically perfect gas (CPG). The ideal inlet valve moves instantaneously, closing when combustion begins and then opening fully when the refill phase begins. The refill occurs with no aerodynamic loss. The CPG gas properties are computed using CEA executable calls integrated into the code. CEA had to be installed and operational on the computer prior to utilizing the RDRE model code. CEA was also requested and obtained through the NASA software catalog.

Three stages represent the entirety of the cycle. First being instantaneous heat release at constant volume, followed by chamber blowdown (flow expansion) and then chamber refill. The cycle for each individual PDE tube can be seen in Fig. 3.3. This subsection contains detailed discussion on modeling these processes.

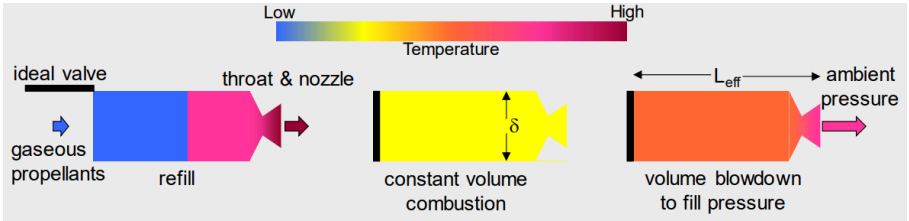

Figure 3.3: PDE tube chamber schematic during three phases used to model one complete cycle[66].

3.2.1 Constant Volume Combustion Phase

Governing equations and equations of state can be used to obtain the state of the gas at various points along this Atkinson cycle. The post constant volume combustion chamber temperature (Eqn. 3.1 can be obtained knowing the initial total temperature of the injection manifold and the heat released due to combustion of a known chemical composition as provided in Eqn. 3.2.

$$T_{c\_cv} = T_{tm} + \gamma(\gamma - 1)q_0 \; ; \; \frac{P_{c\_cv}}{P_{c\_final}} = \frac{T_{c\_cv}}{T_{tm}} \tag{3.1}$$

$$q_0 = \frac{h_f}{\gamma R_g \hat{T}^*(1 + o/f)} \tag{3.2}$$

Normalized variables are the default in this paper and are used accordingly here. Dimensional variables are denoted using the circumflex [37] over the variable. T_{tm} is the total temperature of the chamber inlet manifold. P_{c_final} is the final chamber pressure at the end of the refill phase. The first iteration of the solver assumes this variable to be equal to the inlet manifold pressure as P_{c_final} is not known. The density is found using the non-dimensional equation of state

$$P = \rho T \tag{3.3}$$

3.2.2 Engine Blowdown Phase

The blowdown phase then takes these results following the constant volume combustion computation as the initial conditions to the following set of ODEs.

$$\frac{d\rho_c}{d\tau} = -\rho_{th} v_{th} A_{th} \tag{3.4}$$

$$\frac{dP_c}{d\tau} = -\gamma(T_c \rho_{th} v_{th} A_{th} + \beta(\rho_{th} v_{th})^{0.8}(T_c - T_{wall})) \tag{3.5}$$

These are time dependent continuity and energy equations. The two equations are numerically integrated using a two-step Runge-Kutta method. The integration is solved when the chamber pressure matches the inlet manifold pressure.

Terms with the subscript th denote a notional throat at the exit of the chamber of each tube. The exit area ratio following this tube is set by the nozzle exit area ratio and the ambient pressure can also be specified by the user in this model. For a given exit area ratio, ambient pressure, the computed notional throat values determine the properties in the exit plane of the nozzle using the area-Mach number relations [67]. The right hand side of the energy loss equation (Eqn.3.5) is a wall heat transfer term that depends on a user specified wall temperature and with a geometric and fluid property parameter β. The throat area is normalized by a reference area and time is normalized by an acoustic transit time. This parameter is defined as the effective chamber length divided by the reference speed of sound. The effective length of the chamber is determined by a non-dimensional cycle time.

3.2.3 Engine Refill Phase

Next the refill phase of the cycle is computed. The fresh mixture is assumed to enter at a specified Mach number which is driven by the value of the notional throat area. This value was carefully tuned based on CFD results. This phase is modeled by the infill of new detonatable mixture, and the out flow of post detonative gas through the nozzle. The author notes that the fresh mixture and hot gases are separated by an assumed interface. The pressure across this interface is constant but with varying density. For this portion of the cycle, no heat transfer is assumed. The hot gases are therefore assumed to expand isentropically. For this portion, only one governing equation is used.

$$\frac{P}{\rho^{\gamma}} = \text{constant} \tag{3.6}$$

The governing equation for the refill phase is provided as follows.

$$\frac{dP_c}{d\tau} = \gamma(T_{tm}\rho_{in}v_{in} - T_c\rho_{th}v_{th}A_{th}) \tag{3.7}$$

Using an isentropic flow assumption and chamber pressure P_c, the inlet manifold plane properties are computed using:

$$\rho_{in}v_{in} = \begin{cases} \sqrt{\frac{2}{\gamma-1}}\frac{P_{tm}}{\sqrt{T_{tm}}}\left(\frac{P_c}{P_{tm}}\right)^{\frac{1}{\gamma}}\sqrt{1-\left(\frac{P_c}{P_{tm}}\right)^{\frac{\gamma-1}{\gamma}}} & \text{if } \frac{P_c}{P_{tm}} < \left(\frac{2}{\gamma+1}\right)^{\frac{\gamma}{\gamma-1}}, \\ \frac{P_{tm}}{\sqrt{T_{tm}}}\left(\frac{2\gamma}{\gamma+1}\right)^{\frac{\gamma+1}{2(\gamma-1)}} & \text{if } \frac{P_c}{P_{tm}} \geq \left(\frac{2}{\gamma+1}\right)^{\frac{\gamma}{\gamma-1}}. \end{cases} \tag{3.8}$$

The refill governing equation is integrated until mass is conserved.The total mass of the gas at the start of the fill portion and the mass that flows across the exit during the fill portion must match. To summarize, the code checks the relative error between the newly computed value of P_{c_final} and the value of P_{c_final} used in Eqn. 3.1. For instance, since the first iteration used a guess on P_{c_final} equaling P_{tm} to compute the post combustion temperature T_{c_cv}. The equation of state then defines the initial conditions of the gas for the blowdown phase. This time dependent blowdown process proceeds until the solution for pressure is equal to the inlet manifold pressure. At this point the refill phase commences and uses Eqn.3.7 to compute a new value on P_{c_final}. The process repeats by replacing the last guess on P_{c_final} with the newly computed P_{c_final} at the end of the last iteration back into Eqn. 3.1. Fig. 3.4 shows the calculated chamber pressure requiring 4 cycles to reach limit cycle behavior [37]. This is the repeatable steady state operation that provides a periodic solution, meaning, the conditions at one end of one cycle match the conditions at the end of the next cycle.

When the solver converges, the cycle averaged performance parameters are calculated. The following equations are used to compute the mass flow rate and the specific thrust respectively.

$$\omega = \frac{P_{c\_final}}{T_{tm}\tau_{cy}} \tag{3.9}$$

$$F_{sp} = \frac{\int_0^{\tau_{cy}}(\frac{P_e - P_0}{\gamma} + \rho_e v_e^2)d\tau}{\int_0^{\tau_{cy}}(\rho_e v_e)d\tau} \tag{3.10}$$

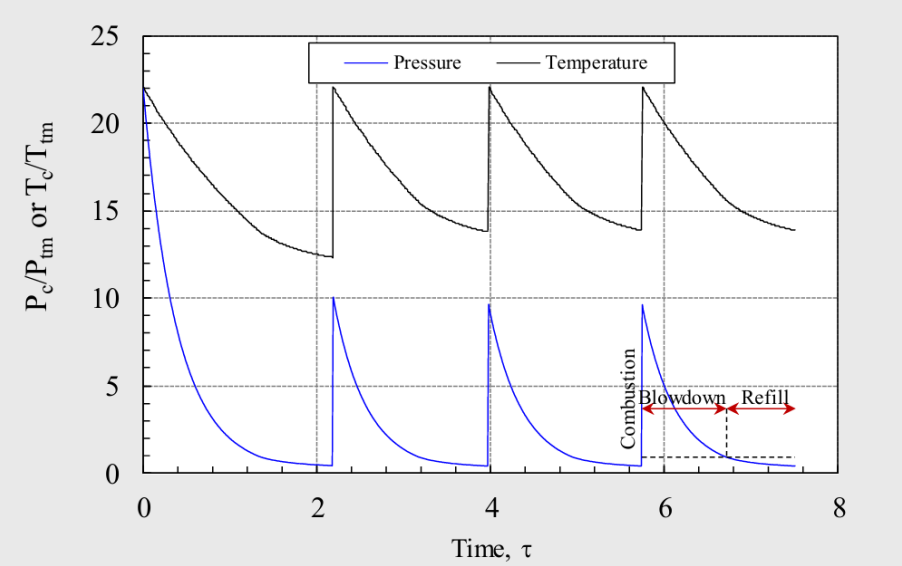

Figure 3.4: Model convergence to a limit cycle for pressure and temperature.[37].

3.2.4 Experimentally Validated CFD Anchoring of Notional Throat Area Parameter

The notional throat used in the model is a fluidic throat rather than a physical throat, but aims to capture effects as such. The next few paragraphs aim to provide insight behind the studies done leading up to how this value is used and how it was tuned. Paxson and Perkins reported from idealized Q2D CFD simulations that the detonation gas products reach sonic velocity downstream of the detonation but upstream of (before) the detonation exit plane. The location of the notional fluidic throat meant to replicate this sonic condition determines the characteristic length. The value of this notional throat determines the fill Mach number. The value was tuned to match fill Mach numbers observed in their Q2D CFD simulations. This value was not altered in the work that will be presented through implementation of the model in this design study. Beyond providing a good estimate on fill Mach number, these values also seem to have implications on detonation stability and performance.

Performance is tightly coupled to inlet design and minimal restriction between the supply manifold and the annulus is beneficial. An ideal inlet prevents backflow when the pressure at the inlet face is high in regions behind the detonation wave. However, this comes with the trade and careful balance of minimizing aerodynamic loss during inflow and preventing backflow. Preventing backflow is important it prevents pressure drops in the manifold and from a reliability standpoint, can protect injection systems and other critical elements upstream of the inlet manifold. Backflow can lead to inconsistent injection and thus potentially ruin the continuous operation of an RDE. Constriction at the throat of the chamber has been reported to increase performance. The exhaust throat reduced the fill Mach number and increases the pre-detonation pressure, just upstream of the detonation wave reducing aerodynamic losses at the inlet [68]. This points to improved performance over similar chambers with no exit throat. However, as with almost all engineering decisions, it comes with a trade off. Reducing the throat area means that the number of reflected shock waves that travel from the throat back to the inlet can potentially disrupt the inlet process, engine operation and lead to instability.

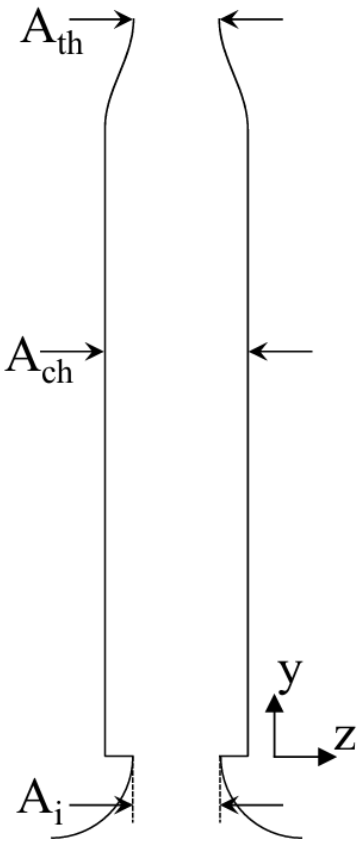

Figure 3.5: Axial profile of RDE [68].

Results from previous work done by Paxson [68] in studying the impact of an exhaust throat on semi-idealized RDE led to the question of whether an instability found growing in time leading to a detonation failure was a physical solution or a result of the numerical method used. The affect was verified to be a physical occurrence rather than a numerical artifact. The work done by Paxson and Schwer in [68] aimed to investigate the effects of these parameters on pressure gain performance and its effects on detonation wave stability using numerical simulations.

Two independently verified CFD codes were used in this study. As displayed in Fig. 3.5, the throat area denoted as A_{th} throat areas were tested to investigate the effect of throat constriction on performance and detonation stability. The performance for these simulations was benchmarked by an ideal exhaust Equivalent Available Pressure (EAP_i). Paxson and Schwer define this as essentially the pressure required to produce the specific thrust provided by the RDE. A plot showing a maximum value occurring in the range of 0.72 to 0.76 the area ratio of the throat over the channel area is seen in Fig. 3.6

The two CFD codes showed that the instability that arises from constricted throats was thermo-acoustic in nature. Pressure and heat fluctuations were deemed to be coupled in a complex manner. Given the complex flow phenomena, boundary layer interactions, reflected shockwaves, differing time-scales for heat transfer and pressure interaction phenomena. It is critical to understand when and how these behaviors arise, and what can be done to mitigate them. Accurately modeling these interactions and behaviors is a complex undertaking. Furthermore, heat release from the combustion process and pressure oscillations from reflected shock waves from the physical throat can reinforce each other

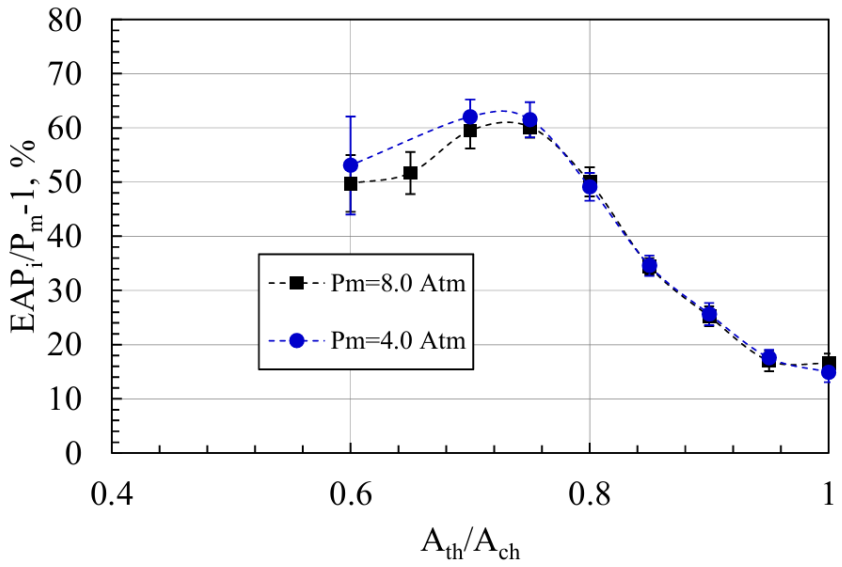

Figure 3.6: EAP_i pressure gain as a function of throat to channel area ratio at different manifold pressures [68].

and collapse the stability of the detonation wave as it revolves around the annulus. The authors reported that the exact mechanism of the reinforcement of these pressure and heat release fluctuations was unknown. However, it was apparent from the simulations that the mechanism involves perturbations in the detonation height due to interactions between the inlet and waves reflected upstream from the exit throat [68]. This can visually be seen in Fig.3.7 where time is represented by the number of revolutions the detonation wave has passed through the 2D periodic boundary. Note the injection boundary changing in time and the variance in the height of the detonation front. The simulation performed here was for an idealized inlet where the inlet area equaled the chamber area (no restriction at the inlet).

3.2.5 Modeling Injection and Inlet Conditions

To further investigate instability and performance affects due to other parameters, Paxson and Schwer investigated the size of the inlet restriction, inlet manifold pressure, axial length, and reactant equivalence ratio. They reported the inlet restriction having the largest effect on stabilization. While inlet restriction leads to unavoidable aerodynamic loss, the consequence of that loss seems to be compensated by the stabilization effect of the constriction. Inlet restriction is a real laboratory approach of achieving non linear valving where flow wants to move forward but not backwards against the grain. These non-mechanically actuated injectors are also known as fluidic-diodes. A schematic from Teasley et al [12] can be seen in Fig. 3.8. Different fluidic diode schemes informed by additive manufacturing (AM) were considered as well. These can be seen in Fig. 3.9. This review from NASA outlines numerous desirable attributes for successful injector design. An interesting lesson learned from this paper is that some of the better design features are only possible through additive manufacturing [12]. Additive manufacturing provides the engineer the ability to optimize fluidic geometries and manufacture the complex geometries these designs provide. The paper also covers important how injectors influence mixing efficiency, operational stability, performance, manufacturability

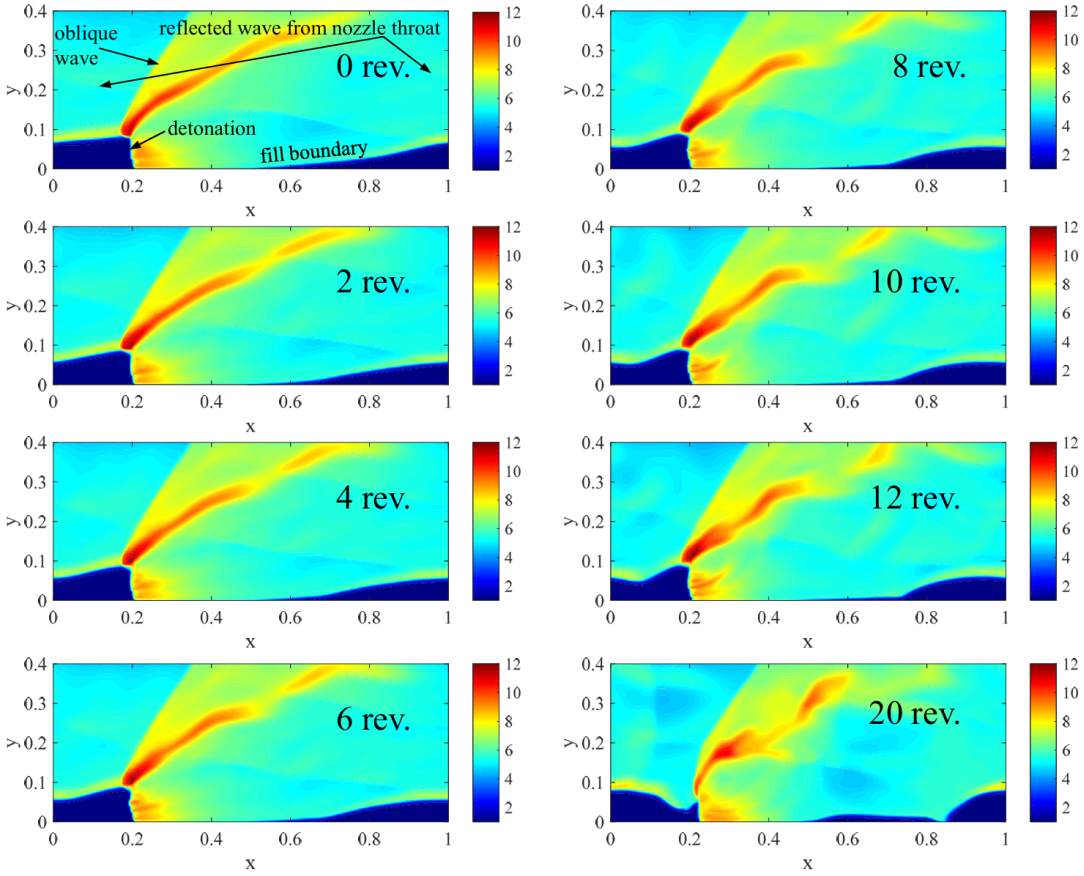

Figure 3.7: Non-dimensional temperature contrours visually showing the instability breaking down the detonation wave after 20 revolutions around the simulated annulus for a throat area to channel area ratio of 0.85 [68].

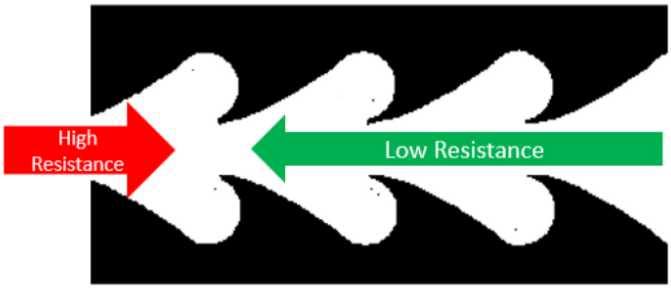

Figure 3.8: Fluidic diode showing high resistance to flow in one direction, and low resistance to flow the other direction [12].

and more. This leads back to the discussion from Paxson and Schwer's analysis on inlet restriction. With an understanding of these fluidic diodes and how representing these restrictions mimics the increased backflow resistance, it makes sense that this restriction reduces the ability for reflected waves to propagate energy upstream the injector. This improves stabilization inside the chamber at the cost of increased aerodynamic loss. The author reports the gain outweighs the loss here. The aerodynamic loss is modeled as a total pressure loss that increases with decreasing inlet area to chamber area ratio.

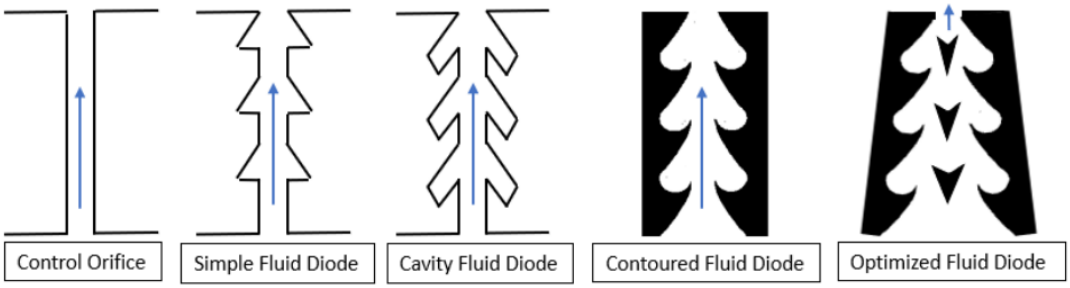

Figure 3.9: Different AM fluidic diodes and their injector orifice and control case [12].

Other design and operational parameters such as axial length, inlet manifold pressure and reactant equivalence ratio provided more insights. It was determined that the axial length did not have an effect on stability. In fact, the paper mentions that as length increases, more entropy is generated as the oblique wave and the shear zone behind it are longer in length as well. Paxson and Schwer report the potential reason behind improvement in EAP_i with shorter lengths may be a result of this. It was reported that once the exit flow is choked, CFD solutions become invariant with changing manifold pressures. Given instability is caused in part due to heat release fluctuations, the authors studied the effect of different equivalence ratios. It was found that reducing the equivalence ratio reduces instability.

In some configurations, the authors reported with reduced instability, the lower equivalence ratio also allowed for a smaller exit throat which in turn improves performance. It is interesting to note from the conclusion of the paper at the time that, although these instabilities were not yet observed in experimental RDEs, they predicted that the instabilities may appear as RDE performance begins to approach the performance of semi-idealized simulations. Experimental work done by Bennewitz et. al out of AFRL in 2021 further verified this behavior. The data showed increasing engine performance with increasing throat constriction. The maximal increase was cited to be 27% for both the I_sp and thrust. The also measured that there was nearly equal performance in the shorter length chambers as the longer length counterparts. The experimental data also proved that with counter propagating wave sets become more prevalent with increasing constriction, thereby reducing the wave speed and increasing unsteadiness. One of the conclusions of this work further solidified the predictions made by Paxson's CFD code. The authors suggested that injection physics drives chamber wave dynamics, and the interaction between the throat and the injector influences this counter-propagation detected in experiment [69].

This model's CPG assumption limits the use to one value for γ. In a real gas, γ would vary significantly during the denotation cycle. To obtain a reasonable estimate on γ, the model executes the CEA code during its computational process to get a value for the ideal specific thrust of the ideal Atkinson cycle. Corrections on γ are made iteratively until the value computed by Eqn.3.11 matches the result of the CEA code. The required inputs are inlet manifold pressure and temperature, the ambient pressure, and the fuel and oxidizer type and ratio [37].

$$F_{spi} = \frac{-\int_{P_{c\_cv}}^{P_{c\_refill}} v_e dp_c + v_{e\_refill} P_{c\_refill}}{\rho_{c\_cv}} \tag{3.11}$$

Paxson outlines the results of an adiabatic test ($\beta = 0$) of the sea level static specific impulse over a range of manifold pressures. The engine modeled for this study had RP-1 as the fuel and O2 as oxidizer. The equivalence ratio of the mixture was set to a value of $\phi = 1.3$. To model a rich mixture with single gas models, the effective fuel heating value is adjusted. The following relationship determines the effective heating value.

$$h_{f\_eff} = (H_m - H_p)(1 + o/f) \tag{3.12}$$

H_m is the mixture enthalpy found using the initial mixture pressure and temperature executing an *hp* problem in CEA. The *hp* problem in CEA computes the equilibrium composition and state of the fuel-oxidizer mixture at a fixed enthalpy and pressure. CEA is then run in *tp* mode, which computes the chemical equilibrium composition and state of the same mixture fixed at an initial temperature and pressure. The output from this step provides a value for the product enthalpy H_p. The oxidizer fuel ratio is also determined by the equivalence ratio that is provided as a user input. The model provides the ability to model rich fuel mixtures more accurately as real engines can use rich fuel mixtures to provide cooling Paxson states that the reference state for the calculations is: $\hat{P}^* = 14.7$ psia, $\hat{\rho}^* = 0.082$ lbm/ft^3, $\hat{T}^* = 540$ R [37]. The following equation is then used to compute the dimensional specific impulse from the non-dimensional specific thrust.

$$I_{sp} = \frac{\hat{a}^* F_{sp}}{g_c} \tag{3.13}$$

The reference speed of sound used in this equation is determined from the reference parameters provided above. The range for the speed of sound at the injection site is between 984 and 991 ft/s [37]. The author notes that this range is due to the small changes in γ when the manifold pressure changes.

3.2.6 Performance Prediction and Discussion

Paxson et al. provide a succinct plot comparing the model to the ideal Atkinson cycle, and ideal conventional rocket (constant pressure) and the Q2D CFD developed that was validated with experimental data. It is interesting to note how comparable the RDRE model is to predicting specific impulse of a $\phi = 1.3$ RP-1/GOX mixture at sea level static conditions (ambient pressure = 14.7 psia). Furthermore, the predicted performance of the RDRE at these operating conditions yield about a 8% increase in I_{sp} compared to an idealized conventional rocket engine computed again from CEA with a CPG assumption. The x-axis provides varying dimensional manifold pressures in units of psia. This model provides reasonable estimation of RDRE performance and thus was selected as the primary tool for this design trade space study to understand sizing and performance due to design parameter coupling. As noted by Paxson et al. an RDRE can provide similar performance of a comparable rocket engine at reduced manifold pressures. In fact, it is reported that the model in its current state actually underestimates idealized RDRE performance. This implies that optimized designs may have even higher performance than predicted by this model. Reduced manifold pressures will enable lower structural and turbo-machinery requirements. This could have implications to overall vehicle architecture design and other subsystem and element level requirements may be simplified due to the lower operating pressures. The increased heat release presents it's own challenge and ultimately will require engine designers to ensure cooling capabilities

meet requirements set by the extreme conditions present inside the combustion chamber.

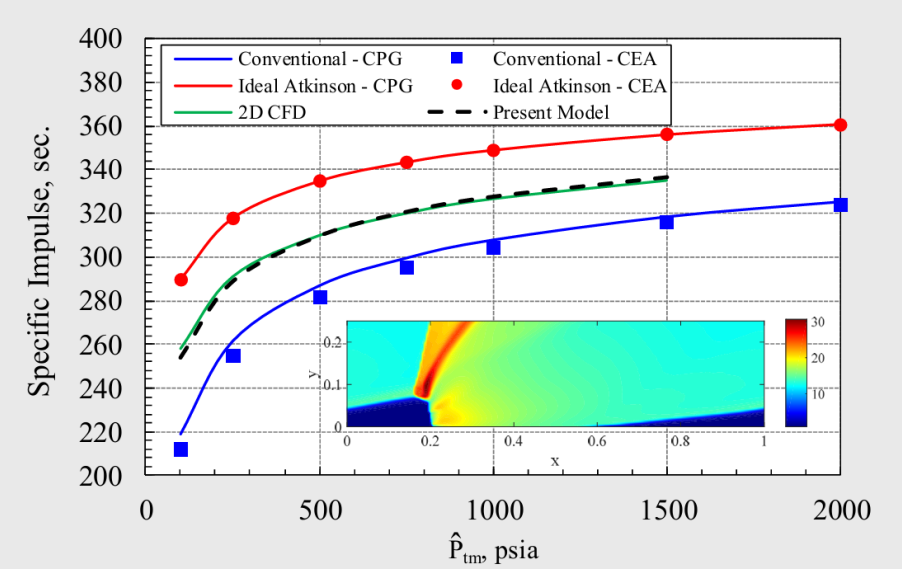

Figure 3.10: RDRE Specific impulse predicted by various methods by Paxson et al. [37].

3.2.7 Engine Sizing, Flow rates, and Heat Transfer

Paxson et al. provide insight into how they take this notional chamber with analogous dimensions and translate it to a physical size and thrust estimation. The sizing also provides necessary parameters to predict heat transfer to the cooled walls. Two parameters are used to provide heat transfer estimates, the mean diameter D_m and annular gap δ are supplied as inputs. The time it takes for one cycle with the three defined phases to complete is matched to the time it takes for a detonation to travel around the annulus. The detonation wave speed is given in Eqn. 3.14 [37].

$$u_{det} = \sqrt{(\gamma+1)(\gamma-1)q_0 + 1 + \sqrt{((\gamma+1)(\gamma-1)q_0+1)^2 - 1}} \tag{3.14}$$

It can be seen the velocity is determined by q_0 and γ where the method to obtain both values has been outlined earlier. These two variables are mostly driven through selection of the fuel and oxidizer, and operating conditions of the working fluid. From the definition of non-dimensional time, the effective chamber length can be obtained by [37]:

$$L_{eff} = \frac{\pi D_m}{\tau_{cyc} u_{det}} \tag{3.15}$$

The authors report the effective length value is not used in the analysis within the code, but to rather it provides a sanity check as it should be on the same order as the sonic choke point seen in validated CFD solutions. The dimensionless mass flow rate is provided in Eqn. 3.16.

$$\hat{\omega} = \omega \hat{\rho}^* \hat{a}^* \pi \delta D_m \tag{3.16}$$

The heat transfer coefficient in Eqn. 3.5 is provided in Eqn. 3.17. In the model, the Prandtl number can be changed but is set as 0.7 by default. L_{act} is the actual length

of the RDE computed using the hydraulic diameter of the engine. This will be discussed later. $\bar{\mu}$ is the average viscosity of the fluid.

$$\beta = 0.023\alpha^{\frac{4}{3}}\frac{L_{act}}{\delta^{2/3}}Pr^{-0.67}Re^{*-0.2}, \quad \text{where } Re^* = \frac{\rho^* a^* \delta}{\bar{\mu}} \tag{3.17}$$

The free parameter α is tuned by matching CFD results that were validated with experimental results. Paxson and Perkins provide methodology to how and why this parameter was tuned. To summarize from their work, parameters in the model were tuned until measured and computed mass flow rates matched using specified manifold pressures and temperatures for a stoichiometric hydrogen air experimental engine. With this tuning done, the model was able to predict the thrust of the experimental engine to within 15% while the code matched experimental inlet area within 8%. Furthermore, this model in its current state models the injected fluid as a CPG. Further work is discussed to implement multi-phase fluid sub-models to capture either liquid or supercritical fluids that will inevitably be used in RDREs [63]. When taking two test points of an experimental engine where the CFD predicted a 50% drop in total pressure across the inlet and setting this reduced value as the input manifold pressure, the model predicted the mass flow rate of the experiment to within 5%. They then further tuned α to match the CFD predicted value of 17% of the energy being absorbed by the cold walls in the experiment [37]. A brief overview on a model predicted 190,000 lbf class RDRE using RP-1 as fuel was presented in Chapter 2. Two geometrical configurations achieving comparable thrust were used to demonstrate model utility in potential design optimization.

3.3 Gas Generator and Turbopump Model

3.3.1 Discussion

In a rocket engine, fuel and oxidizer are transported from their storage tanks and into the injection manifold at specified pressure and mass flow rate requirements. Minimizing losses during this process is crucial for engine performance optimization. The turbine converts thermal energy generated by a smaller combustion chamber, called a gas generator, and converts it to useful mechanical work. The mechanical work can then be transferred to oxidizer and fuel pumps. Turbopump driven propellant feed systems enable high operating pressures, providing increased engine performance and efficiency compared to pressure fed or gravity fed systems, especially for high thrust engines [45].

Turbopump feed systems consist of several elements. The propellant pumps, turbine(s) to drive these pumps, a power source for the turbines, and additional elements such as gears, lubrication systems, accessory drives, propellant inlet and discharge ducts, and turbopump mounts [45]. There are several common methods to provide power to these turbines. Three of focus are the gas-generator cycle, expander cycle, and staged combustion cycle. The gas generator cycle is either bipropellant or monopropellant. The bipropellant takes a small amount of fuel and oxidizer and combusts it before exhausting it to drive the turbine. The turbine flow is then dumped over board. This is how the gas-generator turbo-pump feed system is modeled in the Paxson and Perkins model. The gas generator is conventionally combusting a small fraction of the propellants at a very fuel rich mixture. This enables the gas generator to operate at lower temperatures and prevent damage to the turbine. The exhaust of the gas generator does not generate thrust

as the engine is modeled as an open cycle gas generator. Huzel and Huang [45] state the gas-generator cycle has a turbine flow path in parallel with the thrust chamber flow path. Gas generator cycle engines have the improved benefits of simple operation and reduced development cost with the drawback of lower performance compared to turbine flow paths that are in series with the chamber.

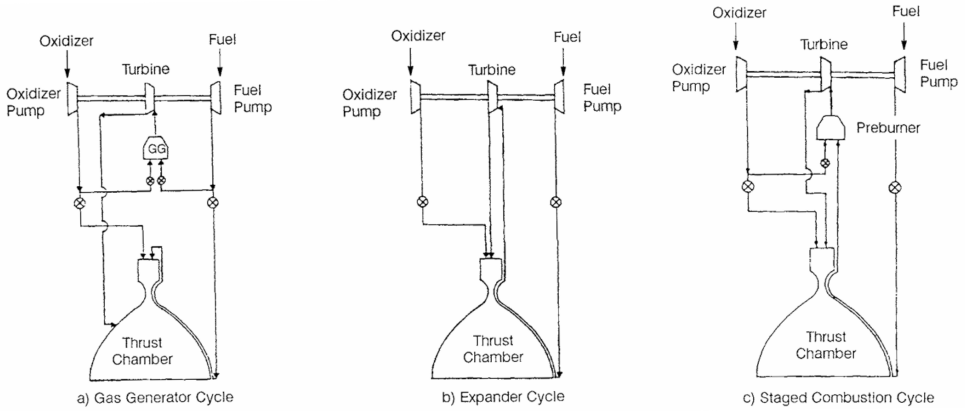

Figure 3.11: Basic cycles for pump fed liquid-propellant engines [45].

The energy conversion processes may be modeled using isentropic relations, with additional efficiency parameters. Values for these efficiency parameters would be found using high fidelity simulation or empirical data from testing allowing for a simplified but accurate method of modeling known component losses and studying the effect on the system as a whole. Furthermore, technology forecasting trends can be used to predict performance gains the particular element may have on a system. This is useful for projecting improvements and studying impacts on future mission planning and design [70]. Such improvements may for example be quantified in terms of reduced fuel consumption and thus total weight of a proposed system.

Paxson and Perkins provide further utility to this RDRE performance and sizing tool by enabling the simplified modeling of cooling jackets within the combustion chamber as well adding a gas generator driven turbo-pump. The turbopump sub-model will be discussed in this section. The capability of the code to provide estimates on necessary performance requirements may assist in engine design and optimization. Furthermore, these system level data can inform individual element design. For example the blade geometries in a pump may be optimized to compress the fluid more efficiently. The number of blades, their shape, angle, curvature and material selection may be parameters varied in an optimization study. The turbine designer needs to achieve maximum efficiency within constraints imposed, and the trade off between flow and available energy needs to be optimized [45]. The scope of work in this report will not go into this design, but is planned as future work. Nevertheless, the turbopump component may be modeled using assumption on these efficiency parameters.

3.3.2 Turbine Model

The gas generator combusts a fuel rich mixture of fuel and oxidizer providing energetic flow to power a turbine. The total enthalpy of the hot gas provided by the gas generator must be converted into useful mechanical work in the form of a turbine, shaft,

and pump assembly. The pump-feed system must consume this energy and mechanically drive propellant mass into the combustion chamber. The amount of power required per unit mass to operate the turbine and pump may be determined through the following method.

A subroutine MATLAB file exists in the NASA tool that computes turbopump parameters. The function takes in two arguments, the options defined in the main run file, and the global parameters that are needed for the calculations. Both arguments are MATLAB structures. The function outputs the specific power input required for the pump, and the specific power output of the turbine, both in BTU/lbm. The required pump power in units of horsepower is also computed. Lastly, the required mass flow rate $\dot{\omega}_{\text{gg}}$ to power the gas generator is provided. These values are stored to a dataset to later be processed. This helps provide a more accurate estimate on the fuel and oxidizer consumption that is lost to power the turbine. Values and parameters used here will reflect the notation style used in the code.

Efficiency values η_p and η_t are constant values assigned by the user for the pump and turbine component respectively. The total power per unit mass of the turbine and pump driven by the working gas downstream of the gas generator are computed. The working fluid is assumed to be a CPG allowing for use of isentropic relations. The turbopump is modeled under the assumption the engine operates at steady state with constant pressures and mass flow rates.

The post combustion gas generator properties such as γ_{gg}, the specific gas constant R_{gg}, temperature T_{gg} and the oxidizer fuel ratio OF_{gg} are computed using a built in CEA function call described earlier. The necessary user inputs are an equivalence ratio, and operating pressure inside the gas generator, P_{gg}. This allows the computation for the total available energy contained by the gas before the turbine. This can be defined as the enthalpy drop per unit weight of working fluid in the turbine.

$$\Delta h = c_p \cdot (T_{gg} - T_e) \tag{3.18}$$

The specific heat at constant pressure c_p for the working fluid can be defined by properties computed from CEA:

$$c_p = \frac{R_{gg} \cdot \gamma_{gg}}{\gamma_{gg} - 1} \tag{3.19}$$

A value can be supplied as a user input defining the pressure ratio of the turbine (PR_t) defined as

$$\text{PR}_t = \frac{P_{gg}}{P_e} \tag{3.20}$$

This value in the code is set to 3 by default. Inputting higher values for this parameter will model more a efficient turbine enabling the analysis of its effect on engine performance. The isentropic flow relations can then be used to solve for T_e [45] and the resulting drop in enthalpy drop can be written as:

$$\Delta h = c_p \cdot T_{gg} \left[1 - \left(\frac{P_e}{P_{gg}} \right)^{\frac{\gamma_{gg}-1}{\gamma_{gg}}} \right] \tag{3.21}$$

The actual specific power produced by the turbine will be scaled by the value for η_t. Plugging in for c_p, and a user defined pressure drop across the turbine PR_t yields an expression:

$$\dot{e}_t = \eta_t \left(\frac{R_{\mathrm{gg}} T_{\mathrm{gg}} \gamma_{\mathrm{gg}}}{\gamma_{\mathrm{gg}} - 1} \right) \left(1 - \mathrm{PR}_t^{\frac{1-\gamma_{\mathrm{gg}}}{\gamma_{\mathrm{gg}}}} \right) \tag{3.22}$$

Where $\dot{(e)}_t$ is used in the code to denote the specific power the turbine delivers per unit mass of flow.

3.3.3 Pump Model

The pump adds energy to the fluid preferably in the form of higher discharge pressure. To obtain this higher discharge pressure, the specific power required by the pump can be computed knowing the mass flow rate of each propellant with the increase in pressure that must be obtained from the storage tank to the inlet manifold. The operating pressure at the inlet manifold for the engine is a user defined value for P_{man}. However, since some fuel and oxidizer must be redirected to the gas generator, this amount of mass flow rate must be taken into account. The specific pump power can then be computed for both the power input into the annular chamber as well as the power input to feed the gas generator. A useful engineering term defined by Huzel as the pump developed head (DH) is the difference between pump-discharge total head and pump suction head, representing the energy added per pound of pumped fluid and expressed as a change in enthalpy with units of ft-lb/lb, (typically units of ft). The DH required to obtain an inlet manifold pressure can be written as [65]:

$$p_{sp\_fuel} = 144 \left(\frac{P_{fuel\_in} - P_{tank}}{\rho_{fuel\_in}(1 + o_f)} \right) \tag{3.23}$$

The same is applied for the oxidizer.

$$p_{sp\_oxid} = 144 \left(\frac{P_{man} - P_{tank}}{\rho_{oxid\_in}(1 + o_f)} \right) \tag{3.24}$$

The tank pressure can also be set as the user and is at a default value of 14.7 psi in the code. If the RDRE is instead driven by a pressure fed system where the tank pressure would be set to a specified pressure and the turbopump sub-model could be deactivated.

The flow is assumed to be incompressible and the density of each propellant is found using fluid property lookup tables for common fuels provided in the program. The temperature of both propellants leaving the storage tanks are set as inputs. The methodology to obtain fluid properties for a given temperature will be discussed in more detail as it also pertains to the cooling system modeling in the next section of this chapter.

The pump developed head or energy added per pound of pumped fuel to bring the fuel to the gas generator operating pressure is provided as:

$$p_{sp\_fuel\_gg} = 144 \left(\frac{P_{fuel\_in} - P_{tank}}{\rho_{fuel\_in}(1 + o_{f\_gg})} \right) \tag{3.25}$$

and for the oxidizer as:

$$p_{sp\_oxid\_gg} = 144 \left(\frac{P_{man} - P_{tank}}{\rho_{oxid\_in}(1 + o_{f\_gg})} \right) \tag{3.26}$$

The actual specific power required for both the main engine and the gas generator can be found leveraging η_p provided by the user. The default value used in the code is 0.9. The equation for the specific power required to the drive propellant into the combustion chamber only is written as:

$$\dot{e}_{main} = \frac{p_{sp\_fuel} + p_{sp\_oxid}}{\eta_p} \tag{3.27}$$

The same is applied to delineate how much specific power the pump must achieve to sustain the gas generator:

$$\dot{e}_{gg} = \frac{p_{sp\_fuel\_gg} + p_{sp\_oxid\_gg}}{\eta_p} \tag{3.28}$$

The turbine needs to satisfy the power requirements of the engine and gas generator. As such, mass flow rate of the gas generator will be proportional to the power required to provide the flow rate $\hat{\omega}$ into the main combustion chamber. The code is able to call this value as part of a field within the data structure called as an argument to the turbopump parameters function in the code. Notation wise, the derivation in [37] used $\hat{\omega}$, and the code uses $\dot{\omega}_1$. The ratio of flow rates provided below:

$$\frac{\dot{\omega}_{gg}}{\dot{\omega}_{main}} = \frac{\dot{e}_{main}}{\dot{e}_t - \dot{e}_{gg}} \tag{3.29}$$

Where the total flow rate required by the propulsion system not including losses by the cooling system would be:

$$\dot{\omega} = \dot{\omega}_{gg} + \dot{\omega}_{main} \tag{3.30}$$

3.3.4 Impact on Design

The value in the denominator of Eqn. 3.29 is the specific power available after some has been drawn away to sustain the gas generator. The specific power available corresponds to the power necessary to drive the main engine. For example, a desired thrust will drive the main engine propellant consumption and associated power requirement. Improving the turbine efficiency through optimal component design could be an example of studying element level optimization effects on system performance. The available power quantity would increase, resulting in a smaller ratio and ultimately decreasing the flow rate requirements into the gas generator. Given the ability to go into the code and add additional condition statements, such as checking to see if the user wants to model a staged combustion cycle engine, the models can be tuned to represent the improvements of such a system on overall fuel efficiency. This highlights the modularity and flexibility this code provides in engineering analysis and design studies.

Paxson et al. provided a performance estimation comparison highlighting the effects of operating an RDRE with an open cycle gas generator under varying manifold pressures. The plot provided in Fig.3.12 highlights the ideal Atkinson-CPG model, the present code being discussed with no heat loss modeled, with heat loss modeled as seen in green, and finally with both heat loss and the gas generator operational. The parameters used are provided in the following table.

The specific impulse trends comparatively with the heat transfer model highlighted

Table 3.1: Default settings for pump feed system used in code.

Parameter	Value
Single stage turbine pressure ratio (PR_t)	3.0
Turbine efficiency (η_t)	0.6
Pump efficiency (η_p)	0.9
Tank Pressure (P_{tank})	14.70 psi

by the green line until about 500 psi. After that, the rate of efficiency improvement begins to trail off with increasing manifold pressure requirements. This is expected as the power demand on the pump system will scale the flow rate consumed by the gas generator. It would be interesting to implement a sub-model for a staged combustion engine and study performance gains at these higher pressure ranges. This is also planned future work.

The curve nearly flattens out after about 1000 psia signifying to the designer that efficiency performance is not longer improving with increasing pump requirements. In fact, this does not capture the non propulsive system trades of further increasing pump power such as the size and weight of all pump and turbine elements.

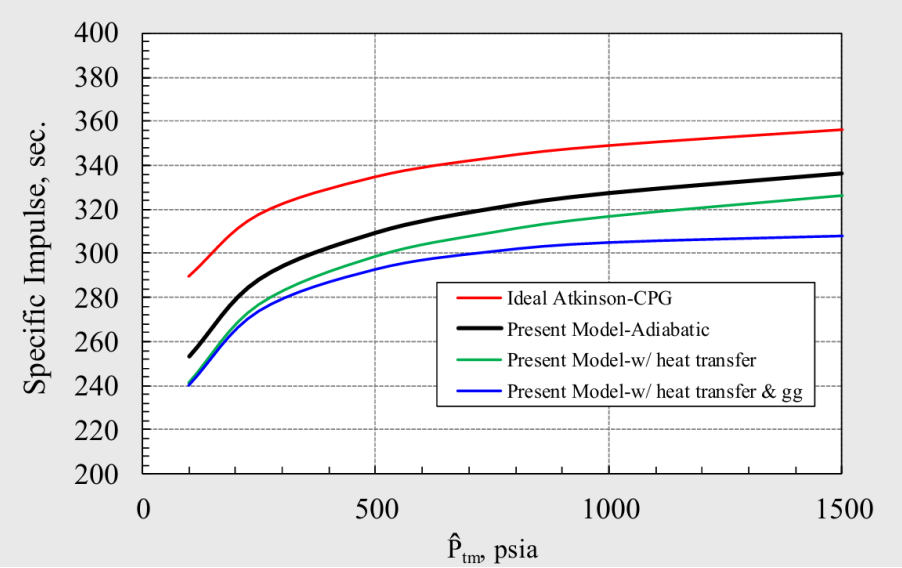

Figure 3.12: RDRE specific impulse as a function of inlet manifold pressure for an RP-1/GOX engine [37].

3.4 Additional Components - Cooling Sub-model and heat transfer

As the code solves the governing equations, it has the necessary parameters to compute the total heat load on the walls. The mass flow rate of the fuel is also known. The authors implement curve fitting techniques to tabulated liquid properties of common fuels in the code. These fuels include RP-1, H2, and CH4 (methane). Other fuels can be added manually by the user. The percent of the chemical energy lost to the wall is also computed knowing the mass averaged exhaust total temperature and the adiabatic value that compares with the mass averaged exhaust total temperature [65]. This percent

chemical energy lost to the chamber walls is used as a proxy to compute the heat load the cooling system needs to manage. Mass flow rate of the fuel is determined using the known oxidizer fuel ratio and the total dimensional mass flow rate.

$$\hat{\omega}_{fuel} = \frac{\hat{\omega}_{total}}{1 + O/F} \tag{3.31}$$

The total heat load to the walls is then computed using the dimensional parameters for fuel mass flow rate and heat of reaction of the mixture as computed by CEA run to find γ.

$$\dot{\hat{Q}}_{total} = \hat{\omega}_{fuel} h_f (\%\text{ chem energy to walls})/100 \tag{3.32}$$

Cooling passages with fuel flowing through them are also modeled in this code. Fig. 2.14 represents an axial view of the cross section of a chamber and its cooling passages along the inner and outer wall. The model assumes that 75% of the wetted perimeter of the channel is active for heat transfer and the passages are rectangular in cross section and extend along the length of the engine,(L_{act}. This value can be adjusted based on actual data on cooling capabilities of the engine cooling system. A United States Patent by Vlahinos et al. denotes a novel structural gyroid lattice infill that optimizes cooling and heat transfer capabilities of additively manufactured structures by increasing surface area for heat transfer to take place without increasing the mass or volume of the structure [71].

The cooling submodel will not used in the design of experiments study in Chapter 5 as it involves iterative testing of different channel sizing parameters to converge on configurations where the temperature in the cooling chambers does not exceed the threshold for thermal coking while providing minimized losses in engine efficiency.

The cooling model is described in detail in [37] and the user manual [65] provides detail to the equations and parameters used. The following is a short summary of what is described in both references. The cooling sub-model takes an input guess on the aspect ratio and passage width of the rectangle seen in Fig.2.14 This enables the calculation of the number of passages and thus the heat load each passage needs to absorb for a given wall temperature also set by the user. The fuel flow rate through each channel is then computed. The coolant properties are computed based on a curve fit and algorithm outlined in [65]. Data on various fluid properties as a function of temperature for common fuels/coolants are stored in the model codebase. The common fuels recorded are CH4, RP-2 and H2. When the cooling sub-model needs the state of the fluid in the passage, the temperature value is plugged into a curve fit function for that data. The data is is referenced to provide estimates on average fluid properties given the computed average temperature.

$$\text{fluid property value} = \frac{a_0 + a_1 T + a_2 T^2 + a_3 T^3}{1 + b_1 T + b_2 T^2 + b_3 T^3} \tag{3.33}$$

This expression is utilized within a subroutine file that is called to obtain fluid properties at given temperatures. The function takes in several arguments, of which one is a string denoting the fluid property to be computed and returned to the calculations being performed by the cooling submodel. These properties include c_p, dynamic viscosity μ, heat transfer coefficient k and fluid density rho. Polynomial coefficients are defined in a matrix for each coolant. No phase change occurs inside the cooling channels as the property relationships are for a supercritical fluids.

Obtaining fluid properties at a specified temperature, along with known geometric parameters and operating conditions enable the computation of the average velocity of the coolant. Knowing the average velocity is crucial for the design of a cooling system. Velocity is found using the fuel flow rate, passage cross section geometry, and average fuel density determined by the curve fitting described earlier.

Velocity, hydraulic diameter, density and viscosity are then used to compute a Reynolds number. The Reynolds number is then used with the Prandtl number and empirical correlations to compute a Nusselt number. From here, the heat transfer coefficient, inner surface area, and temperature difference between the wall and the fuel provide the actual heat load transferred to the fuel. If the actual value and target value match, the process has converged. If no convergence is reached between the actual and target value, then a new value is assumed on the aspect ratio and width and the process continues until convergence. The final Reynolds number is also used to compute the friction factor. This friction factor can quantify the pressure loss of the working fluid as it works its way through the non-frictionless passage and absorbs heat.

The cooling sub-model can be used to test different allowable pressure drops to be expected by such a cooling system. A pressure drop across the cooling subsystem will result in increased work that must be done by the fuel turbopump thus dropping the specific impulse of the gas generator [37]. The computed cooling jacket inlet pressure is determined by adding the pressure drop with the specified inlet manifold pressure set as the operating pressure for the engine. The cooling jacket inlet pressure is the pump-out pressure requirement for the system to achieve the appropriate level of cooling required by the engine. This provides the ability to understand design choices as cooling these engines will pose a significant challenge in the pathway to flight qualification standards.

Chapter 4: Overview of Engineering Model Implementation and Sample Engine Design

This chapter provides an introduction and overview of the RDRE engine performance and sizing code written by Paxson et al. out of NASA Glenn Research Center [37]. The initial sample case will be replicating a deflagration based constant pressure RP-1/LOX Alpha-1 stage engine design provided by Huzel at al. [45]. Significant improvements in performance metrics are noted and discussed.

The code inputs will be introduced along with descriptions and the units if any. This information will be provided along with values used to later simulate an example case. The structure of the code outputs will be introduced along with the computed results from the example case. The code computed performance and sizing will then be compared with actual engine operating conditions and performance data gathered from available hot fire experimental RDRE test data. Lastly, the code will be run varying individual parameters of interest to produce parameter sweep data. This data will be presented and discussed, providing insight into important RDRE design considerations and trades. The Excel and MATLAB code were obtained from NASA through a formal request through the NASA Software catalog.

4.1 Example Model Usage

4.1.1 RDRE Geometry

The geometry of the RDRE is defined primarily by non-dimensionalized parameters along with a specified value for the mean engine diameter. This sub-section covers critical geometric parameters and additional equations to compute other commonly used dimensions in RDRE engine design. Such dimensions include the inner and outer diameter of the annular walls. These are driven by a selection for the hub-to-tip ratio and engine mean diameter. The parameter ht is the hub-to-tip ratio which is the ratio of the inner to outer diameter of the chamber walls.

$$ht = \frac{\text{ID}}{\text{OD}} \tag{4.1}$$

Where the inner diameter and outer diameter are dimensionalized by a user input for the engine mean diameter D_{mean}.

$$ID = D_{\text{mean}} ht \tag{4.2}$$

$$OD = \frac{2D_{\text{mean}}}{(1+ht)} \tag{4.3}$$

The channel width CW otherwise known as the annular gap can also be found via the following expression:

$$\text{Channel Width } (CW) = D_{\text{mean}} \frac{(1-ht)}{(1+ht)} \tag{4.4}$$

A user selection for the aspect ratio of the engine provides a value for the actual physical length of the engine from the injection face to the chamber exit.

$$L_{\text{act}} = 2AR_{\text{RDRE}} CW \tag{4.5}$$

This parameter is defined as the ratio of the actual engine length to the hydraulic diameter, or annular gap of the channel.

$$AR_{\text{RDRE}} = \frac{L_{\text{act}}}{\text{hydraulic diameter}} = \text{constant} \tag{4.6}$$

4.1.2 Inputs

The following section aims to introduce all model inputs, their notation as written in the MATLAB application, and other options and tags that can be activated or deactivated.

These are broken up categorically by the primary engine inputs, the chamber cooling inputs, turbopump inputs, and finally parametric sweep inputs. Within the primary inputs, the user controls the propellant and reaction chemistry, the boundary conditions such as operating temperatures and pressures, the geometry parameters including the engine diameter, and lastly heat transfer. There is an option to utilize the summer field approximation. The logic flag determines whether the Summerfield approximation for separated flow in over expanded nozzles is applied. If this setting is not activated, or set to 0, the pressure ratio at which the flow separation occurs is set to 0.0002 and if the setting is activated, the value of 0.37 is used. The results obtained in this report are with the Summerfield approximation setting not turned on. The flow is then assumed to separate very easily and as such will provide a more conservative estimate on performance. Further to note, the time-step for the solver is non-dimensionalized by the wave transit time

The values of the primary inputs were selected to produce a similar thrust RDRE as the hypothetical Alpha-1 (A-1) engine design provided by Huzel and Huang in table 3-2 of the textbook on design of liquid-propellant rocket engines [45]. The calculations of these parameters will not be provided, however, engine data will be tabulated to compare to a modeled RDRE. Note, the RDRE design was not optimized and could provide even further improvements on the predicted performance.

This data serves as reference to compare the RDRE model predicted performance results. The thrust value of the RP-1 and LOX A-1 engine is 750,000 lbf. The engine has a turbopump feed system and uses the same propellant for its gas generator and is

regeneratively-fuel-cooled [45]. As such, the RDRE will be modeled with similar engine pump feed and regenerative cooling system architecture as provided by Huzel et al. A brief discussion will be provided on the comparison of engine performance. A schematic diagram of the deflagration engine being compared to in this chapter is shown in Fig. 4.1.

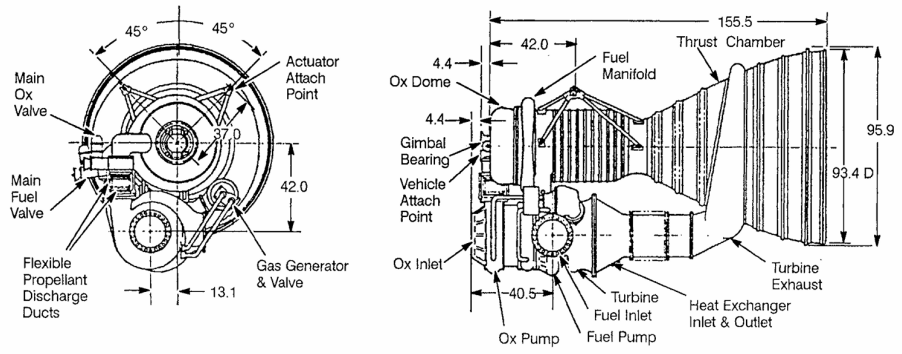

Figure 4.1: A-1 constant pressure deflagration based engine schematic [45].

In modeling this engine, the oxidizer and fuel temperatures at the inlet to the pump were not changed given the densities of both propellants matched reasonably well with the cited value in the text. Both the oxidizer and fuel pumps are assumed to operate at the same efficiency in the RDRE model. The pump efficiency was chosen as the lower of the two cited pump efficiencies with a value of η_p of 65.8%. The model also set A-1 matching turbine efficiency η_t and pressure ratio PR_t the be the same at 23.7 and 58.2% respectively. Both engines are operating at sea-level ambient conditions and their mixture ratios were chosen to be the same. The area ratio of the nozzle for the RDRE was matched as well. The Prandtl number used for heat transfer was set to 0.7, the cooling efficiency was set to 0.8, this is an assumed value. The aspect ratio of the RDRE was chosen to be 3. The injector pressure loss was set such that the initial pressure value in the code matched the injector end pressure provided in the text. The RDRE gas generator is set to 700 psi.

The thrust was used as the matching performance parameter. The last input window on the GUI is the parametric sweep utility that enables an input to be varied across a specified number of points within a range. This utility was first used to obtain a diameter that provides a close enough thrust value to the Huzel A-1 engine of 750,000 lbf [45]. The first mean engine diameter parameter D_{mean} value was selected by performing a parametric sweep on diameter without the cooling and turbomachinery sub-models activated. This initial diameter should provide the necessary mass flow rate estimates by the RDRE model assuming equivalent injection characteristics.This process provided a ball park of about 30 inches for the engine mean diameter aligning with the A-1 engine chamber diameter. The parametric sweep settings used in the last tab within the inputs window of the MATLAB RDRE blowdown application are provided in Tab. 4.1.

The output data for these parametric sweeps are accessible to be exported into the MATLAB workspace for further processing. The MATLAB application also enables the user to rapidly plot the results of these sweeps to understand performance trends with this varied parameter. Fig. 4.2 shows the utility of the user interface in performing these single parameter sweeps. The user interface shows the input to vary being the mean diameter of the RDRE. The four other inputs to provide the start value, the end

Table 4.1: Parametric sweep configuration summary.

Parametric Sweep Parameters	
Parameter Description	**Setting**
Input to vary	D_{mean}
Start Value	15
End Value	35
Number of Points	30
Sweep filename	tmp

value, and total number of points to compute in that range and a file name for this sweep in case further processing is required. On the right hand side, there is a box called plot settings, allowing the user to easily change the X-axis and Y-axis data as well as the sweep file name. The figure in the example shows the X-axis data being the mean diameter values generated via the sweep range, and the Y-axis is the Isp gain relative to an idealized deflagration based rocket engine. The drop down menu shows the wide range of parameters able to be plotted.

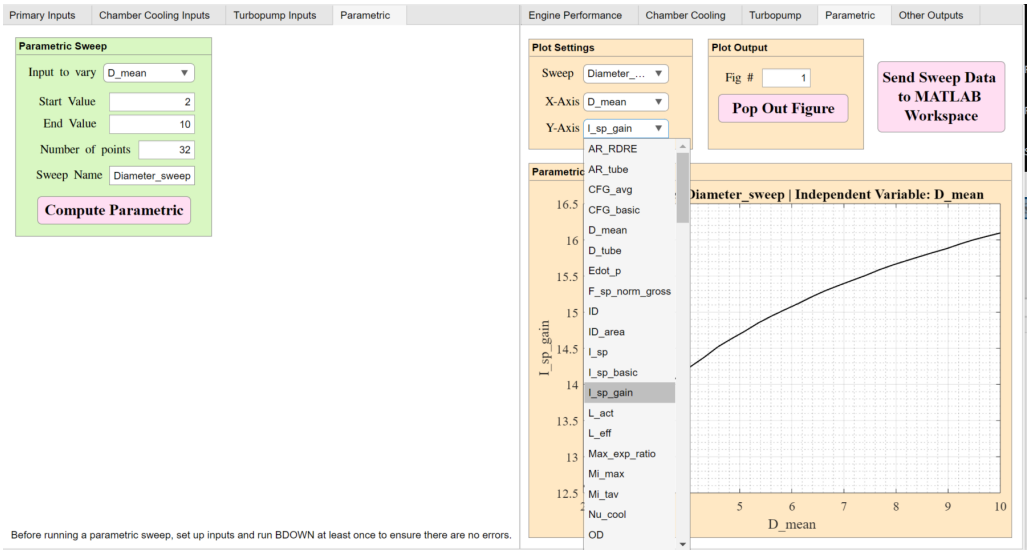

Figure 4.2: Screen capture of the user interface for the MATLAB RDRE blowdown model showing the parametric sweep input and output boxes with an automated plotting feature.

From here, the cooling system and an open cycle gas generator powered turbopump feed system were modeled. The additional losses were captured by replicating the isentropic efficiencies provided by Huzel for the A-1 engine design. The values and units of the respective parameters, if any, as organized in the primary inputs tab are provided in Tab. 4.2. These are the exact same inputs able to be provided via a MATLAB script. The English unit system is used and will be the system used in further discussion to follow in this report.

The chamber cooling inputs tab allows for selection of the critical parameters provided in Tab. 4.3. This tab allows for preliminary analysis of the cooling system requirements assuming a constant wall temperature the cooling system must maintain. If the combination of the fuel inlet temperature with the cooling tube geometry selection criteria does not provide sufficient cooling capabilities, the code will throw an error stating the

Table 4.2: RDRE primary model input parameters and example values.

Propellants & Reaction Chemistry			
Description	**Variable**	**Value**	**Units**
Fuel Type	`Fuel`	RP-1	-
Oxidizer	`Oxid`	O_2	-
Equivalence Ratio	ϕ	1.545	-
CEA Outputs			
Gamma (γ)	`Gamma`	1.17208	-
Specific Gas Constant	R_g	47.827	ft-lbf/lbm-°R
Heat of Reaction	h_r	12119	BTU/lbm
O/F Ratio	OF	2.204	-
Boundary Conditions			
Manifold Temperature	T_m	540	°R
Manifold Pressure	P_m	1500.0	psi
Injector Loss	V_{loss}	0.667	-
Initial Pressure	P_{in}	1000.50	psi
Wall Temperature	T_w	2400	°R
Ambient Pressure	P_{amb}	14.70	psi
Geometry			
Throat Area Ratio	A_t/A	0.80	-
Exit Area Ratio	A_e/A_t	14.0	-
Mean Diameter	D_{mean}	27.27	in
Hub-to-tip Ratio	h/t	0.80	-
Heat Transfer & Other Options			
Prandtl Number	Pr	0.7	-
Combustion Efficiency	η_c	0.97	-
Summerfield Approximation	Logic	Unchecked	-
Timestep	dt_i	0.001	-

temperature of the supercritical fluid as it is assumed within the cooling chamber is over the high temperature limit. When the coolant temperature exceeds a certain threshold, the cooling tube geometry must be adjusted, or the mass flow rates reduced to ensure lower release of energy in the system. These are complex trades that require careful analysis. The values used as example inputs do not suggest an optimal configuration.

Altering values on parameters such as the the fraction of tube area that absorbs heat can provide predictive capabilities into efficiency gains that improved cooling system designs can provide. For example, the current value assumes that 80% of the available surface area is being utilized for heat transfer. Novel additive manufacturing techniques enable construction of complex gyrodial geometries that facilitate increased fluid surface area contact without sacrificing increased structural volume and weight requirements. This serves as a technological pillar worth considering for the future of propulsion system design.

Tab. 4.4 provides the input parameters for the propellant feed system model. To recall, the open cycle gas generator modeled in this code moves propellant by transferring energy harnessed from a smaller combustion chamber which drives a turbine and then dumps the combusted gas overboard, not generating any extra thrust. As such, the efficiency parameters here will dictate Isp losses of the engine. The turbomachinery box

Table 4.3: RDRE cooling system input parameters.

Coolant Properties			
Description	**Variable**	**Value**	**Units**
Coolant Type	`Coolant`	RP-1	-
Average Density	ρ	42.023	lbm/ft^3
Average Specific Heat	c_p	0.608	BTU/lbm-°R
Average Thermal Conductivity	k	0.0656	BTU/hr-ft-°R
Average Viscosity	μ	0.000188	lb/ft-s
Average Temperature	T	803	°R
Cooling Tube Geometry			
RDRE Aspect Ratio	AR_{RDRE}	3.00	-
Tube Wall Thickness	t_{wall}	0.030	in
Tube Aspect Ratio	AR_{tube}	4.0	-
Fraction of Tube Area Absorbing Heat	η_{cool}	0.80	-
Inlet Temperatures			
Fuel Inlet Temperature	$T_{fuel,in}$	540	°R
Oxid Inlet Temperature	$T_{oxid,in}$	160	°R
Cooling Options			
Simulate Cooling	-	Checked	-
Simulate Regenerative Cooling	-	Checked	-

allows for modification to the isentropic efficiency values for the turbine and pump as well as the turbine pressure ratio. As discussed, matching efficiency values to that of the A-1 engine are used.

Modern turbomachinery and improved pump design and manufacturing capabilities enabled by additive manufacturing will likely result in further increase to the efficiency this particular system. Note, the tank pressure is set to 45 psi as this is the value provided for the fuel-side pump inlet pressure for the A-1 engine.

Table 4.4: RDRE gas generator and turbomachinery input parameters.

Gas Generator Reaction Chemistry			
Description	**Variable**	**Value**	**Units**
Fuel Type	`Fuel`	RP-1	-
Oxidizer	`Oxid`	O2	-
Equivalence Ratio	ϕ_{gg}	7	-
Omit Species	-	C(gr) H2O(cr) H2O(L)	-
Pressure	P_{gg}	700.00	psi
Gas Generator CEA Outputs			
Gamma	γ_{gg}	1.13823	-
Specific Gas Constant	R_{gg}	71.472	ft-lbf/lbm-°R
Temperature	T_{gg}	2342	°R
O/F Ratio	OF_{gg}	0.487	-
Turbomachinery			
Turbine Efficiency	η_t	0.582	-
Pump Efficiency	η_p	0.658	-
Turbine Pressure Ratio	PR_t	23.7	-
Tank Pressure	P_{tank}	45.00	psi
Inlet Conditions			
Fuel Inlet Density	$\rho_{fuel,in}$	49.240	$\mathrm{lbm/ft^3}$
Oxid Inlet Density	$\rho_{oxid,in}$	71.613	$\mathrm{lbm/ft^3}$
Options			
Simulate Turbopump	-	Checked	-
Simulate Gas Generator	-	Checked	-

4.1.3 Outputs

The code is then executed with these inputs set. The engine performance tab within the GUI first provides the main performance summary and refill conditions along with the limit cycle plots for pressure, temperature, thrust and mass flow rate are provided to the user. The limit cycle pressure as a function of cycle time is provided in Fig. 4.3 for the example case outlined in the inputs subsection. Note the time scale of the limit cycle is of the order of 100 microseconds. The pressure from the detonation model for this case results in a maximum of 8821.14 psi with a cycle time averaged pressure of 2116.96 psi. This value was obtained by adding several lines to the MATLAB script to compute the integral of the cycle parameter data divided by total time for the limit cycle.

The engine performance summary along with the refill conditions computed by the code are tabulated in Tab. 4.5. There are two mass flow rates provided and described by comments in the code [65]. The first, $\dot{w}_1$, is computed by using the initial state of the tube along with the total volume of the RDRE determined by the effective length and the cycles frequency in addition to the gas generator consumption. The second mass flow rate provided, $\dot{w}_2$ is the total mass flux through the engine exhaust in addition with the gas generator consumption. These two values are only off by 2.3 lbm/sec for this case indicating good agreement. The effective length parameter provided in this output box has been discussed earlier and its description is also provided in a comment within the code. The comment next to this variable states L_{eff} is the required length of the PDE tube such that the cycle is complete by the time the detonation wave has made its way

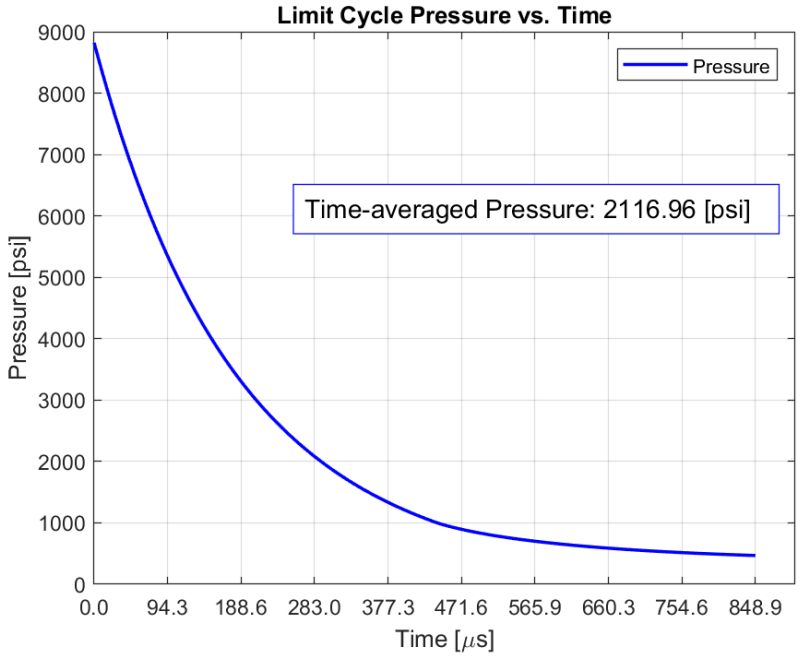

Figure 4.3: Pressure versus time of the the limit cycle obtained from the the RDRE performance model at sample input conditions.

around the circumference of the engine annulus. The refill conditions provide information on the injection scheme being modeled.

Table 4.5: Main outputs of RDRE model along with performance parameters and values for sample design.

Performance Summary			
Description	**Variable**	**Value**	**Units**
Frequency	f	1178	Hz
Thrust	F	750,305	lbf
Specific Impulse	I_{sp}	301.50	sec
Total Mass Flow	$\dot{w}_1$	2488.5	lbm/sec
Total Mass Flow	$\dot{w}_2$	2490.8	lbm/sec
Effective Length	L_{eff}	5.63	in
Peak Pressure	P_{det}	8821.14	psi
Refill Conditions			
Fill Mach Number (avg)	$M_{i,avg}$	0.837	-
Fill Mach Number (max)	$M_{i,max}$	1.000	-
Fill Speed Of Sound	a^*	1019.6	ft/sec
Fill Pressure	P_{fill}	468.71	psi

The calculated geometric parameters necessary to provide sufficient cooling capabilities to the hypothetical engine are provided along with the number of tubes necessary to have along the outer and inner diameter of the engine walls. This information is critical to understand to design and validate these values with more advanced heat transfer models, CFD, and experimentation. This data can also inform manufacturing tolerance requirements to ensure chamber coolant channels deliver sufficient performance.

Table 4.6: RDRE calculated geometric parameters and cooling data.

Calculated Geometric Parameters			
Description	**Variable**	**Value**	**Units**
Engine Length	L_{act}	18.18	in
Chamber Outer Diameter	OD	30.30	in
Chamber Inner Diameter	ID	24.24	in
OD Surface Area	-	1730.56	in^2
ID Surface Area	-	1384.45	in^2
Tube Width	w_{tube}	0.0943	in
Tube Hydraulic Diameter	D_{tube}	0.1029	in
# of OD Tubes	-	1009	-
# of ID Tubes	-	808	-
Calculated Cooling Tube Parameters			
Tube Heat Load	Q_{tube}	134.0	BTU/s
Tube Mass Flow	w_{tube}	0.419	lbm/s
Tube Flow Velocity	U_{tube}	86.7	ft/s
Coolant Prandtl Number	Pr_{cool}	6.08	-
Coolant Reynolds Number	Re_{cool}	1.72e+05	-
Coolant Nusselt Number	Nu_{cool}	611.0	-
Friction Factor	f	0.01606	-
Regenerative Cooling			
Mass-Avg Exhaust Total Temperature	T_{max}	9086	°R
Adiabatic Exhaust Total Temperature	T_{adb}	9340	°R
% Chemical Energy to Walls	$q_{frac,wall}$	2.72	%
Total Heat Load	Q_{cool}	243488.2	BTU/s
Coolant (Fuel) Mass Flow	w_{cool}	760.8	lbm/s
Fuel Outlet Temperature	$T_{fuel,out}$	1067	°R
Cooling Jacket Inlet Pressure	$P_{fuel,in}$	1596.848	psi

The turbopump output tab in the output window of the GUI provides the parameters and associated values for important parameters necessary for turbine and pump design. The resulting turbopump system performance is provided in Tab. 4.7.

Table 4.7: Turbopump parameters and output values.

Turbopump Outputs			
Description	**Variable**	**Value**	**Units**
Specific Pump Power	$\dot{e}_p$	6.7	BTU/lbm
Specific Turbine Power	$\dot{e}_t$	329.0	BTU/lbm
Req'd Pump Power	$\dot{E}_p$	23655	hp
Req'd Turbine/GG Mass Flow	$\dot{w}_{gg}$	50.8	lbm/sec
Gas Generator Outputs			
Description	**Variable**	**Value**	**Units**
ISP without gas generator	-	307.79	sec
ISP with gas generator	-	301.50	sec
ISP lost due to gas generator	-	6.29	sec

The turbopump properties function file had to be modified to correct unit conversion on the specific power parameters. The specific power input as defined in the code had to be divided by 778.2 to properly convert from ft-lb to BTU as the previous value was really reporting the DH of the pump in units lb-ft/lbm.

Table 4.8: Summary of main RDRE performance parameters.

Description	**Value**	**Units**
Thrust	750,000	lbf
Specific Impulse	262.4	s
Flow Rate (LO2 + RP-1)	2,860.0	lb/s
Oxidizer Pump Power	14,850	hp
Fuel Pump Power	11,790	hp
Total Pump Power	26,640	hp
Power Output by Turbine	27,140	hp
Gas Generator Flow Rate (Combined)	157.3	lb/s

The A-1 engine performance parameters are tabulated and compared to the results obtained by the RDRE model. The hypothetical RDRE propulsion system modeled as an open cycle gas generator turbopump fed RP-1 and O_2 engine produces 301.50 seconds of Isp. This is a 39.1 second improvement over the A-1 stage engine design provided by Huzel et al. [45]. This is a significant performance of 14.91%. These levels of improvement in Isp can mean very significant reductions on payload mass to orbit or reduced fuel and oxidizer storage requirements.

Table 4.9: Comparison of baseline deflagration and modeled RDRE performance parameters.

Description	**A-1**	**RDRE**	**Percent Change**	**Units**
Thrust	750,000	750,035	0.005%	lbf
Specific Impulse	262.4	301.50	14.91%	s
Total Mass Flow Rate	2,860.0	2,488.5	-12.97%	lb/s
Oxidizer Pump Power	14,850	-	-	hp
Fuel Pump Power	11,790	-	-	hp
Total Req. Pump Power	26,640	23,655	-11.22%	hp
Power Output by Turbine	27,140	23,676	-12.75%	hp
Required Turbine Flow	92	50.8	-44.78%	lb/s

Table 4.10: Comparison of constant pressure RP-1/LOX Engine A-1 (rocket engine system design by Huzel et al. [45]) with RDRE of equal thrust and equivalent operating conditions.

Description	Units	A-1	RDRE	Percent Dif.
Thrust	lbf	750,000	750,035	0.005%
Specific Impulse	s	262.4	301.50	14.91%
Total Mass Flow Rate	lb/s	2,860.0	2,488.5	-12.97%
Oxidizer Pump Power	hp	14,850	-	-
Fuel Pump Power	hp	11,790	-	-
Total Req. Pump Power	hp	26,640	23,655	-11.22%
Power Output by Turbine	hp	27,140	23,676	-12.75%
Required Turbine Flow	lb/s	92	50.8	-44.78%

Table 4.11: Comparison of constant pressure RP-1/LOX Engine A-1 (rocket engine system design by Huzel et al. [45]) with RDRE of equal thrust and equivalent operating conditions.

Dimension	Units	A-1	RDRE	Percent Dif.
Chamber Diameter	inches	31.50	30.30	-3.81%
Chamber Length	inches	31.00	18.18	-41.35%
Chamber Volume	in^3	21,915	4740.29	-78.37%

Chapter 5: RDRE Parametric Analysis

This chapter provides investigates parametric analysis on RDRE performance. Parametric analysis is important to understand performance sensitivities and correlations to various design input parameters. Parametric analysis can also provide insight into engine performance under varying operating conditions. As an example, understanding how thrust and specific impulse are affected by varying inlet manifold pressures could be useful for the design of a trottleable RDRE system. Parametric analysis can enable design optimization and provide general intuition to RDRE design considerations. Understanding if a parameter results in a linear or exponential increase in heat load to the engine can inform cooling system design choices in the conceptual level design phase. Analysis on changing a particular input parameter and the effect this parameter has on mass flow rate can, for example, inform fuel tank sizing and storage considerations. This data can then be used to optimize trajectories for given mission and payload requirements. The present RDRE performance and sizing model enables rapid parametric analysis and the resulting performance trends and other insights will be discussed in this chapter.

5.1 Single Parameter Sweeps and Discussion

The following section will cover performance behavior trends under single parameter sweeps, a useful feature provided in the user interface of the MATLAB application for the RDRE blowdown model. An example of this window has been provided in chapter 4. The single parameter sweeps were executed without the cooling and gas generator driven turbopump sub-model activated and with no cooling modeled. The wall temperature was held constant along with other major input parameters. These are summarized in Tab. 5.1. These input parameters are to be considered the default parameters and unless otherwise specified, are the inputs used while a different parameter is varied. For example, the engine being modeled has a 3 inch mean diameter, and for a parametric sweep on *phi*, all parameters remain constant. However, the default equivalence ratio ϕ when sweeping values of diameter is held fixed at 1.3.

5.1.1 Methodology

After setting the various inputs in the MATLAB application GUI parametric tab, each parameter is swept across 20 test points within the specified range. The outputs are then stored in the MATLAB workspace and processed by a MATLAB script written to automate the storage of the data into `csv` files. Each file is named by the script according to a parameter that is detected as being varied within each data structure.

Table 5.1: Default primary input parameters and values used for single parameter sweep analysis.

Propellants & Reaction Chemistry			
Description	**Variable**	**Value**	**Units**
Fuel Type	`Fuel`	RP-1	-
Oxidizer	`Oxid`	O_2	-
Equivalence Ratio	ϕ	1.3	-
Boundary Conditions			
Manifold Temperature	T_m	540	°R
Manifold Pressure	P_m	1500.0	psi
Injector Loss	V_{loss}	0.9	-
Initial Pressure	P_{in}	1350.0	psi
Wall Temperature	T_w	2400	°R
Ambient Pressure	P_{amb}	14.70	psi
Geometry			
Throat Area Ratio	A_t/A	0.80	-
Exit Area Ratio	A_e/A_t	22.0	-
Mean Diameter	D_{mean}	27.27	in
Hub-to-tip Ratio	h/t	0.80	-
Heat Transfer & Other Options			
Prandtl Number	Pr	0.7	-
Combustion Efficiency	η_c	0.97	-
Summerfield Approximation	Logic	Unchecked	-
Timestep	dt_i	0.001	-

Once all parametric sweeps were performed, the data was processed and visualized with Python.

Table 5.2: Swept parameters and ranges.

Description	**Variable**	**Range Low**	**Range High**
RDRE Aspect Ratio	AR_{RDRE}	2.0	8.0
Mean Diameter [inches]	D_{mean}	1.0 in	20
Hub-to-tip Ratio	ht	0.5	0.98
Manifold Pressure [psi]	P_{man}	100	2000
Equivalence Ratio	ϕ	0.5	2.0

5.1.2 Equivalence Ratio

A parametric sweep was performed by varying the equivalence ratio from 0.5 to 2 with 20 test points along this range. This sweep provides insight into performance of the engine under different fuel and oxidizer mixture ratios.The equivalence ratio of 1 is the stoichiometric ratio with a value above 1 being a fuel rich mixture and below 1 is a lean mixture where oxidizer is in excess. The model predicts maximized Isp of the engine with an equivalence ratio of about 1.2. The plot of specific impulse performance as a function of equivalence ratio is provided in Fig. 5.1.

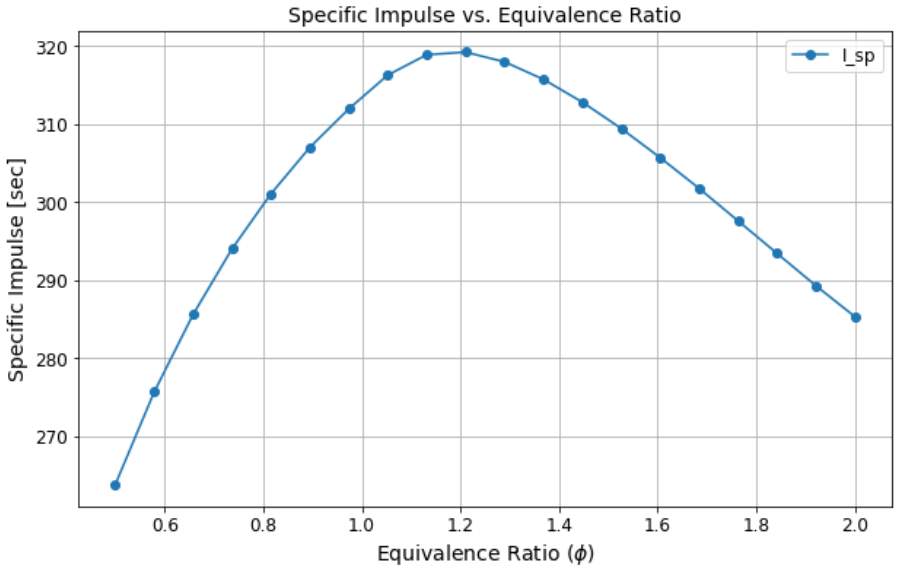

Figure 5.1: Specific impulse performance computed by the RDRE blowdown model across a range of equivalence ratios (ϕ) for RP-1/O_2.

5.1.3 Inlet Manifold Pressure

Similar to the plots provided by Paxson [37], the parametric sweep feature was used to estimate the specific impulse performance of this engine under varying inlet manifold pressures. Twenty pressures were used from 200 to 2000 psi. The results are seen in Fig.5.2. The trend indicates reduced rate in increase of specific impulse performance with increasing inlet pressure. This gives good insight in the design process as marginal gain of increasing the manifold pressure from 1000 psi to 2000 psi is only about 14 seconds. This aligns with what was reported by Paxson et al. [37].

5.1.4 Mean Engine Diameter

Continuing, the next parameter of interest that was swept while holding all other parameters constant was the mean diameter of the engine. A large diameter results in an increased annular area through which more mass can flow. Asides from obvious increases in thrust and mass flow rate, other factors such as the specific impulse were seen to increase. Other trends in the estimated performance specifications as predicted via this model were investigated for varied engine diameter. The next few plots will highlight

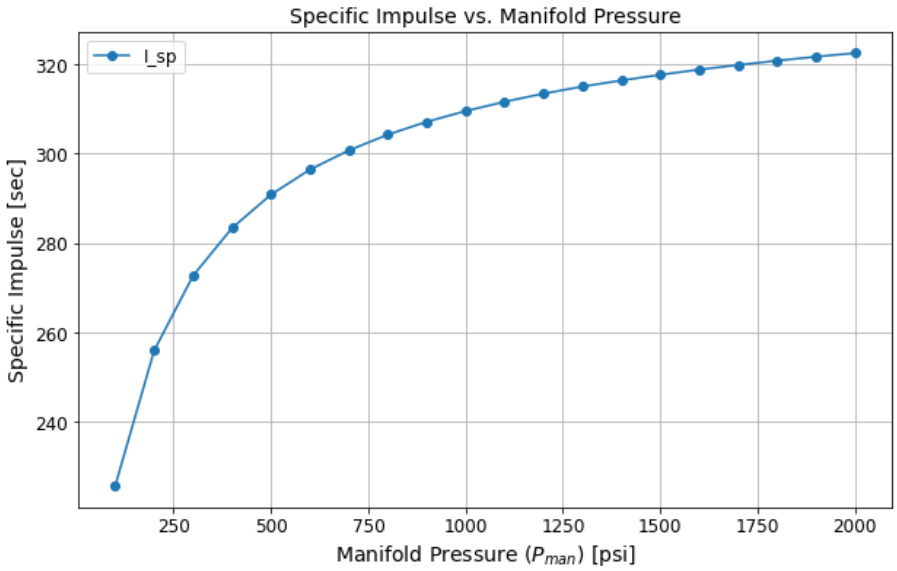

Figure 5.2: Model predicted specific impulse performance as a function of manifold pressure.

important outputs as function of the mean diameter. The mean diameter was varied from 1 inch to 20 inches with a total of 20 data points in this range.

It is straight forward that as the the size of the engine increases with all other major operating conditions and geometric ratios held constant, the mass flow rate increases non-linearly with increasing engine mean diameter. What is interesting to not here is the rate at which thrust increases with increasing engine diameter. This however, also results in significant heat transfer to the walls of the annular combustion chamber (note, this does not take into account heat transfer to the nozzle walls). However, when looking at the chemical energy absorbed by the walls, the overall percentage decreases with both increasing pressure and diameter. This suggests larger engines with higher manifold pressures operate more efficiently. Of course, the total net amount of heat transfer scales rapidly with both parameters increasing. Fig. 5.4 shows the percentage of chemical energy lost to the walls. The trend predicted by the model in varying the manifold pressure indicates improved conversion of chemical energy to production of thrust, and less overall chemical energy being absorbed by the walls. This corresponds to the trend for improved, but plateauing gains in specific impulse with increased manifold pressure. Increasing the mean diameter of the engine also indicates reduced overall chemical energy lost to the cooled walls. This parameter was then later used as a proxy for selecting engines that require lower overall cooling. There will be more discussion on this in the following chapter.

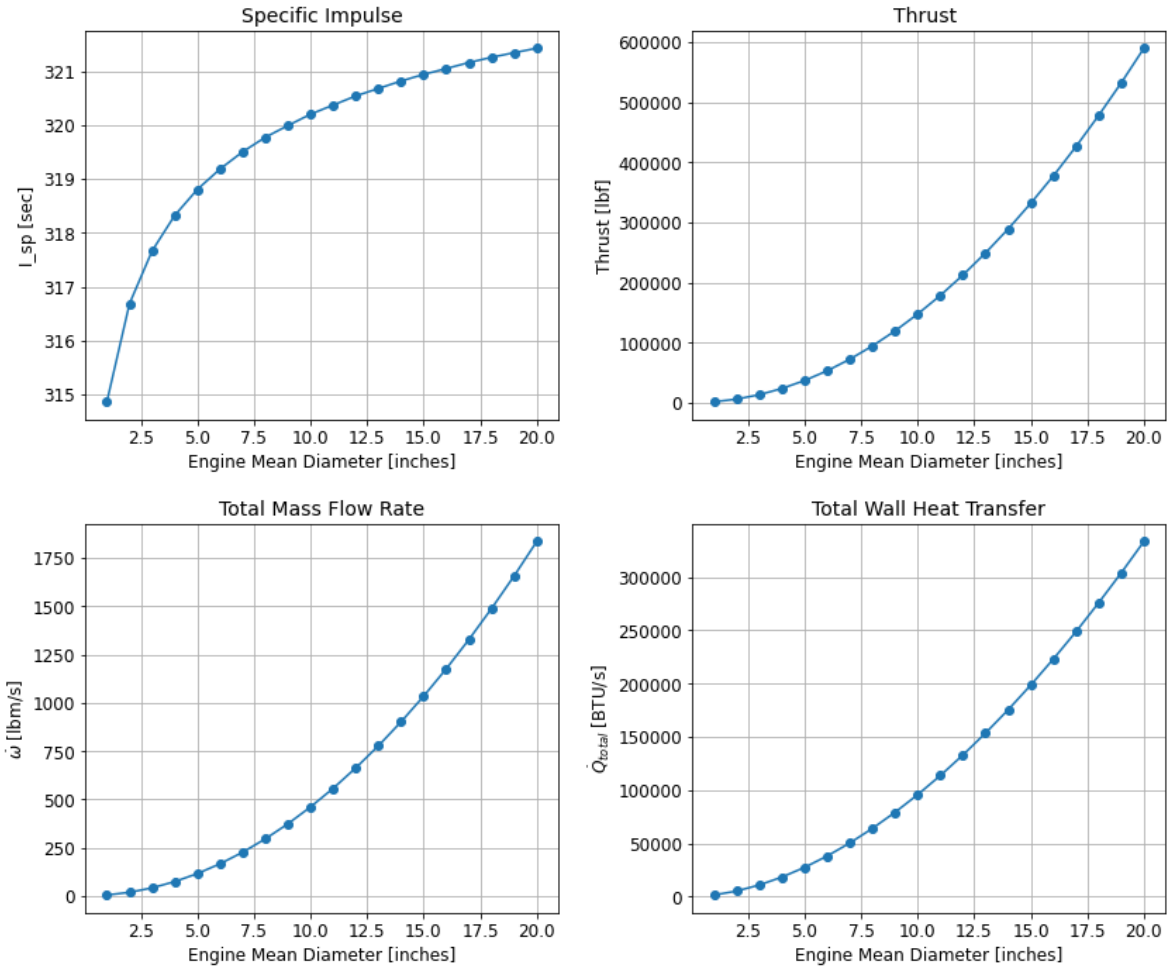

Figure 5.3: Various RDRE performance parameters for a parametric sweep on the engine mean diameter. The specific impulse, thrust, total mass flow rate and the total heat transfer to the wall are shown in order.

5.1.5 Effect of Turbopump and Gas Generator

Parametric sweeps were then performed with the turbopump submodel activated. The equivalence ratio of the gas generator was set to 7. The pressure of the gas generator was set to 1500.0 psia and the fuel used for the gas generator was also RP-1. The pump efficiency was set to 0.9 and the turbine pressure ratio and efficiency were set to 3 and 0.6 respectively. The turbopump sub-model inputs are provided in Tab. 5.3. The parametric analysis was performed again to see the net effect of having to run a turbopump powered by a gas generator cycle with the following parameters set to model the turbopump and gas generator subsystem.

Table 5.3: RDRE turbomachinery submodel input parameters and respective values.

Turbomachinery Model Inputs	
Turbine Efficiency η_t	0.600
Pump Efficiency eta_p	0.900
Turbine Pressure Ratio PR_t	3.000
Tank Pressure P_{tank} (psi)	14.70

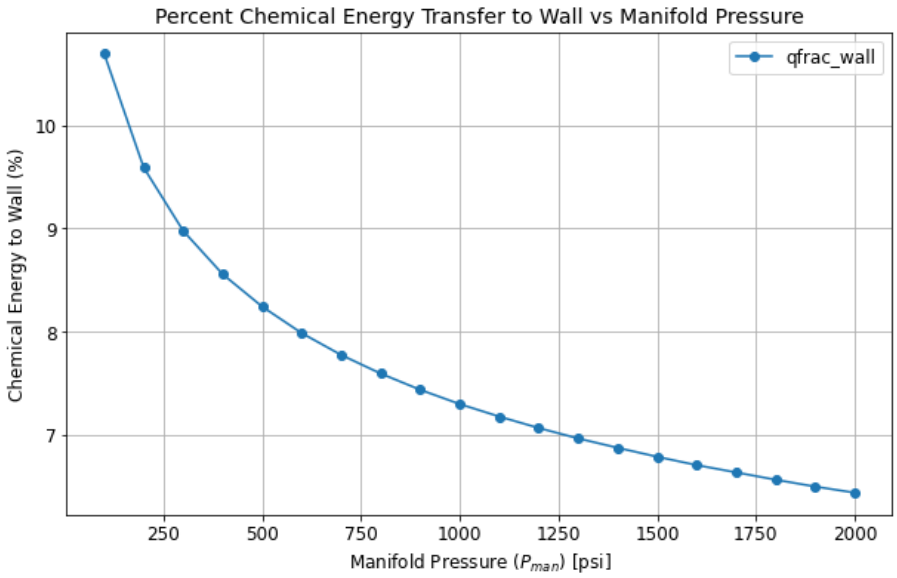

(a) Percent chemical energy lost to walls as a function of varying manifold pressure.

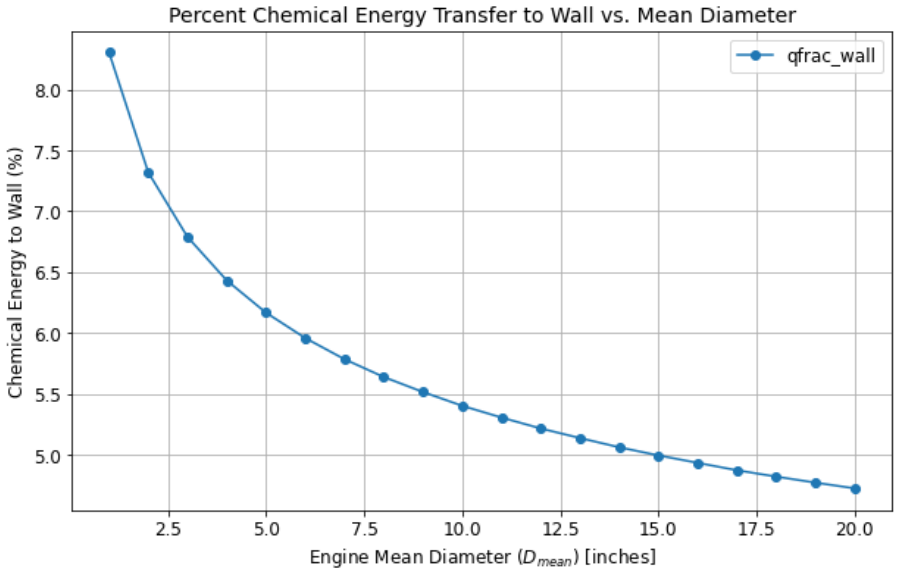

(b) Percent chemical energy lost to walls as a function of engine mean diameter.

Figure 5.4: Percent chemical energy lost to walls for two parametric sweeps performed using the RDRE blowdown model.

As seen in Fig. 5.5, there is a net loss in specific impulse due to the gas generator and turbopump with the parameters set in Tab.5.3. The gains in specific impulse essentially top out after about 1000 psi. This aligns well with the predicted performance trends from [37]. These types of parametric sweeps can assist in the preliminary trade studies for an RDRE. These results might suggest that the induced cost in weight, complexity, and size of the turbopump system may not be worth the marginal performance increase in the specific impulse of the engine. On the other hand, thrust does go up significantly even with increasing pressure. As expected, the thrust values should be the same as the pressure at the inlet should be the same with or without the turbopump since the turbopump

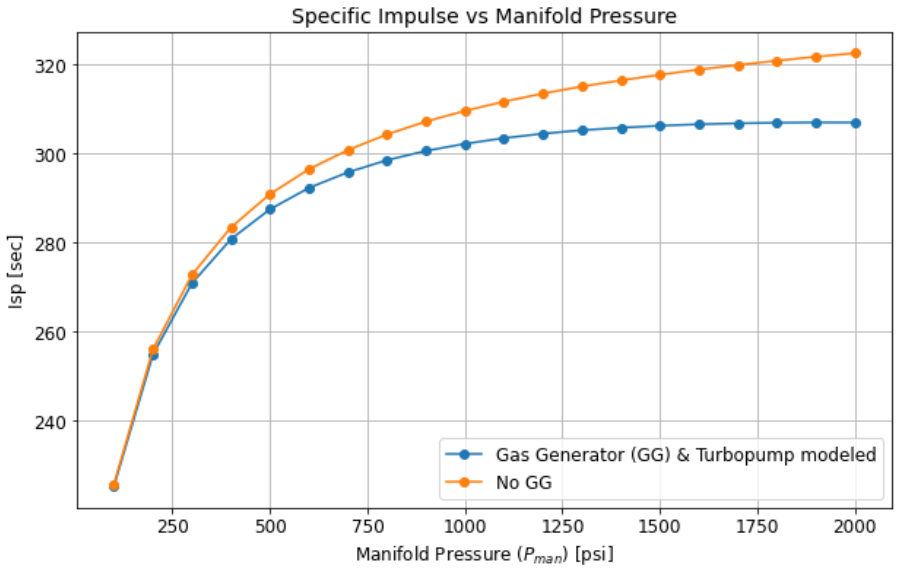

Figure 5.5: Performance effects of modeling the gas generator and turbopump for the RDRE.

calculations are based on the necessary pressure output at the manifold to be equal to the user provided input manifold pressure. In this case, if an engine has a set requirement on thrust, a smaller engine with higher turbopump capabilities may achieve necessary performance even with the cost of improved turbopump subsystem requirements. These are all complex and dynamic trades that must go on in the design of a propulsion system. The total mass flow rate with the gas generator and turbopump modeled is slightly higher over the case when no gas generator is modeled. This is explained by the extra propellant required to operate the gas generator at its conditions set for this case. Another parameter that was varied was the hub to tip ratio. According to [37] [65], this parameter still has no special meaning and the limits of this parameter are unknown. The hub to tip ratio, otherwise denoted as ht in the model and code is the ratio of the inner diameter to the outer diameter of the annular combustion chamber. A low value means a large annular gap. A value close to 1 means a very small annular gap relative to the diameter of the engine. Given this definition, it would be clear that reducing the value of ht should result in increased mass flow rate and therefor thrust. This was investigated via a parametric sweep on ht from 0.5 to 0.98 with 20 cases in the range. The results are provided below in Fig.5.7. The specific impulse is seen to decay and then more rapidly drop off after a ht value of about 0.9. The thrust, mass flow rate, and total heat transfer to the walls varies almost linearly with varying hub to tip ratio. Although the total wall heat transfer decreases with increasing ht, the actual percent chemical energy lost to the walls increases with increasing ht. This might indicate that two engines producing similar thrusts and operating at equal mass flow rates and inlet pressures, the lower hub to tip ratio may enable lower cooling requirements compared. This will be further investigated in the next chapter. Thus far, these sweeps have been one dimensional, meaning only one parameter is varied while all others held fixed. To truly dive into engine optimization, these parametric sweeps must be conducted in multiple dimensions to investigate coupled behaviors between different parameters. For example, it is important to understand the trade in increasing the annular gap while and reducing inlet manifold pressure or aim to operate at a higher pressure with a reduced combustion chamber volume. As seen

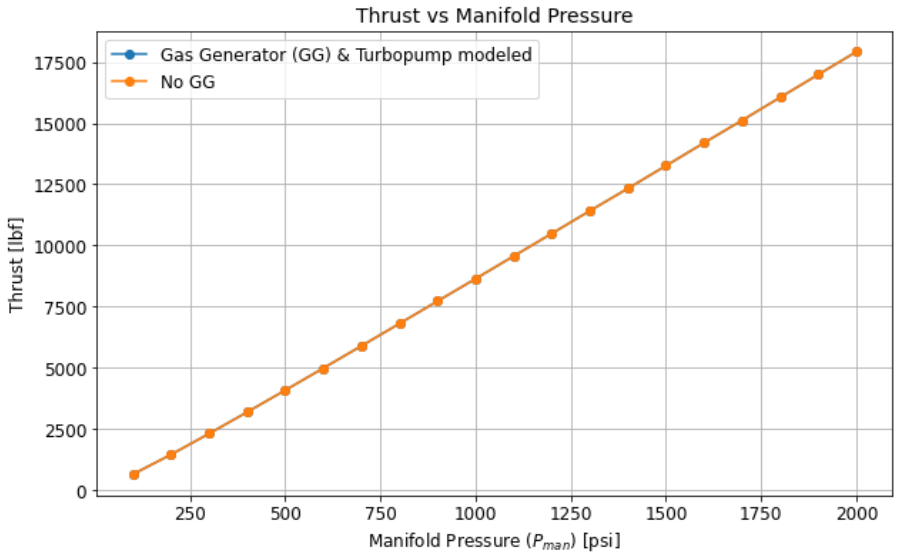

(a) Thrust as a function of manifold pressure.

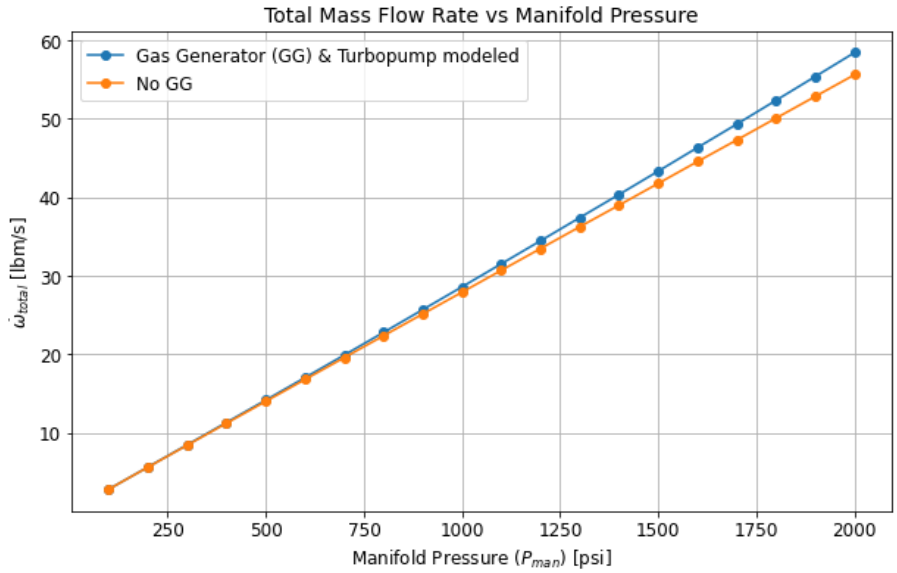

(b) Total mass flow rate in lbs per second as a function of manifold pressure.

Figure 5.6: Manifold pressure parametric sweeps comparing effects on thrust and total mass flow rate for the system with and without the gas generator modeled.

in the previous analysis and through simple intuition, increasing pressure increases mass flow rate. According to these models, the increased pressure improves performance up to a certain point where afterwards, the amount of thrust generated per pound mass of propellant does not increase further. Increasing pressure also decreases the percentage of chemical energy lost to the walls. However, increasing the hub-to-tip ratio increases this value. Further investigation of performance trends under multidimensional variance is critical to map to best optimize engines for certain requirements and mission objectives.

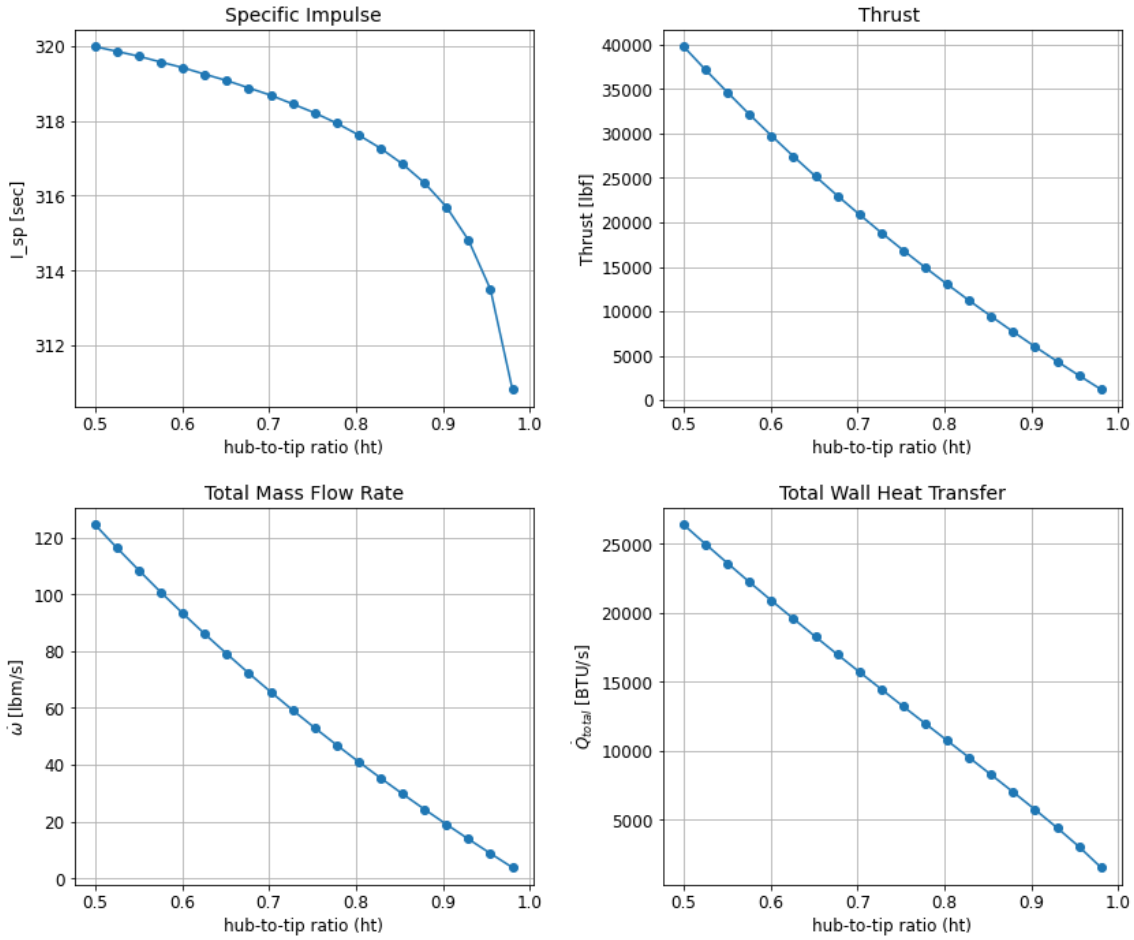

Figure 5.7: Various model predicted outputs for a hub-to-tip ratio sweep. The specific impulse, thrust, total mass flow rate and the total heat transfer to the wall are shown in order.

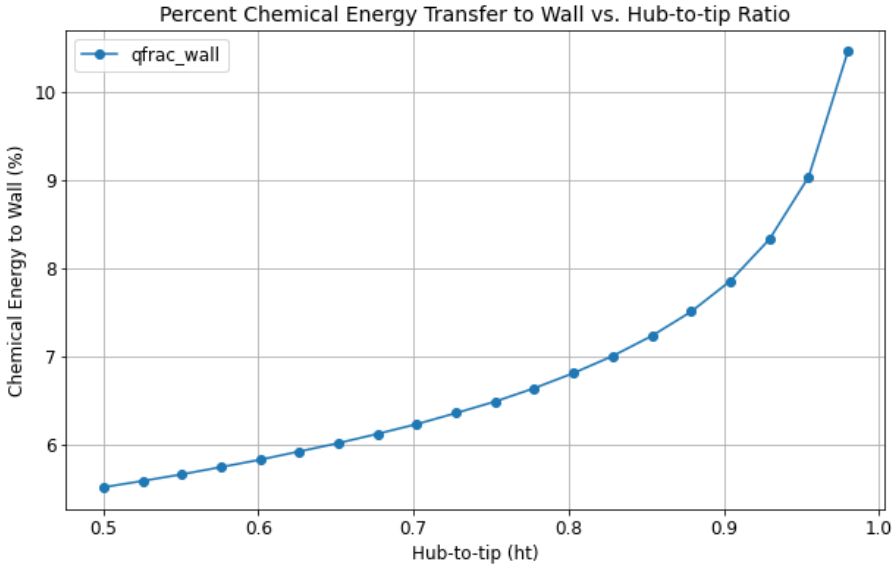

Figure 5.8: Percent of chemical energy lost to walls as predicted by the RDRE model for a sweep on the hub-to-tip ratio.

Chapter 6: Design of Experiments and Optimal Engine Selection

The RDRE blowdown model introduced in previous chapters provides an extremely useful engineering analysis tool that enables rapid assessment of engine sizing and performance. As will be discussed, cases can be run in a fraction of a second when utilizing parallel computing capabilities. The methodology behind this large parametric design of experiments (DoE) is introduced along with discussion on the importance of this approach given the computational efficiency of the tool. Quantitative assessment on this computational efficiency is provided and discussed. The RDRE modeling code is utilized to generate a massive dataset with 463,050 unique engine design configurations by initializing a range of values for critical design parameters. Engine performance trends in multi-dimensional design parameter space are analyzed and results are discussed in depth. This data is then used to inform considerations on optimal design configurations for a set of hypothetical system requirements. The top 10 performing engines as measured by specific impulse for a given thrust class are provided. A final engine design is presented along with a discussion on the driving philosophy behind the selection.

6.1 RDRE DoE

6.1.1 Implementation with MATLAB Parallel Computing

MATLAB's parallel computing library is utilized in the work presented in this chapter. MATLAB's parallel computing toolbox has a `parfor` loop construct used to distribute iterations of the loop across multiple processors or cores taking advantage of parallelized computing. This helps in speeding up computations by performing multiple iterations simultaneously rather than sequentially. This toolbox abstracts the complexity that is involved in managing parallel processes and provides scalability to run on several cores or entire compute clusters without modifying the code. By default, computations are not run in parallel. MATLAB divides the iterations into groups and assign the task to a worker to minimize execution time. MATLAB also handles data transfer between the workers and the workspace to optimize resources. Each iteration is distributed such that no iteration is double counted.

The script was programmed to have five nested `for` loops iterating on each datapoint within the rage of values varied for each input parameter. To avoid extensive compute times given the large number of data points for each parameter, the cases were

distributed over multiple cores or processes.

The computed data along with all input values used to perform computations are appended to a MATLAB structure array. This structure array has data containers called fields. Each field contains the unique parameter and stored numerical value, data or setting used in computing each case. Given how the script was initially structured, the `parfor` construct allocated all computations but would store the data in the MATLAB workspace. The data stored in the workspace is temporary and thus is housed on the computers RAM. Due to the size of the study, the first attempt at modeling all 463,050 engine configurations crashed at the end of the final computation as the size of the workspace exceeded the physical amount of memory available on the machine's RAM. This led to another iteration where the individual cycle data was no longer stored. This data was determined to not be necessary for the purpose of the study and recording the cycle data of each engine results in a large amount of data that needs to be written to memory. The design of experiment study was run again by recording the data in the `gbl` structure array only. The variable would only store up to 500 cases before writing that data from RAM to the actual disc in the form of a comma separated file (`csv`). This file was opened, new data written, and closed before the next 500 iterations were allocated by the `parfor` construct. The array structure with 112 fields for each iteration was converted into a table data structure. This table data structure that holds 500 iterations then gets written to the `csv` file created to hold all resulting cases. It was interesting to find that the `gbl` array structure that holds the data for each parameter in the model for each case occupied 19,712 bytes of RAM. When saving that data to an individual row of a `csv` file with 112 columns, each case only occupies 1205 bytes of memory. It seems that there is extra data being handled by the MATLAB workspace to allow for ease of access to temporary data. In total, for the complete study with 463,050 cases, the predicted RAM allocation necessary to temporarily hold the entire dataset including the cycle data and pressure data for the cycle would have resulted in over 90 GB, far higher than the available resources on the machine used. The actual resulting file was 0.56 GB when saving just the fields of interest from the model.

Table 6.1: Compute time experiment for running the model for 396 design configurations. This was done to benchmark the time reduction for increased core utilization. These values were then used to estimate total time required for different design sweeps.

CPU Cores	Cases Per Core	Compute Time (sec)	Average Time per Case
16	24.75	17.9	0.0452
10	39.6	20.72	0.0523
2	198.0	82.33	0.2079

6.1.2 Initialization of DoE

A full factorial design of experiments was performed on critical engine operating and sizing parameters. Factors with more than one level include the equivalence ratio, manifold pressure, hub-to-tip ratio, the engine aspect ratio, and mean diameter. A total of 463,050 experiments were computed to produce a significantly large data set with granular coverage on many key parametric combinations. This large data set enables both qualitative and quantitative analysis on all engine design combinations and operating conditions. Full factorial designs are critical to examine all possible combinations of factor

levels providing performance optimization, assessment of main effects and interaction effects, sensitivity analysis, and can used to develop predictive machine learning models [72] [73].

The granular dataset can be segmented and filtered based on selected engine specifications that meet system requirements. Once the engine data is filtered by performance or sizing requirements, each engine can be compared qualitatively to assess potential design trades that would need to be made. This gives insight into design considerations that may not otherwise be possible with deflagration based engines. As cited earlier, these RDRE thrust chamber form factors can be shorter relative to the standard deflagration based rocket engine. Furthermore, the selection of the hub-to-tip ratio may provide the ability to adjust more than one radial design parameter to achieve varying performance with the same specified engine diameter.

The design of experiment was initialized to achieve a range of low thrust to high thrust class engines. The parameters were selected on previous intuition in using this code along with cited literature and existing data. The ranges of thrust classes to be covered are of the order 10^2 to 10^5 lbf. From here, the ranges of parameters were selected to have small enough step size to give a granular view while holding certain parameters fixed, providing a top level view of performance trends without sacrificing extensive compute time. However, for the purposes of more intense studies, the compute time is still very low relative to high fidelity CFD tools or other models. Tab. 6.1 summarizes the total time and average time per case for a small DoE of 396 total iterations.

The 396 case experiment was performed using 16, 10, and 2 CPU cores. This data was then used to predict total run time and provide a reference point when planning out the parameters being swept as well as their range of values and step size. The total compute time was measured from the start of launching the task to it finishing but not writing the workspace data to a file. The average compute time per case when utilizing every core available was 0.0452 seconds. This is incredibly fast when comparing to standard simulation tools such as CFD where individual cases for an RDRE could take days to complete on the same machine. Of course the advantage of reduced computational time comes with the cost of model simplicity. However, the anchored model is sufficient to provide conceptual level trade study and mission design analysis. The average time per case is reduced by 78% when when running the model for the same experiment on 16 CPU cores versus 2 CPU cores.

An engine database using RP-1 as fuel and O2 as oxidizer was constructed. The exit area ratio parameter was set to have a value of 23 given this was almost consistently the optimal ratio at sea level conditions as determined by the previous design of experiments in section 5.1. The equivalence ratio ϕ was selected to vary from a slightly lean mixture of 0.90 to a fuel rich ratio of 1.80. The engine is modeled having an open cycle gas generator turbopump propellant feed system. The inlet manifold pressures are varied in increments of 150 psi from 700 to 1300 psi. The upper limit was based on the model predicting marginal specific impulse gains with increasing inlet manifold pressures beyond this value. Beyond the marginal gains in Isp, the effect of driving this pressure higher results in increased performance requirements on the pump feed system. This will drive higher overall weights and sizing of the propulsion system.

The inlet manifold temperature was held at the default value used for RP-1 simulations at 540° R. The hub-to-tip ratio was varied from 0.58 to 0.98 in increments of 0.02. This was chosen to cover a reasonable range of inner to outer diameter ratios. Given the limits of this are not known, it could be possible this does not cover all realistic and

potential values for this geometric parameter. The aspect ratio of the RDRE was also varied to control the total length of the engine's chamber (not including the length of the nozzle). This parameter AR_{RDRE} was varied from 2.0 to 6.0. The rule of thumb value provided in the model by default is 5. However, in [37] the authors mention that engines with lower AR may be possible. Thus, the lower end of this sweep provides insight into potential engines with short axial lengths relative to diameter. This could provide high thrust with low axial length form factors by utilizing larger diameter chambers. This can provide interesting options for reaction control system design where engines can be integrated into the airframe. The side of a capsule or a missile like airframe have limited sizing budgets and RDREs can be mounted in areas where otherwise it may not be possible to fit standard combustion chambers and associated nozzles due to their relatively longer lengths.

The area ratio of the notional throat was kept at 0.8 as anchored according to experimentally validated CFD simulations [37]. The mean diameter of the engine is varied in increments of 0.25 inches from 2.0 to 14.0 inches. This was chosen based on the intuition that the largest annular gap and highest inlet manifold pressure will achieve relatively high, or comparable thrust, to that of a large diameter but lower pressure and reduced annular gap configuration. In other words, the thrust and thus mass flow rate will be mostly driven by the annular area which is driven by a combination of inlet manifold pressure, annular gap width and chamber diameter. The limits are set to capture low pressures with low annular gap widths (low mass flux) and high pressures with large annular gap widths (more mass flux).

Table 6.2: Summary of model input parameter sweeps utilized for RP-1 and O2 sea-level RDRE design of experiments study.

Parameter	Number of Points	Range Low	Range High	Increment
phi	10	0.90	1.80	0.10
P_man	5	700.00	1300.00	150.00
T_i	1	540.00	540.00	-
ht	21	0.58	0.98	0.02
AR_RDRE	9	2.00	6.00	0.50
art	1	0.80	0.80	-
arn	1	23.00	23.00	-
D_mean	49	2.00	14.00	0.25

In total, there were 463,050 cases simulated in this study. The summarized design of experiments parameter sweep ranges is provided in Tab. 6.2 A similar computational-time-required study was performed to estimate the time for this analysis. The CPU used for these studies is an AMD Ryzen 5950X 16-Core Processor with a 3.40 GHz clock speed. This time requirement study was done to help showcase the extremely rapid computational capabilities of this model. This code with the rapid compute time is a valuable asset to have for efficient system and mission trade study analysis.

6.1.3 Methodology

A MATLAB script was run in which the parallel processing library was utilized. The MATLAB parallel processing library enables the efficient allocation of computational

tasks withing a nested for loop. In this DoE analysis, there were five nested for loops. The parallel processing capability allows for each unique loop case to be computed by a determined processor. The `parfor` loop allows for iterations to run concurrently on different workers. The script purposefully opened an existing `csv` file, write data, closed that file, and began the next batch of computations. This was done to avoid losing any data in the case the computations stopped or something went wrong. To give insight into even larger studies, the net increase in computational time for a larger simulation batch was only 4.50% longer when opening, writing, and closing a file every 500 cases. The total computation run time for this 463,050 case RDRE parameter sweep was 6.77 hours. This further demonstrates the incredible utility of this model. Individual CFD cases for RDRE on standard desktops can take a comparable if not even longer period of time given the complexity of the flow fields coupled with highly dynamic reacting chemistry.

The data was saved to a final `csv` file that was then read using Python's Pandas library. Pandas enables rapid processing of datasets including filtering and selection based on criteria, analysis and plotting. The very first step was to clean the data of any cases where the effective length L_{eff} (roughly the measure of the length of the detonation front) was longer than the actual physical length of the engine as determined by the geometry parameters. This essentially disqualify any engine chambers that are physically shorter than the expected wave front height.

The Pandas dataframe containing all engine configurations was set to remove any data points where $L_{eff} > L_{\text{act}}$. This filter removed 47,020 engine configurations. The dataset was processed to visualize the distribution of thrust ranges produced in this design of experiments. Fig. 6.1 shows this distribution for thrust values. Clearly, with parameters having a wide range of values, it would make sense that certain combinations of high pressure, large annular gap and larger diameters result in this wide range of thrust values obtained from the DoE. The first bin indicates a large number of engines in the

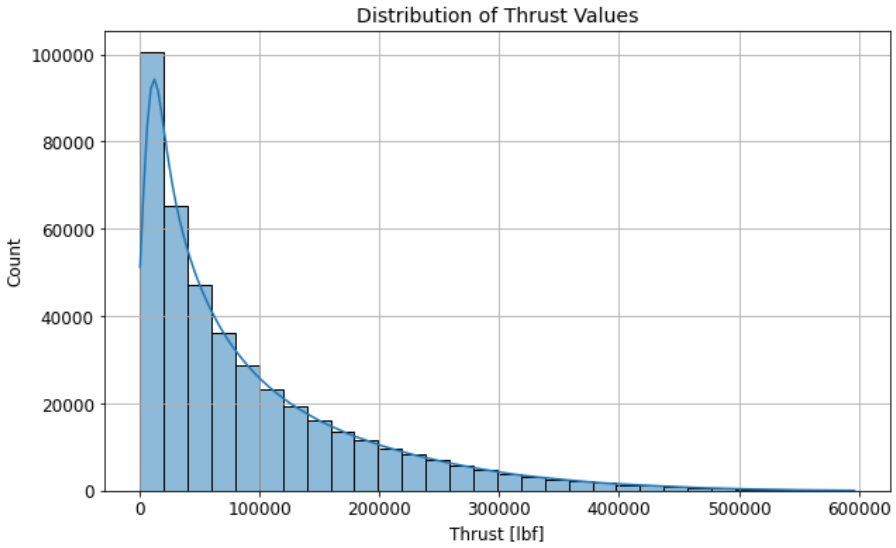

Figure 6.1: Distribution of predicted thrust values for the entire design of experiments for the RP-1/GOX engine modeled with the parameter ranges provided in Tab. 6.2.

0-10,000 lbf class range. From here, the number of parametric combinations producing increasing thrust configurations decays. Given the objective of this study is to converge on several optimal engine configurations in the 15k-16k lbf range, this provides a reasonably

large dataset from which further filtering and sorting can take place. The engines were also sorted to display the distribution of model predicted specific impulse for this large study. Fig. 6.2 shows a a long tail in the lower Isp limits followed by the majority of engines falling in the 280 to 310 seconds range. There is a steep fall off with the maximum just below 320 seconds. The maximum value for the entire data set was an engine producing 315.9 seconds Isp. For this configuration and parametric sweep, there are no engines that exceed this upper limit.

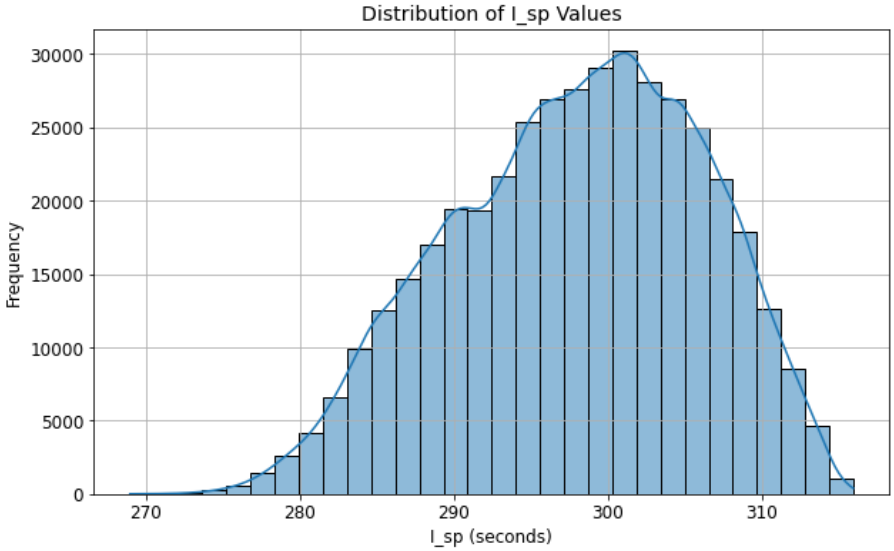

Figure 6.2: Distribution of specific impulse for all combinations of engines modeled in the design of experiment performed with the varied parameter ranges found in Tab. 6.2

6.2 Engine Optimization Discussion

6.2.1 Performance Requirements

The large engine dataset, and associated results, will inform RDRE design considerations and is the main focus of this section. The values chosen for these requirements listed below represent a hypothetical thrust class of interest along with other criteria denoted as hypothetical requirements. As will be shown in the following subsections, the top 15% of engines based on specific impulse performance are selected along with the top 25% of engines that require minimal cooling are further chosen. The optimal engine configurations and rational behind the final engine selection discussed in detail.

Configurations modeled in this DoE were filtered based on the following requirements set to maximize for efficiency and reduced load needed for the cooling system.

- Engine shall achieve 15k-16k lbf thrust.
- Engine shall have a specific impulse of at least 305.35 seconds.
- Engine shall not exceed a total heat load of 6186 BTU/s

6.2.2 Filtering for Optimal Engine Design Configurations

The following subsection outlines the distribution of engines within different design parameter and operational condition space. This provides an understanding of where engine configurations may reside and the frequency at which engines occur at the respective parameter and value.

The dataset was then filtered for engines the model estimates producing 15,000 lbf to 16,000 lbf of thrust. This left 4,798 total engine configurations. The distribution of specific impulses was once again plotted for this dataset filtered by the specified thrust requirement range. The 85th percentile for engine Isp was below 305.36 seconds. This value selected as the next filter. The dataset was further reduced by dropping all modeled engines producing less than 305.36 seconds, leaving the top 15% of engines by specific impulse performance. The resulting dataset contained 721 engines. The final filter applied was based on the value for total heat transferred to the combustion chamber walls. Engines that were estimated to transfer less than 6,186 BTU/s of total heat load to the engine walls were selected. This set of engines compromises the lowest 25% of engines based on cooling requirements. To summarize, the dataset was filtered by engines falling in the 15k to 16k lbf range from which the top 15% of engines by Isp and lastly, the top 25% of engines based on minimal cooling requirements are selected. The final dataset contains 180 unique engine configurations.

As seen in Fig. 6.4, the majority of 15k-16k lbf RP-1/GOX gas generator powered turbopump engines operating at inlet manifold pressures ranging from 700 psi to 1300 psi with varying equivalence and hub-to-tip ratios belong mostly in the 2.0 to 6.0 inch range. The engines filtered by Isp have a more pronounced leftward distribution with no engine combinations existing with larger than 7.5 inches in diameter. Based on previous parameter sweeps, this would be indicative of engines running at lower manifold pressures resulting in reduced specific impulse performance relative to smaller form-factor and higher pressure counterparts. Plotting the distribution of inlet manifold pressures across the three datasets confirms this. The model estimates there being a set of engines that meet these requirements on specific impulse and total heat transfer to the engine walls operating around the 850 psi range. Taking a more granular view between 700 and 850 psi would be beneficial to examine even further.

As expected, there are more engines that meet the final criteria at larger pressures due to increased efficiency. The cooling system limit threshold set to 6186 BTU/s is expected be largely dictated by the size of the engine. If there is more surface area for hot gas to transfer energy to the walls of the chamber, the total heat load will increase. Furthermore, given this sweep also varied the aspect ratio of the engine, it provides insight into performance of potential engines with aspect ratios lower than five times the hydraulic diameter of the inner chamber as cited by Paxson in the comments of the code [65].

As RDRE technology development continues, it may be possible that these engines can indeed operate at these lower length to hydraulic diameter ratios. When the model is run using lower values for AR_{RDRE}, the reduced length of the engine therefore drives a lower heat transfer value given the resulting total surface area is reduced. This behavior is confirmed when plotting the distribution of actual engine lengths as determined by the model based upon the aspect area ratio parameter.

Given the engines are being selected based on their specific impulse and reduced cooling requirements relative to the overall dataset, it is expected that most of these

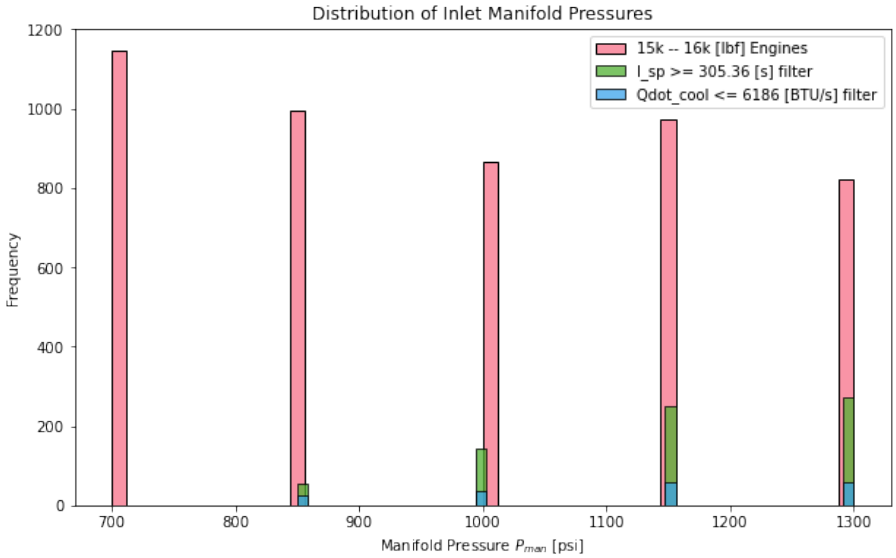

Figure 6.3: Distribution of inlet manifold pressures 15k-16k lbf thrust range. Sequential filters are shown on design of experiment multi-dimensional parameter sweep dataset.

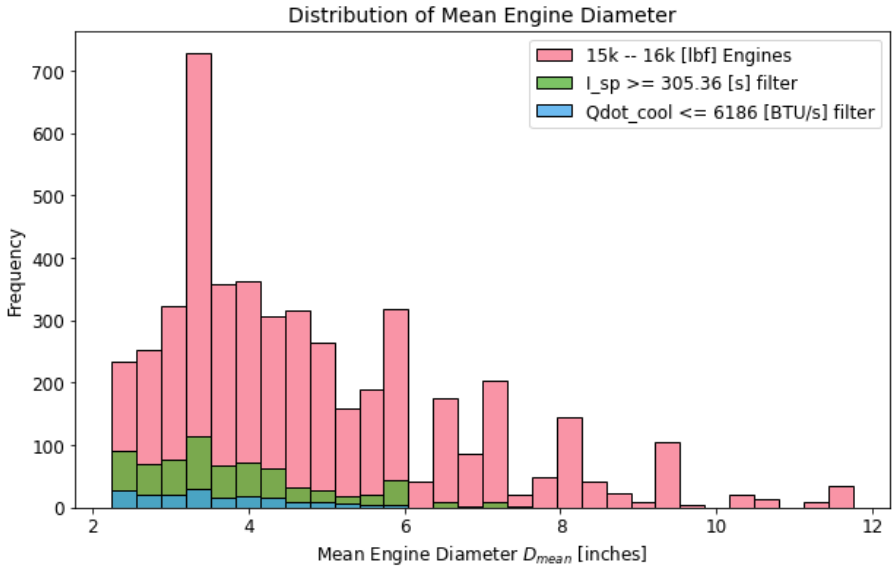

Figure 6.4: Distribution of mean engine diameter [inches] for 15k-16k lbf thrust range. Sequential filters are shown on design of experiment multi-dimensional parameter sweep dataset.

engines should reside in the lower operational mass flow rate range. This trend can be seen in Fig. 6.6 with the distributions of filtered engines residing at, or below the 52 lbm/s mass flow rate range. Note this includes the required flow rate of the propellant entering the gas generator cycle.

For these design sets, all engines operate with a gas generator with an operating pressure of 1500 psi and an equivalence ratio of $\phi_{gg} = 7$ also utilizing the RP-1 fuel. The mixture is run fuel rich to ensure lower temperatures in the gas generator [65]. This model provides further value as these submodels can be expanded upon or updated to match systems with known performance available today. This model enables the investigation of turbopump subsystem tuning on performance effects on the overall propulsion system.

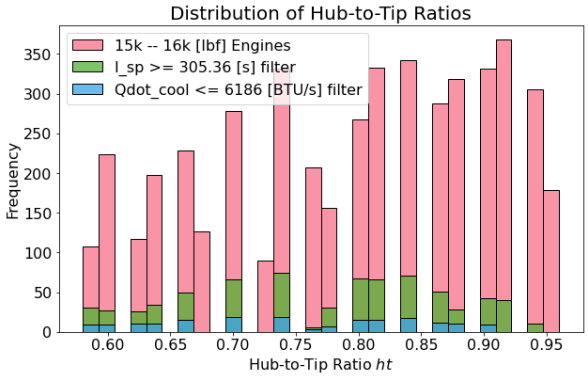

(a) Distribution of Hub-to-Tip Ratios

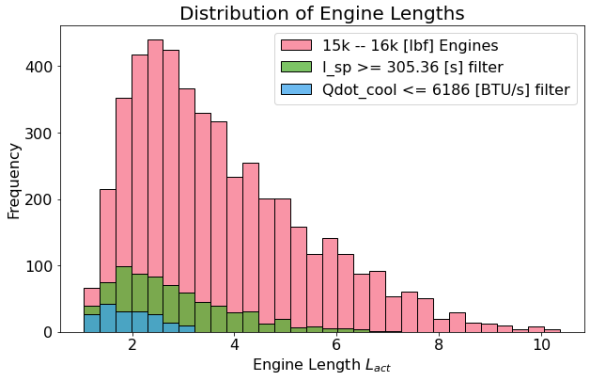

(b) Distribution of Engine Lengths

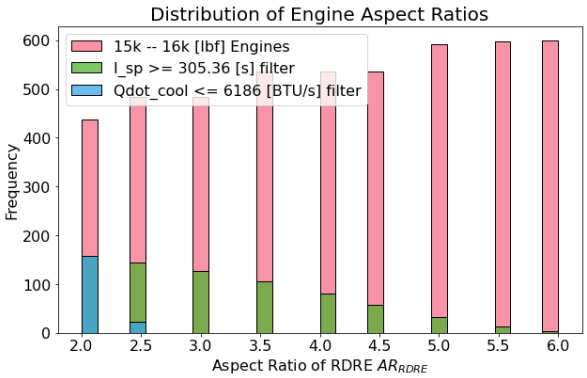

(c) Distribution of Engine Aspect Ratios

Figure 6.5: Distribution of Engine Parameters

The open cycle is less efficient than closed cycle/ staged combustion cycles such as those used on the SpaceX Raptor full flow staged combustion cycle engine [74]. In these cycles, the usually fuel rich mixture enters the first combustion chamber, which generates the hot gas to drive turbines and associated pumps to increase flow rate. This hot gas then gets fed into the main combustion chamber.

To recall, the present model assumes the open cycle variant where the combusted gas in the generator does not contribute to the overall thrust of the system. This penalizes the overall efficiency as measured by the Isp of the system. The modeling and potential utilization of denotative propulsion may also be interesting for the purpose of driving an even more efficient gas generator cycle. There may be a way to design the pre-burner to utilize pressure gain detonative propulsion. Turbines driven by detonated gas may offer further increased efficiency relative to deflagration based gas generators.

However, the actual length of the engine is computed using the value for AR_{RDRE}. This value multiplied by the hydraulic diameter of the engine provides the total length. The hydraulic diameter in this case is two times the annular gap. Thus, for lower values of ht, the annular gap increases, increasing the hydraulic diameter and increasing the length for a set diameter. This behavior can be more easily visualized in three dimensional space. For example, an aspect ratio of 5, with a diameter of 3 inches and a hub-to-tip ratio of 0.6 results in a annular gap of 0.75 inches with an actual length $L_{\text{act}} = 5 \cdot 2 \cdot 0.75 = 7.5$ inches.

Plotting the data in three dimensions while holding two input parameters constant generates unique surfaces for one varied parameter. By generating a surface for each

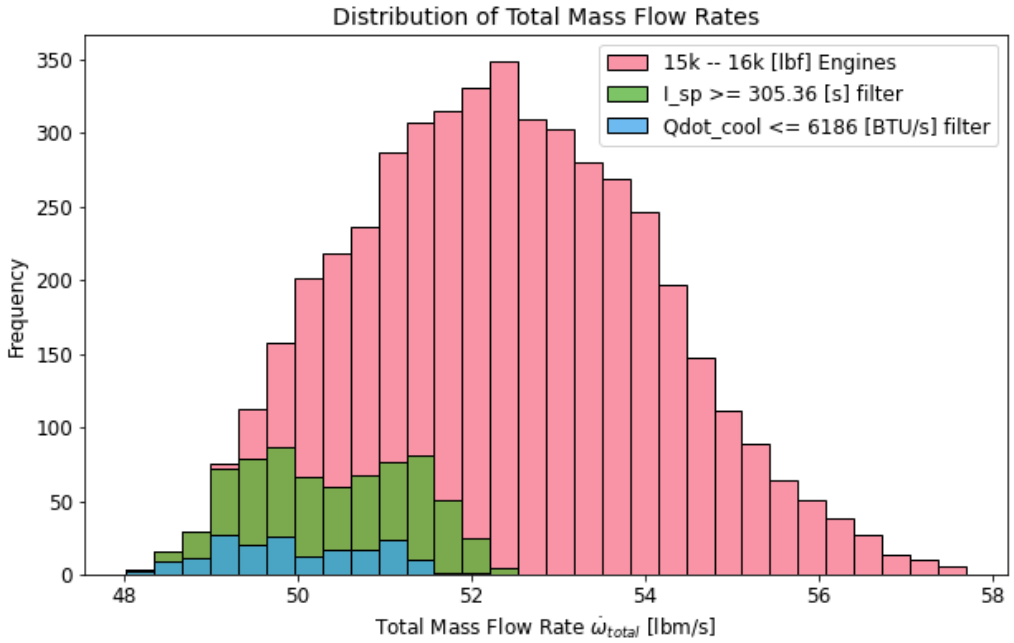

Figure 6.6: Distribution of total engine mass flow rates in [lbm/s] for the 15k-16k lbf thrust range engine selection. Sequential filters are shown on design of experiment multi-dimensional parameter sweep dataset.

unique value of AR_{RDRE}, every point in the surface represents one unique engine configuration at a fixed operating condition for pressure and equivalence ratio. The behavior of the actual engine length is plotted along the z-axis with the mean diameter and hub-to-tip ratios being varied. As seen in Fig.6.7, a 4th dimensional parameter may be added by applying a color encoding to the thrust value of each point along the surface. The grid is generated with a resolution of 100 points the x, y, and z directions. The values interpolated across the grid.

6.2.3 Multi-Dimensional Parametric Analysis

The case plotted in Fig.6.7 represents a multidimensional visualization of rocket engine configurations filtered for all combinations that produce thrust in the 15k-16k lbf range. For example, this particular plot rapidly provides insight into which design parameters drive slightly higher thrust in this thrust range requirement. There are regions of yellow at higher engine diameters at reduced hub-to-tip ratios. These engines are shorter relative to the rest of the configurations in this dataset. There is also regions on each surface (each unique aspect ratio) for smaller diameters yet increased ht. The resulting length of the engine also provides good insight into sizing requirements. As each individual aspect ratio value generates a unique surface, the performance of a particular engine can be analyzed in further detail. A higher aspect ratio results in a longer engine for the same combination of a ht and D_{mean}

Out of the five parameters (Tab.6.2) being varied in this study, two are chosen here to represent the x-axis and y-axis of the 3D surface plot. Each value of ht and D_{mean} produces an engine length for a given aspect ratio AR_{RDRE}. Thus, a unique surface is plotted for each value of the aspect ratio. This parameter drives length. This can be seen as the surface layers higher along the z-axis result in longer lengths for matching

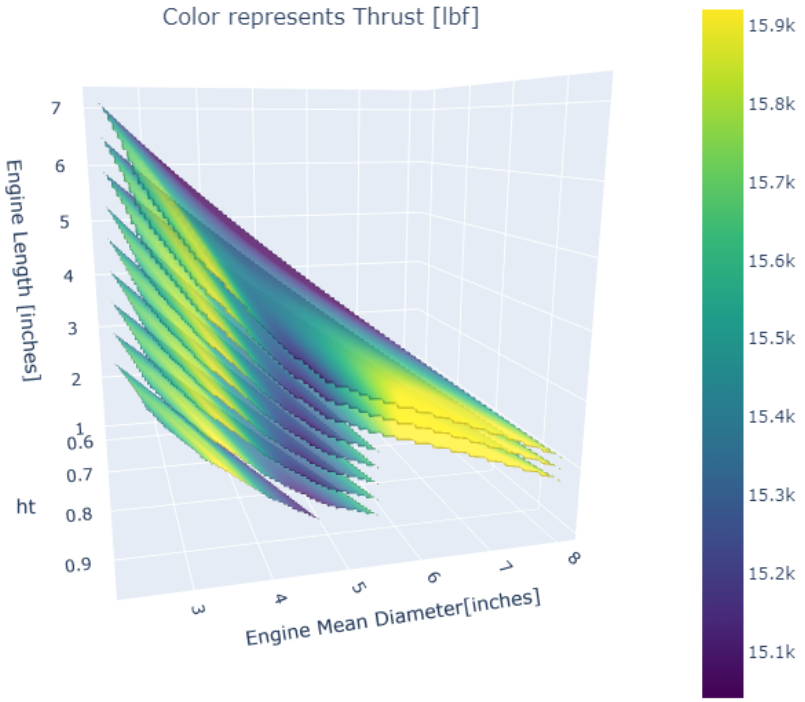

Figure 6.7: 3D visualization of engine length due to varied geometry parameters: ht and D_{mean}. Each surface delineates an aspect ratio AR_{RDRE}. The color encodes the value of thrust for that configuration at a fixed pressure ($P_{man} = 1300$ psi) and equivalence ratio ($\phi = 1.2$).

geometry inputs for ht and D_{mean}.

In order to visualize the value for fourth dimension such as thrust or specific impulse in this design space, there needs to be two more parameters held fixed. Hence, the inlet manifold pressure and equivalence ratio are held fixed. This enables one unique engine along each surface of AR_{RDRE} with a corresponding performance parameter. The plotting function was made using the Plotly package. This enabled rapid visualization for any series of inputs. The function takes in the parameter for each axis of the plot, the color of the surface, and unique surface delineation parameter. This process helped rapidly produce multi-dimensional visualizations to qualitatively assess affects of multiple parameters on engine sizing and performance. Another similar plot was made using the same process of carefully selecting varied and fixed parameters to ensure plotting of individual engine configurations and their respective performance outputs along a surface. Fig.6.7 shows the specific impulse performance across different aspect ratios for engines operating with the same pressure and equivalence ratio as mentioned earlier. The specific impulse is seen to steadily increase with decreasing aspect ratio given the reduced total surface area and thus reduced chemical energy losses to the walls of the combustion chamber. The parameter stored in the output section by the model representing the

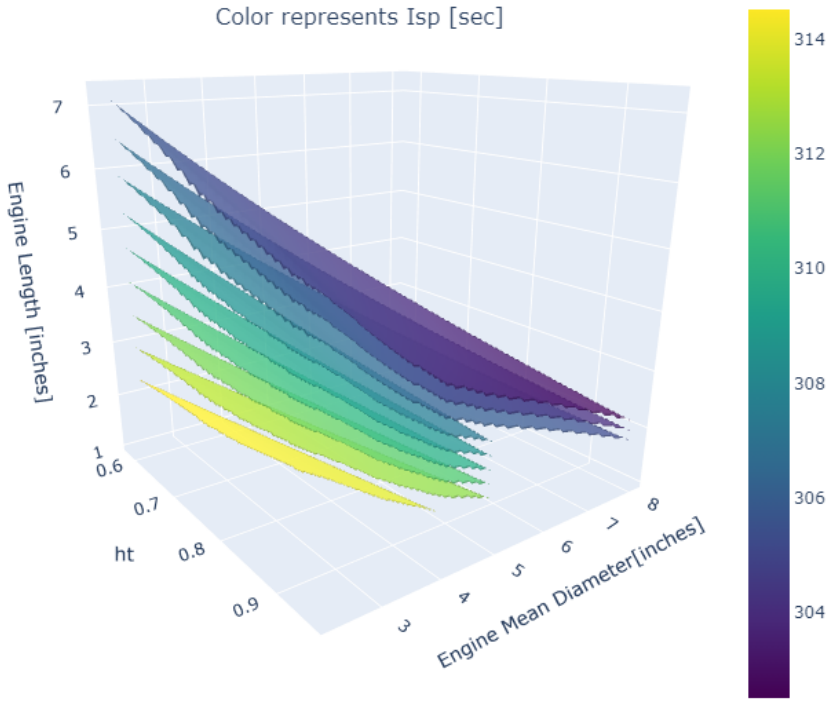

Figure 6.8: 3D visualization of engine length due to varied geometry parameters: ht and D_{mean}. Each surface delineates an aspect ratio AR_{RDRE}. The color encodes the value of specific impulse for that configuration at a fixed pressure ($P_{man} = 1300$ psi) and equivalence ratio ($\phi = 1.2$).

fraction of chemical energy lost to the walls of the combustion chamber ($qfrac_{wall}$) is then plotted to confirm this trend. As seen in Fig.6.9, the engines with the lowest aspect ratios only lose about 3% of their chemical energy to the walls. The engines designed with the upper bound for the aspect ratio losing almost 10%. This helps visualize the potential losses of different systems operating under the same conditions.

Another interesting parameter to note is the specific impulse increase for the RDRE compared to a basic rocket engine with identical inlet conditions. The author of the code [65] mentions the specific impulse of the basic rocket is computed using the same gas generator conditions and equal combustion efficiency (this design of experiments held this value at 0.97). The code models the idealized basic rocket (basic referring to a standard deflagration based rocket chamber) and compares the resulting specific impulse performance with the value obtained with the RDRE. This value can help provide preliminary estimates when performing design optimization when replacing deflagration based rocket engines.

The basic rocket is modeled using the ideal gas law with isentropic flow and a constant specific heat ratio as computed by CEA for this mixture and pressure. The basic rocket model takes into account over and under expanded flow in the nozzle. The code

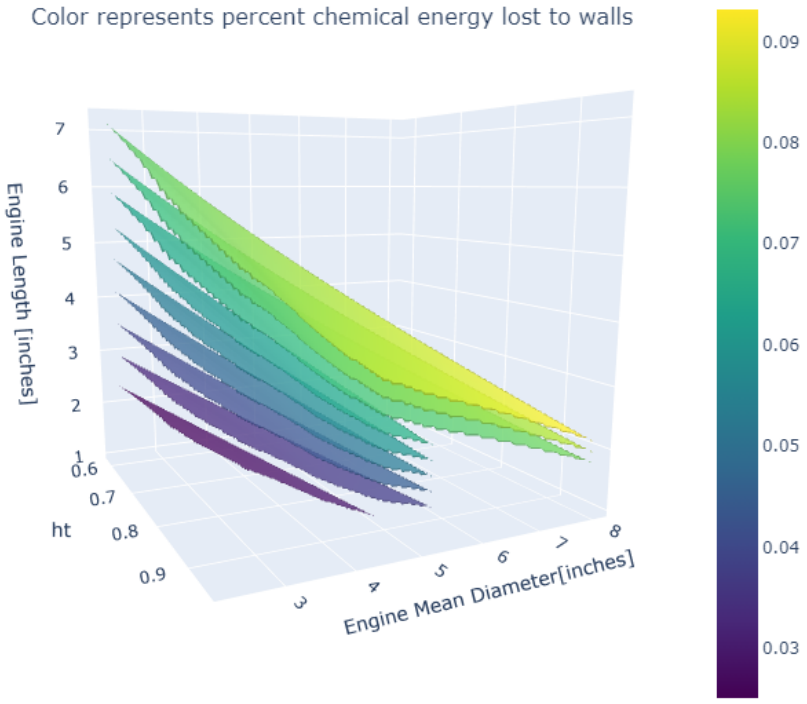

Figure 6.9: 3D visualization of engine length due to varied geometry parameters: ht and D_{mean}. Each surface delineates an aspect ratio AR_{RDRE}. The color encodes the value of the fraction of chemical energy lost to the walls for that configuration at a fixed pressure ($P_{man} = 1300$ psi) and equivalence ratio ($\phi = 1.2$).

solves for the the ideal exit velocity using known parameters and from the RDRE computations and computes an ideal exit velocity. Using this ideal exit velocity, it computes the Isp of the engine. A 2D heat-map was used to visualize the relative Isp gain of a system operating at a manifold pressure (P_{man}) of 1300 psi and an equivalence ratio (phi) of 1.2. The fuel is RP-1. The specific impulse gain of engines mapped in the hub-to-tip ratio and mean diameter space. The fixed value for aspect ratio is set fixed. It can be seen the specific impulse improvement over an idealized basic rocket as modeled in the code is shown to be over 22 seconds higher for high diameter and low hub-to-tip ratio engines. Note the dataset fed into this image is for the entire design of experiments. To recall from Fig.6.1, these are likely engines in the high hundred thousand pound thrust class. This result is interesting nevertheless. The study done utilizing this simplified RDRE and standard rocket engine may suggest that detonation based propulsion scales its efficiency for higher thrust systems.

The 15-16k lbf engine subset was then plotted (Fig. 6.11 using the same conditions set to produce the plot seen in Fig.6.10. The cells with color denote that there exists an engine at this point in ht and D_{mean} space at the operating condition of 1300 psi, and an equivalence ratio of 1.2. It is interesting to see where these specific RDREs exist in

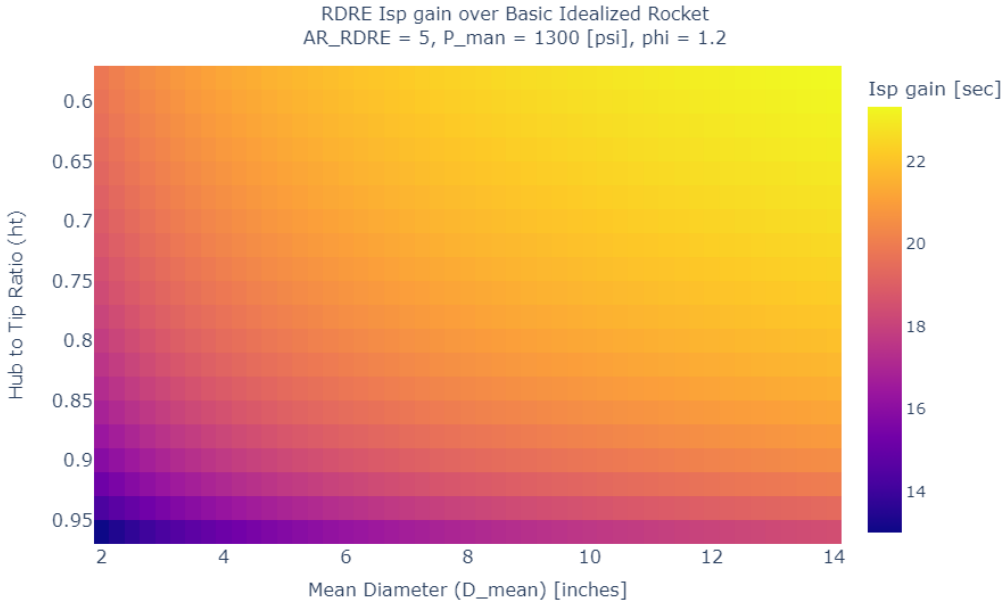

Figure 6.10: Heat map denoting the gain in specific impulse of an RDRE in ht and D_{mean} 2D space relative to an idealized basic rocket at identical operating conditions. The aspect ratio of the engine is fixed at 5. $P_{man} = 1300$ and $\phi = 1.2$. This data spans all possible thrust ranges. No specified thrust range was filtered.

the design space. The plot shows the model predicted specific impulse increase relative to existing (idealized basic rocket system). When using this as the performance metric, the winning candidates exist in the upper left hand corner of the plot. Thus, these trends currently suggest, when choosing a specified thrust class, the engines with smaller diameters and decreased hub-to-tip ratio will provide better gains in specific impulse relative to higher diameter but reduced hub-to-tip ratio RDREs. These are the same data trends visualized through the 3D surface plots, however, the data is down selected for a required aspect ratio and presented in an easier to navigate 2D plot. However, although the engines in the upper left hand corner of this map produce higher gains in specific impulse, the engine lengths are also longer.

This presents an important trade as the system mass will be highly sensitive to both diameter and length. The authors of the model plan to implement some mass properties model. This can also be confirmed through the design of two systems on either end of this map, and compare the estimated mass properties in CAD utilizing known materials from literature. Knowing mass property behavior will give a more realistic definition to what is considered optimal. It could be possible that RDREs provide advantages such as the capability to install larger diameter yet reduced length form factors. This could enable the relocation of other subsystems closer to the engine core itself. For example, a long yet narrow design would result in turbomachinery being housed to the sides or typically on top of the engine. If there is room on the airframe to utilize the full diameter of say a rocket or missile-like airframe, then critical components may be shifted closer and centered within the inner diameter annulus. In other words, more compact housing of propulsion systems and subsystems may offer improved vehicle system and mission performance. A qualitative trade study will show that reducing the length and mass of

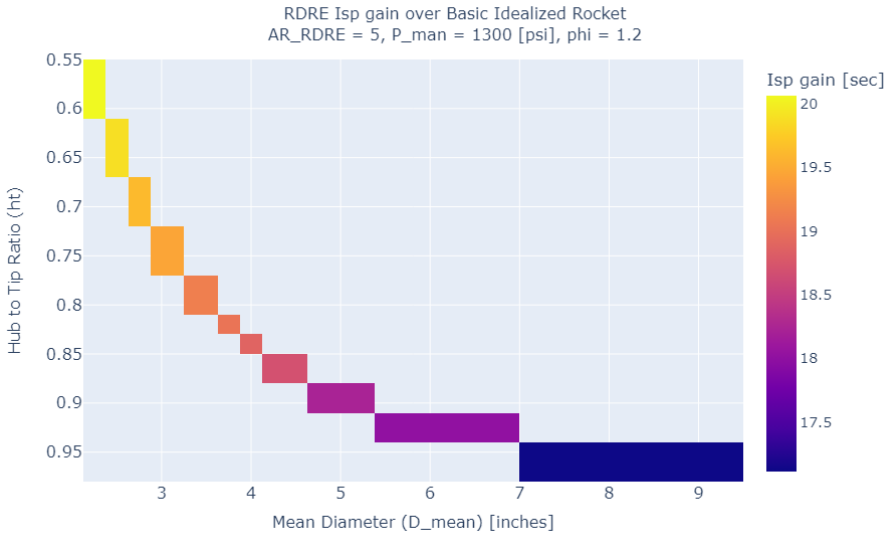

Figure 6.11: Heat map as provided in Fig.6.10 filtered for all engine configurations at selected operating conditions filtered for 15-16k lbf class engines.

the propulsion system will move the C_g of a rocket or missile like airframe forward.

In turn, this will increase the stability margin of the vehicle. As the baseline vehicle airframe has yet to be changed, one way to regain the stability margin of the original system would be to reduce the length or decrease passive stability control surface area. Given the RDRE also provides improved specific impulse, the vehicle will require reduced propellant storage requirements to produce the same thrust for an equivalent duration. This reduced propellant requirement can enable the reduction in length of the vehicle airframe reducing the overall system weight and size or allowing more payload mass and volume. The exact mass and sizing trade studies need to be analyzed in further detail. These preliminary values do provide a step in this direction with conceptual and preliminary design level analysis. Further discussion will take place in another section.

Two thrust classes are then compared by plotting all engines that produce an estimated thrust of 15-16k lbf and 100-102k lbf. Two families of engines are plotted in the 2D design space holding inlet manifold pressure, equivalence ratio and aspect ratio fixed. Fig.6.12 shows the 15k lbf class and the 100k lbf class with individual color bars. Each colored cell represents linearly interpolated values of Isp gain from unique combinations of mean diameter (D_{mean}) and hub-to-tip ratio (ht).

The parameter AR_{RDRE} is fixed at 5, with manifold pressure (P_{man}) at 700 psi and equivalence ratio (ϕ) at 1.2. The color bars on the right indicate the percentage increase in Isp, providing a clear comparison of performance enhancements across the two thrust classes within the parameter space. The trends seen are as expected. The large thrust class engine family curve has been transposed rightward along the mean diameter axis and up along the ht axis, denoting decreasing hub-to-tip ratio values. These decreasing values increase gap width at fixed diameter. The family of engines in the 100-102k lbf class produce a net increase in predicted specific impulse of about 10%. Note, this is a very simplified approach to comparing these engines. The idealized rocket engine does not factor into account many entropy generating mechanisms. Furthermore, it most likely provides an over estimate to the actual Isp of a standard rocket system. The Isp of

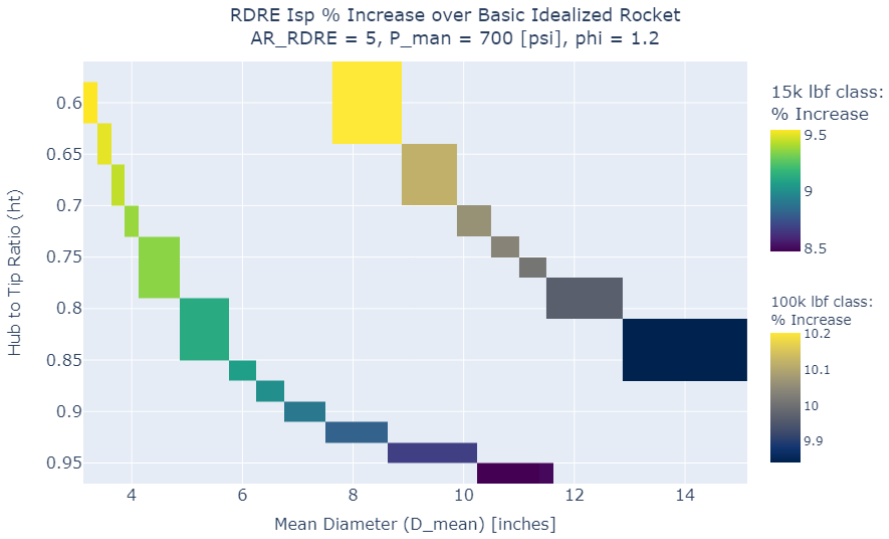

Figure 6.12: Heatmap with color denoting percentage increase in specific impulse for RDRE at the design space coordinate. Test cases conditions: P_{man} = 700 psi and ϕ = 1.2. for RDRE's segmented by thrust class compared to a baseline idealized rocket under equivalent operating conditions: P_{man} = 700 psi and ϕ = 1.2. RDREs with an aspect ratio of 5 are selected.

an known RP-1/Oxygen rocket engine system and the predicted specific impulse of the idealized basic rocket modeled in this code can be compared to provide a good reference frame for interpreting these values.

6.2.4 Comparison to Existing Deflagration Engine

The key parameters set for the input of the model are provided in Tab. 6.3. The data for the Merlin 1D engine was taken from a NASA Space Launch Report [75] published in 2017. As expected, the idealized calculations provide an over estimate on specific impulse performance for the given operating pressure and equivalence ratio. The model also provides a calculation for the ideal optimal expansion area ratio for a given ambient pressure. It is interesting to note that the actual expansion area ratio the Merlin 1D uses is slightly higher than this optimal value. This is in part due to optimization of the nozzle for the first stage trajectory where ambient pressures will decrease with increasing altitude. The larger area ratio may provide optimal performance across the first stage flight envelope.

These test cases provide insight into the even further potential efficiency gains of RDREs as the idealized deflagration rocket calculations are already providing an over estimate on the actual performance. The combustion efficiency input parameter is used in the idealized rocket specific impulse calculation was then lowered until the resulting performance matched. The value for the combustion efficiency was lowered to 0.88. This information was then used to calculate a new value for the idealized specific impulse of the basic rocket engine. These values were again compared as done in Fig.6.12. The only step here was to obtain a new value for the basic rocket engine specific impulse from the MATLAB GUI application. The inputs were set to match those used for the

Table 6.3: Merlin 1D engine test data [75] compared to idealized basic rocket calculations performed by the code [65].

SpaceX Falcon-9 (v1.1) - Merlin 1D Test Data 2011	
Engine Type	Gas Generator
Propellant Feed System	Turbopump
Operating Pressure	1410 psi
Equivalence Ratio (approximately)	1.45
Oxidizer	LOX
Fuel	RP-1
Specific Impulse (Sea Level)	282 sec
Specific Impulse (Vacuum)	311 sec
Actual Exit Area Ratio	16
Model Inputs	
Turbine Efficiency (η_t)	0.6
Pump Efficiency (η_p)	0.9
Turbine Pressure Ratio PR_t	3
Manifold Temperature	540 °R
Manifold Pressure P_man	1410 psi
Injector Loss v_loss	1
Exit Area Ratio	16
CEA computed value for γ	1.175
Idealized Basic Rocket - Computed Model Results	
Test 1: Combustion Efficiency Parameter (η_c)	0.97
Specific Impulse (Sea Level)	296.12 sec
Specific Impulse (Vacuum)	325.64 sec
Test 2: Combustion Efficiency Parameter (η_c)	0.88
Specific Impulse (Sea Level)	282.86 sec
Specific Impulse (Vacuum)	311.06 sec
Computed Ideal Exit Area Ratio (Sea Level)	12.6

fixed parameter values: $P_{man} = 700psi$, and $\phi = 1.2$. The model uses the idealized exit area ratio, which is different than the exit area ratio used to compute the performance of the RDRE. In other words, this data may suggest an under estimate in actualized gains for comparable systems. The updated specific impulse of the idealized basic rocket was computed to be 259.83 seconds for the conditions specified earlier. This value was then used to update the calculation for the percentage increase in specific impulse of the RDRE. The data for two aspect ratio cases is visualized below in Fig. 6.13. Recall the engine length is reduced when using a relative lower value for AR_{RDRE}. For the assumed engine design using an aspect ratio of five, the model predicts over 14.5% and 15.3% increase in specific impulse for both thrust classes respectively. This is measured relative to results obtained in computing the performance of the ideal basic rocket with η_c now set to 0.88. Note, the RDRE dataset was gathered using $\eta_c = 0.97$ as provided in Tab.6.2.

Reviewing the data shows an additional 2.51% performance increase for the RDRE after tuning the combustion efficiency parameter for the basic rocket computations from 97% to 88% to reflect the previously determined calibration value. The predicted results from the model provide insight into the relatively significant gains that may be realized for RDREs. It is further important to note the improved performance at relatively lower

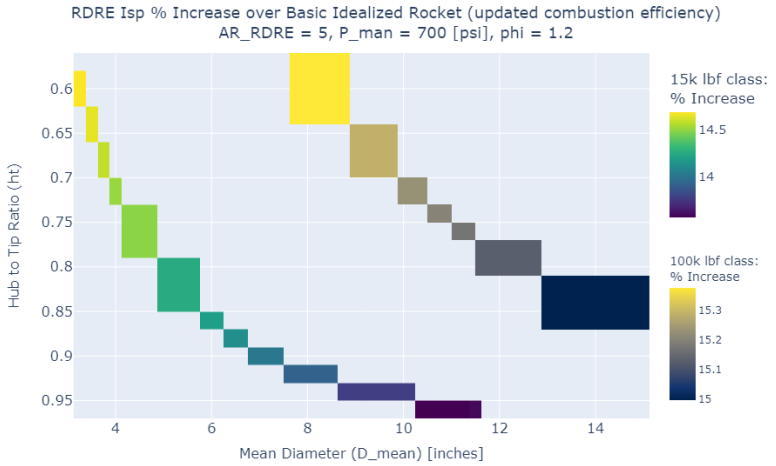

(a) RDREs with an aspect ratio of 5.

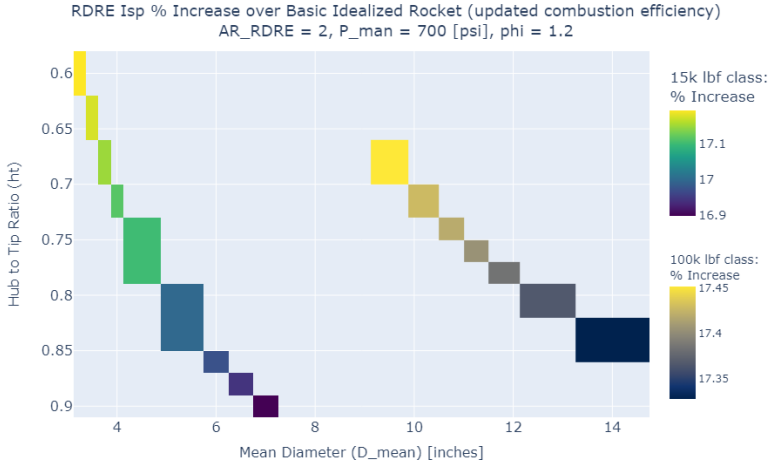

(b) RDREs with an aspect ratio of 2.

Figure 6.13: Heatmap with updated combustion efficiency ($\eta_c = 0.88$) used to compute reference Isp for idealized basic rocket. RDRE's segmented by thrust class. Color denotes percentage increase in specific impulse for RDRE at the design space coordinate. Test cases conditions: $P_{man} = 700$ psi and $\phi = 1.2$.

operating pressures. This will reduce weight and eventual manufacturing cost due to lower pressure requirements on the propellant feed system and other associated propulsion subsystems.

6.2.5 Delta-V Improvements with RDRE

Known trends in Isp performance for an RP-1/OX open cycle gas generator turbopump propellant fed RDRE enables conceptual level analysis on the ΔV and mass fraction performance increase of a rocket system. The Tsiolkovsky rocket (ideal rocket equation) equation below can be used to estimate the mass fractions and ΔV of an idealized rocket

system with no drag or gravity losses.

$$\Delta V = I_{\text{sp}}\ g_0\ ln(\text{MR}) \tag{6.1}$$

ΔV is the maximum change in the vehicle velocity with no other external forces acting on the system. MR is the mass ratio or sometimes called mass fraction. MR is defined as:

$$\text{MR} = \frac{m_0}{m_{\text{f}}} \tag{6.2}$$

Where m_0 is the initial total mass and m_f is the final total mass of the system (structure and payload). Clearly, increasing the Isp of the rocket system will increase the maximum change in velocity. If the vehicle is required to achieve a set delta-V, then the required mass fraction can be slightly smaller. This means either less propellant is required or a larger final mass can be taken to the necessary velocity.

As an example, an orbital maneuvering vehicle (OMV) is tasked with transferring an asset from a 185 km to 20,000 km orbit via a Hohmann transfer with no plane change. The required delta-V budget for this in-space mission is 3.5 km/s [76]. Assuming the original Isp of an engine was 345 seconds and the new Isp is 370 seconds, the required mass ratio necessary to achieve the required maneuver would decrease from 2.816 to 2.625. This can be significant in terms of the fuel budget or the ability to deliver more payload with the same starting propellant and structural mass. Rearranging Eqn .6.1 leads to an expression for the final mass at maneuver completion. Solving for m_{f} gives:

$$m_{\text{f}} = \frac{m_0}{e^{\frac{\Delta V}{I_{\text{sp}}\ g_0}}} \tag{6.3}$$

Where m_f can further be expressed as:

$$m_{\text{f}} = m_{\text{structure}} + m_{\text{payload}} \tag{6.4}$$

Where the initial mass is the final mass in addition to the starting propellant mass. To demonstrate the significance of this Isp increase, a hypothetical system is briefly analyzed.

Assuming the mission constraint is placed on the initial mass of the entire system due to launch vehicle capacity, the increase in payload mass can be determined for a given constant vehicle structural mass. For this example case, the improved engine design provides a 7.25% increase in specific impulse. Moreover, this does not take into account any potential weight savings this improved RDRE replacement would have over the deflagration engine. As such, further gains could be realized through detailed engine and system level design optimization and analysis.

Several assumptions were made to obtain the values provided in Tab. 6.4. The structural mass was assumed constant for all three cases. The propulsive burn is assumed to be uniform in performance and ideal through its entire mission. This conceptual level mission analysis of an OMV suggests the replacement of its vacuum optimized RP-1/O_2 deflagration power unit can improve payload capacity by 56.02%. The net Isp increase percentage was taken from the analysis provided in the previous sub-section where the increase was measured relative to the idealized performance calculations. The upper limit of the plot in Fig.6.13b is approximately 17.45% increase relative to idealized calculations for a basic rocket. The idealized performance calculations of the deflagration engine were calibrated through adjusting the combustion efficiency until the performance matched a known system, in this case the Merlin 1-D.

Table 6.4: Idealized rocket equation delta-V analysis and comparison to deflagration powered system.

Mission Constants		
Parameter	**Value**	**Units**
Delta V	3,500	m/s
Initial Mass	10,000	kg
Structural Mass	2,500	kg
Deflagration Engine: Isp = 345 sec		
Final Mass	3,555	kg
Payload Mass	1,055	kg
RDRE Case 1: Isp = 370 sec		
Net Isp Increase	7.25%	-
Final Mass	3,813	kg
Payload Mass	1,318	kg
Net Payload Mass Increase	263	kg
Net Payload Increase	24.89%	-
Optimized RDRE: Isp = 405.20 sec		
Net Isp Increase	17.45%	-
Final Mass	4,146	kg
Payload Mass	1,646	kg
Net Payload Mass Increase	591	kg
Net Payload Increase	56.02%	-

6.3 Final Selection of 15-16k lbf engines from DoE

The engine configurations modeled in this DoE were filtered based on requirements set to maximize for efficiency and reduced load needed for the cooling system.

- Engine shall achieve 15k-16k lbf thrust.
- Engine shall have a minimum specific impulse of 305.35 seconds at peak thrust.
- Engine shall not exceed a total heat load of 6186 BTU/s.

As seen in Fig. 6.3, there is a small set of engines in the 850 psi inlet manifold operating range. This is the minimum operating pressure that provides the necessary performance metrics. These sets of engines were determined to be the favorable choice given the inlet manifold pressure is sufficient to provide necessary performance without penalizing the system with higher pump feed system capability requirements. The lower inlet manifold pressures out of all engines in this thrust class may provide reduced cost and weight and increased reliability. The operating inlet manifold temperature and engine wall temperature were held fixed for all simulation cases. The fixed parameters and selected operating conditions are summarized in Tab. 6.5. The data was then sorted by specific impulse with the maximum value in the first row. The corresponding engine performance is summarized in Tab. 6.7.

An interesting takeaway is that engine ID 45913 has the highest resulting Isp in this dataset and lowest total heat load on the walls of the combustion chamber and lowest mass flow rate. The engine also has the smallest diameter at 3.0 inches and smallest

Table 6.5: Parameters held fixed in final engine set selection for the 15k-16k lbf thrust class.

Parameter	Value
P_{man}	850 psi
ϕ	1.2
T_i	540 °R
T_{wall}	2400 °R
Exit Area Ratio (arn)	23

Table 6.6: Resulting engine sizing and design parameters for RDREs matching performance requirements and selected to operate at a $\phi = 1.2$ and $P_{man} = 850$ psi. The resulting engine annulus inner and outer diameter are tabulated under the column names ID and OD respectively.

Engine ID	D_{mean} [inches]	ht	L_{act} [inches]	AR_{RDRE}	ID [in]	OD [in]
45913	3.00	0.62	2.815	2.00	1.860	3.704
90463	3.25	0.66	2.663	2.00	2.145	3.916
135013	3.50	0.70	2.471	2.00	2.450	4.118
179563	3.75	0.74	2.241	2.00	2.775	4.310
202063	4.00	0.76	2.182	2.00	3.040	4.545
292063	5.00	0.84	1.739	2.00	4.200	5.435
314563	5.25	0.86	1.581	2.00	4.515	5.645
337513	5.75	0.88	1.468	2.00	5.060	6.117

hub-to-tip ratio of 0.62 out of the final eight engines. Given the filter criteria across all engine combinations was based on a maximum heat transfer to the walls, all final 8 engines have an AR_{RDRE} of 2. This parameter drives the resulting engine length. The study assumes a value of 2 for this parameter is feasible for RDREs.

To recall, all engines that had an actual length less than that of the predicted wave front height were removed from the original dataset. This engine also had the lowest percent chemical energy loss to the walls of only 2.63% as values were not tabulated here. Furthermore, due to the low *ht* compared to the other seven engines, this engine has the longest resulting length for the combustion chamber. This could be an important factor when deciding on the optimal engine configuration in this hypothetical engine design exercise.

The final set of eight engine configurations presents an interesting opportunity to explore some qualitative trades. Given these engines all fall in the same required thrust class, engines can be chosen based on maximized fuel efficiency or best form factor. The trends show that although engine with the ID 45913 has the highest specific impulse, it is the the longest engine out of the set. However, it still produces more thrust than engine ID 314563 for example. Engine 202063 produces the highest thrust out of the final set with the model predicting a value of 15,836.55 lbf. This engine has a 33.33% larger diameter at an additional inch over engine 45913. This trade of increased thrust but also additional sizing requirements would have to be further investigated. For example,

Table 6.7: Performance parameters for the final top eight filtered 15k-16k lbf engines that meet performance requirements and are operating at 850 psi inlet pressure with an equivalence ratio of 1.2. Engines are summarized based on decreasing specific impulse (Isp).

Engine ID	Thrust [lbf]	Isp [sec]	Isp gain [sec]	$\dot{\omega}_2$ [lbm/s]	$\dot{Q}_{cool}$[BTU/s]
45913	15321.37	308.48	30.86	49.71	5,028.95
90463	15694.50	308.42	30.80	50.94	5,218.92
135013	15689.17	308.36	30.74	50.93	5,298.58
179563	15255.57	308.27	30.65	49.53	5,257.40
202063	15836.55	308.24	30.62	51.42	5,489.22
292063	15774.85	308.01	30.39	51.26	5,737.77
314563	15059.34	307.92	30.30	48.95	5,586.46
337513	15321.32	307.85	30.23	49.81	5,771.08

understanding the mass increase due to this increased diameter would have to be modeled or designed in CAD with accurate mass properties. However, the model returns a slightly lower overall engine length compared to engine 45913.

For a given set of hypothetical RDRE design requirements calling for maximized Isp performance and minimized cooling, the final engine design would be engine ID No.45913. However, due to the reduced sizing relative to all other engines, it could be possible that the reduced space available to integrate cooling channels into the combustion chamber may disqualify this engine.

Chapter 7: Conclusions and Recommendations for Further Research

7.1 Conclusion

The summary of research along with the design and analysis of a potentially optimized RDRE system has been presented in this report. The report provides important insights into a rapidly evolving and maturing technology posed to usher in a next generation of rocket propulsion systems. Foundational topics critical to detonation theory are first discussed along with governing equations and key assumptions. Discussions are made on how theory compares to experimentally measured data obtained on detonation wave physics and engine testing. Pulsed and revolving detonation waves compromise the two forms of propulsion introduced in this report with the main focus on the methodologies taken to produce combustion through revolving the self propagating detonation waves within an annular chamber.

The report discusses computational simulation and modeling along with comparison to experimentally measured results. Computational modeling has been shown to provide good alignment with experimental measurements and enables the analysis of critical detonation physics and complex non-linear phenomena in these flow fields. High performance computing and massive strides in simulation capabilities have provided critical insight into many phenomena not possible to observe through experiment. These insights improve design considerations and performance evaluation of RDRE systems.

Moreover, the recent surge in experimental hot fire testing and sustained and stable operation has provided critical milestones in advancing the technology readiness level of RDRE systems. Experimental data has also enabled validation of simulations providing the ability to develop performance and sizing modeling tools for engineering level analysis. One such tool produced by a leading RDRE research team from NASA has been the main focus of this paper. The RDRE model implemented in MATLAB serves as a highly effective analysis tool capable of predicting RDRE performance to enable mission and system level analysis and optimization.

The RDRE performance and sizing code was used to produce a baseline RDRE design for given operating and design conditions from a reputable liquid rocket engine design textbook. The equivalent RDRE system showed significant improvements in both performance, reduced pump feed system requirements, and reduced form factor. The RDRE design was not optimized and served as a means to introduce all possible inputs and outputs provided within this code. The code enables additional component modeling

including regenerative cooling and open cycle gas generator turbopump pump feed system level performance analysis.

Potential improvements achievable by an RDRE modeled using this code showed a 14.91% increase in specific impulse when compared to a deflagration based engine at equivalent operation conditions for a thrust of 750,000 lbf. Pump feed system requirements were also reduced indicating a 11.22% reduction from 26,640 horsepower required for the deflagration engine compared to 23,676 hp required for the conceptual RDRE design producing equivalent thrust. The total required mass flow rate was also computed to decrease by 12.97%. The RDRE length is predicted to be reduced by 44.78% when comparing to the length of the deflagration combustion chamber for the hypothetical A-1 engine designed by Huzel et al.

Parametric analysis was then performed enabled by the extremely computationally efficient capabilities of this engineering level RDRE analysis code. Parametric sweeps are computed within seconds and resulting analysis is discussed and design implications assessed. Results are provided for varying operational conditions and geometric sizing parameters. Performance trends for the engine configuration studied indicate improving performance with increasing engine diameter and hub-to-tip ratio. The operating pressure at the inlet manifold, equivalence ratio of RP-1 and O_2, and the aspect ratio of the RDRE are also varied. Plots and data are presented and each parameter's impacts on performance discussed. The authors of the code cite the aspect ratio for an RDRE typically being five times the hydraulic diameter of the annular chamber. However, some preliminary results have indicated this parameter can possibly be smaller without losing performance. By decreasing this value, resulting engine lengths are reduced and total chemical energy loss to the engine walls is reduced thereby improving engine Isp performance. The assumption on potentially feasible values on the engine aspect ratio are then used as part of a large scale design of experiments to assess a wide range of potential designs.

The penultimate chapter focuses on this design of experiments performed through leveraging the scripting nature of this code along with parallel computing capabilities. The computational cost analysis was first done by executing the same task under across 2, 10, and 16 cores. The average time per case on a modern 16 core AMD CPU was found to be 0.0452 seconds. This included the time to initiate the parallel compute workers and to completion and writing the data to computer memory. This average time per case simulated was used to inform reasonable limits on the number of total number of levels for each factor within the DoE space.

A total of 463,050 engine configurations were computed. Of these, 47,020 engines were removed due to the effective length being shorter than the actual length. The resulting engines provide valuable insights into performance distributions amongst all factorial combinations. Engines from 2 inches to 14 inches were modeled with inlet pressure ranges from 700 to 1300 psi. A range of aspect ratios and hub-to-tip ratios provided coverage of engine sizing. Detailed analysis is provided including the visualization of performance trends in four dimensional design parameter space.

Idealized deflagration rocket engine performance computations are made through calibrating the model's combustion efficiency parameter. Results indicate upwards of 17% increase in Isp for engines at equivalent operating pressures. This trends well with other comparisons made to existing designs and experimental data. A brief assessment of payload performance increase for a hypothetical orbital maneuvering vehicle is made. Simple ΔV computations are made using the idealized rocket equation along with two

Isp values indicative of potential performance metrics for RDREs. The upper limit from the DoE engine optimization analysis indicates that achieving 17.45% improvement in Isp will provide approximately 56% increase in payload for this particular sample mission analysis.

Lastly, an optimized 15k thrust class engine design is provided. The final engine selected provides 15,321 lbf of thrust with a specific impulse at sea-level ambient conditions of 308.48 seconds. This engine is predicted to achieve 30.86 more seconds of Isp relative to an idealized deflagration engine. The total mass flow rate is 49.71 lbs with for an RP-1/OX engine operating at 850 psi with an equivalence ratio of 1.2. This engine was selected based on requirements on Isp and maximal heat flux to the walls. The total heat flux the regenerative cooling system is required to sustain is 5,028.95 BTU/s. Discussion is provided on the selection and qualitative trades made to obtain the finalized engine design.

7.2 Further Research

Harnessing detonative propulsion has been shown to be a feasible pathway for the advancement of advanced liquid rocket propulsion systems, potentially reshaping the entire rocket propulsion system design approach in the coming decades. Although air-breathing propulsion was not a focus of this report, there is ongoing research and experimental validation of improved efficiency in turbine engines that harness detonation as their form of combustion. Progress on both fronts is posed to enable improvements in aerospace vehicle system performance not achievable with the standard form of deflagration based combustion.

RDREs should continue to be perused by the aerospace engineering industry as a viable next-generation propulsion technology demonstrated to provide significant reductions in form factor, improved fuel efficiency and increased performance with reduced mechanical complexity. Such characteristics are crucial for applications requiring rocket propulsion and will enable increased payload capacity, increased operational range, cost reductions and improved sustainability. Significant improvements in propulsive efficiency will enable new missions, systems, and applications not before conceived with deflagration based engines.

Further research is suggested to be made on the full system design and optimization. A large DoE can be implemented within more confined bounds to provide further granularity on design parameters and sensitivities. Subsystem level design and analysis should then be performed to evaluate the overall performance increase and mass savings for an RDRE of equivalent thrust to an existing engine. High fidelity simulations should be performed to better calibrate and tune the engineering level code to provide accurate prediction on combustion performance. Injection schemes should be investigated to minimize pressure losses and entropy generation phenomena such as pre-deonation parasitic deflagration. Further experimental measurements on thermal loads, pressure forces, and vibrational loads across different operating conditions will inform material selection, chamber wall sizing and other crucial aspects of engine design. Verification and validation standards should be further defined by the industry to improve understanding of engine design, modeling, simulation and performance analysis.

References

[1] Zeldovich, Y. B., "To the Question of Energy Use of Detonation Combustion," *Journal of Propulsion and Power*, Vol. 22, No. 3, May 2006, Translation of article originally published in Russian in Zhurnal tekhnicheskoi fiziki (Journal of Technical Physics) Vol.10, Vol.17, 1940, pp. 1453–1461.

[2] Wolański, P., "Detonative propulsion," *Proceedings of the Combustion Institute*, Vol. 34, No. 1, 2013, pp. 125–158.

[3] Frolov, S., Aksenov, V., and Ivanov, V., "Experimental proof of Zel'dovich cycle efficiency gain over cycle with constant pressure combustion for hydrogen-oxygen fuel mixture," *International Journal of Hydrogen Energy*, Vol. 40, No. 21, June 2015, pp. 6970–6975.

[4] Hargus, William A., J., Schumaker, S. A., and Paulson, E. J., "Air Force Research Laboratory Rotating Detonation Rocket Engine Development," *2018 Joint Propulsion Conference*, AIAA 2018-4876, American Institute of Aeronautics and Astronautics, Cincinnati, Ohio, 2018, Session: Potential Applications and System Integration.

[5] GE Aerospace, "GE Aerospace Demonstrates Hypersonic Dual-Mode Ramjet with Rotating Detonation Combustion," Dec. 2023, Available: https://www.geaerospace.com/press-release/other-news-information/ge-aerospace-demonstrates-hypersonic-dual-mode-ramjet-rotating.

[6] Skidmore, I. C., "The physics of detonation," *Science Progress (1933-)*, Vol. 55, No. 218, 1967, pp. 239–257.

[7] Kailasanath, K., "Review of Propulsion Applications of Detonation Waves," *AIAA Journal*, Vol. 38, No. 9, Sept. 2000, pp. 1698-1708, https://doi.org/10.2514/2.1156.

[8] Paxson, D. E., "Pressure Gain Combustion 101," Presentation at Propulsion and Energy 2018, July 2018, NASA Glenn Research Center, Cleveland, OH, United States. GRC-E-DAA-TN58397.

[9] Jones, S. M. and Paxson, D. E., "Potential Benefits to Commercial Propulsion Systems from Pressure Gain Combustion," *49th AIAA/ASME/SAE/ASEE Joint Propulsion Conference*, American Institute of Aeronautics and Astronautics, San Jose, CA, July 2013, No. AIAA 2013-3623, available at https://doi.org/10.2514/6.2013-3623.

[10] Bureau of Transportation Statistics, "Airline Fuel Cost and Consumption (U.S. Carriers - Scheduled) January 2000 - October 2023," Online, 2023, Available Online: https://transtats.bts.gov/fuel.asp.

[11] I., K., Yoneyama, K., Watanabe, H., Itouyama, N., Kawasaki, A., Matsuoka, K., Kasahara, J., Matsuo, A., Funaki, I., and Higashino, K., "Thrust Performance of Converging Rotating Detonation Engine Compared with Steady Rocket Engine," *AIAA Journal of Propulsion and Power*, Vol. 39, May–June 2023, https://doi.org/10.2514/1.B38784.

[12] Teasley, T., Williams, B., Larkey, A., Protz, C., and Gradl, P., "A Review Towards the Design Optimization of High-Performance Additively Manufactured Rotating Detonation Rocket Engine Injectors," Tech. Rep. 20210018267, Marshall Space Flight Center, 2021, Retrieved from NASA Technical Reports Server (NTRS).

[13] Manning, C. G., "Technology Readiness Levels," NASA, 2023, Available: https://www.nasa.gov/directorates/somd/space-communications-navigation/program/technology-readiness-levels/.

[14] "NASA's 3D-printed Rotating Detonation Rocket Engine Test a Success," NASA, 2023, Available: https://www.nasa.gov/centers-and-facilities/marshall/nasas-3d-printed-rotating-detonation-rocket-engine-test-a-success/.

[15] Teasley, T. W., Fedotowsky, T. M., Gradl, P. R., Austin, B. L., and Heister, S. D., "Current State of NASA Continuously Rotating Detonation Cycle Engine Development," *AIAA SCITECH 2023 Forum*, American Institute of Aeronautics and Astronautics, National Harbor, MD, Jan. 2023, No. AIAA 2023-1874 https://doi.org/10.2514/6.2023-1873.

[16] Perkins, H. D., Perkins, D., and Paxson, D., "FY21 Rotating Detonation Rocket Engine Annual Review Presentation," Annual Program Review Presentation, September 2021, Presentation at the Annual Program Review, Virtual Meeting, Sponsored by Space Technology Mission Directorate.

[17] Perkins, D. and Paxson, D., "FY22 Rotating Detonation Rocket Engine Annual Review Presentation," Game Changing Development Annual Program Review, September 2022, Virtual Meeting.

[18] Teasley, T. W., Fedotowsky, T. M., Gradl, P. R., Austin, B. L., and Heister, S. D., "Current State of NASA Continuously Rotating Detonation Cycle Engine Development," *AIAA SCITECH 2023 Forum*, No. AIAA 2023-1873, National Harbor, MD, January 23-27 2023.

[19] Glassman, I. and Yetter, R. A., *Flame Phenomena in Premixed Combustible Gases*, chap. 4, Academic Press, 4th ed., 2008, pp. 147–254.

[20] Glassman, I. and Yetter, R. A., *Explosive and General Oxidative Characteristics of Fuels*, chap. 3, Academic Press, 4th ed., 2008, pp. 75–145.

[21] Wilson, W. E. J. and Fristrom, R. M., "Radicals in Flames," *APL Technical Digest*, Vol. 2, No. 6, 1963, pp. 2–3.

[22] Glassman, I. and Yetter, R. A., *Detonation*, Vol. 1, Academic Press, New York, 4th ed., 2008, pp. 261–307.

[23] Gordon, S. and McBride, B. J., "Computer Program for Calculation of Complex Chemical Equilibrium Compositions, Rocket Performance, Incident and Reflected Shocks, and Chapman-Jouguet Detonations," NASA SP-273, Interim Revision, 1976.

[24] Strehlow, R. A., *Fundamentals of Combustion*, International Textbook Co, 1968.

[25] Vaca, I. A., *A Systematic Literature Review of Rotating Detonation Engines (RDE's) & Potential Scalability for Use in Non-Rocket Based Applications*, Master's project, San José State University, May 2023.

[26] Nakamura, T., *Computational Analysis of Zel'dovich-Von Neumann-Doering (ZND) Detonation*, Master's thesis, Texas A&M University, 2010.

[27] Matalon, M., "Lecture 7: Detonation Waves," University of Illinois at Urbana-Champaign, 2013, Available: https://cefrc.princeton.edu/sites/g/files/toruqf1071/files/Files/2013%20Lecture%20Notes/Matalon/Notes-Lecture-7.pdf.

[28] Štimac, B., "Research of Extreme Explosives," University of Zagreb, Faculty of Mining Geology and Petroleum Engineering, 2017, Available : https://www.rgn.unizg.hr/en/studies/postgraduate-study/blog-en/2834-research-of-extreme-explosives.

[29] Meshkov, E. E., "Instability of the interface of two gases accelerated by a shock wave," *Fluid Dyn*, Vol. 4, 1969, pp. 101–104.

[30] Taylor, J., "The instability of liquid surfaces when accelerated in a direction perpendicular to their planes, I," *Proc. Roy. Soc. Lond. ser. A*, Vol. 201, No. 1065, 1950.

[31] Richtmyer, R. D., "Taylor instability in shock acceleration of compressible fluids," *Communs. Pure and Appl. Math.*, Vol. 13, 1960, pp. 297–319.

[32] Kimura, R. C., Paulson, E. J., Hargus, William, J., and Sankaran, V., "Ideal Thermodynamic Performance Results for Rotating Detonation Rocket Engine Thrust Chambers Using CEA," *AIAA Scitech 2020 Forum*, Orlando, FL, January 2020, pp. 6–10, No. AIAA 2020-0193 https://arc.aiaa.org/doi/abs/10.2514/6.2020-0193.

[33] Cuciumita, C. F. and Porumbel, I., "Computation of Thermodynamic Cycle for Novel Detonation Aircraft Engine," *5th CEAS Air and Space Conference*, COMOTI Romanian Research and Development Institute for Gas Turbines, Bucharest, Romania, 2015, CEAS 2015 paper no. 180.

[34] "Scaled Composites Long EZ Borealis," Aug 2022, Available: https://www.nationalmuseum.af.mil/Visit/Museum-Exhibits/Fact-Sheets/Display/Article/195765/scaled-composites-long-ez-borealis.

[35] Pal, P., Kumar, G., Drennan, S. A., Rankin, B. A., and Som, S., "Multidimensional Numerical Modeling of Combustion Dynamics in a Non-Premixed Rotating Detonation Engine With Adaptive Mesh Refinement," *Journal of Energy Resources Technology*, Vol. 143 No. 11, ASME, November 2021, pp. 112308–1, Available: https://doi.org/10.1115/1.4050590.

[36] Schwer, D. and Kailasanath, K., "Fluid dynamics of rotating detonation engines with hydrogen and hydrocarbon fuels," *Proceedings of the Combustion Institute*, Vol. 34, 2013, pp. 1991–1998, https://doi.org/10.1016/j.proci.2012.05.046.

[37] Paxson, D. E. and Perkins, H. D., "A Simple Model for Rotating Detonation Rocket Engine Sizing and Performance Estimates," *AIAA Scitech 2021 Forum*, Virtual, January 2021, Np. AIAA 2021-0192 https://doi.org/10.2514/6.2021-0192.

[38] Schwer, D. and Kailasanath, K., "Numerical investigation of the physics of rotating-detonation-engines," *Proceedings of the Combustion Institute*, Vol. 33, 2011, pp. 2195–2202.

[39] Paxson, D. E., "Examination of Wave Speed in Rotating Detonation Engines Using Simplified Computational Fluid Dynamics," *2018 SciTech Forum*, No. AIAA 2018-1883, American Institute of Aeronautics and Astronautics, Kissimmee, Florida, Jan. 2018, TM–2018-219870.

[40] Brophy, C. M., Codoni, J. R., Teneyck, J. A., and Spencer, E., "Experimental Performance Characterization of an RDE Using Equivalent Available Pressure," *AIAA Paper*, No. 2019-4212, August 2019.

[41] Roback, R., Szetela, E. J., and Spadaccini, L. J., "Deposit formation in hydrocarbon rocket fuels," Contractor Report (CR) NASA-CR-165405, R81-915216-1, United Technologies Research Center, East Hartford, CT, United States, August 1981, Publicly available under NASA contract NAS3-22277.

[42] Zhang, C., Zhou, J., Zhao, J., Wen, D., and Gao, H., "Three-dimensional CFD model for the coking of supercritical n-decane in circular and elliptical tubes," *Chemical Engineering Science*, Vol. 290, 2024, pp. 119888.

[43] AFRL, "Rotating Detonation Rocket Engines (RDRE)," 2024, Available: https://afresearchlab.com/technology/rotating-detonation-rocket-engines-rdre/.

[44] Smith, R. D. and Stanley, S., "Experimental Investigation of Continuous Detonation Rocket Engines for In-Space Propulsion," *52nd AIAA/SAE/ASEE Joint Propulsion Conference*, American Institute of Aeronautics and Astronautics, Salt Lake City, UT, 2016, No. AIAA 2016-4582 https://doi.org/10.2514/6.2016-4582.

[45] Huzel, D. and Huang, D., "Modern Engineering for Design of Liquid-Propellant Rocket Engines," *Progress in Astronautics and Aeronautics*, Vol. 147, AIAA, 1992.

[46] Daniau, E., Falempin, F., Getin, N., Bykovskii, F., and Zdhan, S., "Design of a Continuous Wave Detonation Engine for Space Application," *42nd AIAA/ASME/SAE/ASEE Joint Propulsion Conference & Exhibit*, No. AIAA 2006-4794, 2006, pp. 9–12, Available: https://doi.org/10.2514/6.2006-4794.

[47] Falempin, F., Daniau, E., Getin, N., and Zhdan, S., "Toward a Continuous Detonation Wave Rocket Engine Demonstrator," *14th AIAA/AHI Space Planes and Hypersonic Systems and Technologies Conference*, November 2006, Available: https://doi.org/10.2514/6.2006-7956.

[48] Sutton, G. P. and Biblarz, O., *Rocket Propulsion Elements*, Wiley, 9th ed., December 2016, pp. 194-245.

[49] Bennewitz, J. W., "Modal Transitions in Rotating Detonation Rocket Engines," *International Journal of Energetic Materials and Chemical Propulsion*, Vol. 18, 2019, pp. 91–109.

[50] Bennewitz, J. W., Burr, J. R., Bigler, B. R., Burke, R. F., Lemcherfi, A., Mundt, T., Rezzag, T., Plaehn, E. W., Sosa, J., Walters, I. V., Schumaker, S. A., Ahmed, K. A., Slabaugh, C. D., Knowlen, C., and Hargus Jr, W. A., "Experimental validation of rotating detonation for rocket propulsion," *Scientific Reports*, Vol. 13, Nature Publishing Group, 2023, Available: https://www.nature.com/articles/s41598-023-40156-y.

[51] Smith, R. D. and Stanley, S. B., "Experimental investigation of rotating detonation rocket engines for space propulsion," *Journal of Propulsion and Power*, Vol. 37, 2021, pp. 463–473.

[52] Kawalec, M., Wolański, P., Perkowski, W., and Bilar, A., "Development of a liquid-propellant rocket powered by a rotating detonation engine," *Journal of Propulsion and Power*, Vol. 39, 2023, pp. 554–561.

[53] Fotia, M., Hoke, J., and Schauer, F., "Performance of rotating detonation engines for air breathing applications," *Shock Wave and High Pressure Phenomena*, Springer, 2017, pp. 1–21.

[54] Colorado State University, "Stoichiometry, Thermodynamics – Lecture Notes," Accessed 2024, Available: https://www.engr.colostate.edu/~allan/thermo/page9/page9.html.

[55] Chacon, F. and Gamba, M., "Study of Parasitic Combustion in an Optically Accessible Continuous Wave Rotating Detonation Engine," *AIAA Scitech 2019 Forum*, 2019, No. AIAA 2019-0473 https://arc.aiaa.org/doi/10.2514/6.2019-0473.

[56] Bigler, B. R., Burr, J. R., Bennewitz, J. W., and Hargus, W. A., "Global Performance Effects of Mode Transitions in a Rotating Detonation Rocket Engine," *AIAA Propulsion and Energy 2020 Forum*, August 2020, No. AIAA 2020-3582 https://arc.aiaa.org/doi/10.2514/6.2020-3852.

[57] Bennewitz, J. W., Bigler, B. R., Hargus, W. A., Danczyk, S. A., et al., "Characterization of Detonation Wave Propagation in a Rotating Detonation Rocket Engine using Direct High-Speed Imaging," *Proceedings of the 2018 Joint Propulsion Conference*, July 2018.

[58] NASA Technology Transfer Program, "A Simple Model for Rotating Detonation Rocket Engine Sizing and Performance Estimates," NASA Software Catalog, n.d., LEW-20423-1.

[59] NASA, "Design and Integration Tools: Genesis Flight Mechanics Simulation and Trajectory Design Tool v0.3.0," Johnson Space Center, n.d., MSC-27061-1.

[60] Heiser, W. H. and Pratt, D. T., "Thermodynamic Cycle Analysis of Pulse Detonation Engines," *Journal of Propulsion and Power*, Vol. 18, No. 1, 2002, pp. 68–76.

[61] Paulson, E. J., Kimura, R., Hargus, W. A., and Sankaran, V., "Ideal Thermodynamic Performance Results for Rotating Detonation Rocket Engine Thrust Chambers Using CEA," *AIAA Paper*, No. 2020-0193, January 2020.

[62] Kaemming, T. A., Fotia, M. A., Hoke, J. L., and Schauer, F. R., "Thermodynamic Modeling of a Rotating Detonation Engine Through a Reduced-Order Approach," *AIAA Journal of Propulsion and Power*, Vol. 33, No. 5, 2017, pp. 1170–1178.

[63] Paxson, D. E., Fotia, M. L., Hoke, J., and Schauer, F., "Comparison of Numerically Simulated and Experimentally Measured Performance of a Rotating Detonation Engine," Tech. Rep. NASA TM–2015-218835; AIAA–2015–1101, 2015.

[64] Rankin, B. A., Hoke, J. L., and Schauer, F. R., "Periodic Exhaust Flow through a Converging-Diverging Nozzle Downstream of a Rotating Detonation Engine," *AIAA*, No. 2014-1015, January 2014.

[65] Thacker, R., Paxson, D. E., and Perkins, H. D., *User's Guide to the RDRE Blowdown Spreadsheet*, NASA, 2022, NASA Documentation.

[66] Paxson, D. E. and Perkins, H. D., "A Simple Model for Rotating Detonation Rocket Engine Sizing and Performance Estimates," *59th AIAA Aerospace Sciences Meeting, SciTech 2021*, AIAA, Virtual Edition, January 11-21 2021, No. AIAA 2021-0192.

[67] Anderson, J., *Fundamentals of Aerodynamics*, McGraw-Hill Education, 6th ed., 2017.

[68] Paxson, D. E. and Schwer, D. A., "Operational Stability Limits in Rotating Detonation Engine Numerical Simulations," *AIAA Paper*, No. 2019-0748, January 2019.

[69] Bennewitz, J. W., Bigler, B. R., Ross, M. C., Danczyk, S. A., Hargus Jr., W. A., and Smith, R. D., "Performance of a Rotating Detonation Rocket Engine with Various Convergent Nozzles and Chamber Lengths," *Energies*, Vol. 14, No. 7, 2021, pp. 2037.

[70] Papadopoulos, P., "AE 210 F23 - Advanced Space Systems Engineering," 2023, Master's Aerospace Engineering course, San Jose State University.

[71] A., V. and Scully S. J., Thaddeus Medical Systems, I., "Protection device that promotes air flow for heat transfer. US 11,090,225 B2," 2021, United States Patent and Trademark Office.

[72] Papadopoulos, P., "Design Sensitivity Analysis, Trade-Off Studies and Approximations and Multi Objective System Level Optimization, Spacecraft Design and Sizing," 2022, Lecture notes for AE 210 - Advanced Space Systems Engineering, San José State University, Fall 2023.

[73] Papadopoulos, P., "Space System Design Optimization and Exploration Techniques," 2023, Lecture notes for AE 210 - Advanced Space Systems Engineering, San José State University, Fall 2023.

[74] Rauf, J., "SpaceX 6 Starship and Super Heavy Booster," OLLI Fall 2023 Lecture Slides, 2023.

[75] Space Launch Report, "SpaceX Falcon 9 v1.1 Data Sheet," Office of Safety and Mission Assurance, NASA, 2017.

[76] Wertz, J. R., Everett, D. F., and Puschell, J. J., editors, *Space Mission Engineering: The New SMAD*, Microcosm Press, 1st ed., 2011, Chapter 8, Table 18-2, p. 532.

[77] Matalon, M., "Lecture 4: Deflagrations and Detonations," University of Illinois at Urbana-Champaign, 2013, Available: https://cefrc.princeton.edu/sites/g/files/toruqf1071/files/Files/2013%20Lecture%20Notes/Matalon/Notes-Lecture-4.pdf.

[78] Hishida, M., Fujiwara, T., and Wolanski, P., "Fundamentals of rotating detonations," *Shock Waves*, Vol. 19, Feb. 2009, pp. 1–10, Published online: 10 February 2009.

[79] HySafe, "Detonations and Shock Waves Module - Fundamentals of Hydrogen Safety: Safety of Hydrogen as an Energy Carrier," Available online at the International Association for Hydrogen Safety, 2024, Available http://hysafe.org/img/fhslect10.pdf.

[80] Glassman, I. and Yetter, R. A., *Combustion*, chap. 3, Academic Press, 2008.

[81] Glassman, I. and Yetter, R. A., *Combustion*, chap. 4, Academic Press, 2008.

[82] Daniau, E., Falempin, F., Zhang, G., et al., "Preliminary Work for a Pulsed Detonation Engine Demonstrator," *14th AIAA/AHI Space Planes and Hypersonic Systems and Technologies Conference*, November 2006, Available: https://doi.org/10.2514/6.2006-7957.

[83] Von Neumann, J., "Theory of Detonation Waves," Progress report, Institute for Advanced Study Princeton NJ, 1942, Accession Number: ADB967734, Report Date: 1942-05-04.

[84] Wolanski, P. and Kawalec, M., "Experimental Research of Performance of Combined Cycle Rotating Detonation Rocket-Ramjet Engine," *27th International Colloquium on the Dynamics of Explosions and Reactive Systems (ICDERS)*, Institute of Aviation, Warsaw, Poland, Beijing, China, July 2019.

[85] Paxson, D. E. and Kaemming, T. A., "Foundational Performance Analyses of Pressure Gain Combustion Thermodynamic Benefits for Gas Turbines," *50th AIAA Aerospace Sciences Meeting including the New Horizons Forum and Aerospace Exposition*, No. AIAA 2012-0770, Nashville, Tennessee, Jan. 2012, NASA TM–2012-217443 https://doi.org/10.2514/6.2012-770.

[86] Ma, J. Z., Luan, M.-Y., Xia, Z.-J., Wang, J.-P., jie Zhang, S., bai Yao, S., and Wang, B., "Recent Progress, Development Trends, and Consideration of Continuous Detonation Engines," Vol. 58, Dec. 2020.

[87] Kailasanath, K., "Review of Propulsion Applications of Detonation Waves," *AIAA Journal*, Vol. 38, No. 9, Sept. 2000, pp. 1698-1708, https://arc.aiaa.org/doi/10.2514/2.1156.

[88] Pandey, K. and Debnath, P., "Review on Recent Advances in Pulse Detonation Engines," *Journal of Combustion*, Vol. 2016, 2016, pp. 1-16, https://doi.org/10.1155/2016/4193034.

[89] Koch, J. and Kutz, J., "Modeling thermodynamic trends of rotating detonation engines," *Physics of Fluids*, Vol. 32, 2020, https://dx.doi.org/10.1063/5.0023972.

[90] Sosa, J., Ahmed, K., Fievisohn, R., Hoke, J., Ombrello, T., and Schauer, F., "Supersonic driven detonation dynamics for rotating detonation engines," *International Journal of Hydrogen Energy*, 2019, pp. 7596 - 7606, https://dx.doi.org/10.1016/J.IJHYDENE.2019.02.019.

[91] Yokoo, R., Goto, K., Kasahara, J., Athmanathan, V., Braun, J., Paniagua, G., Meyer, T. R., Kawasaki, A., Matsuoka, K., Matsuo, A., and Funaki, I., "Experimental study of internal flow structures in cylindrical rotating detonation engines," *Proceedings of the Combustion Institute*, Vol. 38, 2021, pp. 3759–3768, https://dx.doi.org/10.1016/j.proci.2020.08.001.

[92] Kasahara, J., Hasegawa, A., Nemoto, T., Yamaguchi, H., Yajima, T., and Kojima, T., "Performance Validation of a Single-Tube Pulse Detonation Rocket System," *Journal of Propulsion and Power*, Vol. 25, 2009, pp. 173–180, https://dx.doi.org/10.2514/1.37924.

[93] Kasahara, J., Hirano, M., Matsuo, A., Daimon, Y., and Endo, T., "Thrust measurement of a multicycle partially filled pulse detonation rocket engine," *Journal of Propulsion and Power*, Vol. 25, 2009, pp. 1281–1290.

[94] Bigler, B. R., Bennewitz, J. W., Danczyk, S. A., and Hargus, W. A., "Rotating detonation rocket engine operability under varied pressure drop injection," *Journal of Spacecraft and Rockets*, Vol. 58, 2021, pp. 316–325, https://doi.org/10.2514/1.A34763.

[95] Goto, K. et al., "Thrust validation of rotating detonation engine system by moving rocket sled test," *Journal of Propulsion and Power*, Vol. 37, No. 3, 2021, pp. 419–425, https://arc.aiaa.org/doi/10.2514/1.B38037.